A NEW HYDROGEN-ISOTOPE APPROACH TO UNDERSTAND NORTH AFRICAN MONSOON CHANGES IN THE HOLOCENE

BARBARA HAESE

Dissertation zur Erlangung des akademischen Grades
Doktor der Naturwissenschaften (Dr. rer. nat.)

Oktober 2013

Barbara Haese: *A new hydrogen-isotope approach to understand North African monsoon changes in the Holocene,* Dissertation zur Erlangung des akademischen Grades Doktor der Naturwissenschaften (Dr. rer. nat.), © Oktober 2013

GUTACHTER:
Prof. Dr. Gerrit Lohmann
Prof. Dr. Justus Notholt

Eingereicht am: 25.10.2013
Tag des Promotionskolloquiums: 21.01.2014

ABSTRACT

The aim of this thesis is to improve the understanding of the hydrological evolution of the North-West African monsoon system during the Holocene period. In particular the focus is placed on the drastic regime shift from humid and vegetated conditions of the mid-Holocene to the arid present-day conditions in North-West Africa. The timing of this regime shift is investigated in order to determine if the transition from the African Humid Period (approx. from 16,000 – 6,000 years ago) to dry present-day conditions occurred gradually or rapidly. In order to achieve this objective, variations in the isotopic composition of precipitation in relation to rainfall amount are scrutinized.

To reach this goal the coupled atmosphere-land surface model ECHAM5-JSBACH is enhanced by the inclusion of a stable water isotope diagnostic module which traces beside the "normal water" $H_2^{16}O$ the heavier water isotopes $H_2^{18}O$ and HDO. The ECHAM5-JSBACH-wiso model is able to simulate the isotopic composition of precipitation ($\delta^{18}O_P$ and δD_P) comparably well as the stand-alone ECHAM5-wiso model. In order to analyze the sensitivity of fractionation processes over land, a set of simulations with various implementations of these processes over the land surface are compared. The simulations distinguish between no fractionation, fractionation included in the evaporation flux (from bare soil), and fractionation included in both evaporation and transpiration (from water transport through plants) fluxes. While the isotopic composition of the soil water may change for $\delta^{18}O$ by up to +8‰, the simulated $\delta^{18}O$ in precipitation shows only slight differences in the order of ± 1‰.

For evaluation of the simulated isotope composition over the 20th century in North Africa, a nudged ECHAM5-JSBACH-wiso experiment is performed over the period 1958 to 2002. It is shown that the model simulates the climatology as well as interannual variability of precipitation and its isotopic composition in good agreement with observations. Furthermore, it is illustrated that the amount of Sahelian precipitation and δD_P are correlated, with a Pearson correlation coefficient $r = 0.71$. Based on these model results the observed isotope variations are quantitatively calibrated with respect to changes of the precipitation amount. According to the model results, changes of -5‰ in δD_P can be related to an increase of approximately 100 mm in rainfall amount under present-day conditions.

In order to further investigate the evolution of the North-West African hydrological cycle during the Holocene, the precipitation and the vegetation cover simulated by the fully coupled Earth System model COSMOS are analyzed. Both variables indicate

a gradual transition from the African Humid Period into the dry present-day conditions. Based on this transient experiment, time-slice simulations, performed with the ECHAM5-JSBACH-wiso model, are carried out. These time-slice simulations reveal an amplification as well as a southwards shift of the North African rain belt from mid-Holocene to present day. Due to the negative relation between the amount of precipitation and its isotopic composition, the simulated δD in precipitation is about -18‰ more depleted in the mid-Holocene experiment, compared to the present-day one, in the West Sahel region. The findings of the model studies are supported by novel proxy data derived from δD measurements on leaf waxes in the marine sediment core GeoB7920 from the North-West African coast.

In summary, all results of these studies indicate that the drastic regime shift of vegetation and rainfall amount in North-West Africa during mid-Holocene was gradual.

ACKNOWLEDGMENTS

This thesis would not have been possible without the support, patience, and guidance of many, many people.

Firstly I would like to thank my supervisor Martin Werner for his continuous guidance and support. It was he who in the first instance allowed me the possibility of entering the field of climate science and isotope physics. During my time at the Alfred Wegener Institute he always found time to answer my questions, often with a good sense of humor. For that I am very thankful.

I would also like to thank the other members of my PhD committee; Gerrit Lohmann, Enno Schefuß, Britta Beckmann, Grit Freiwald, and Michael Stärz for their constructive discussions, new ideas and general guidance. Also I would like to thank Mr. Justus Notholt for the review and the evaluation of my thesis.

Additional thanks go to the members (both past and present) of the Paleoclimate Dynamics group for the many fun lunch breaks, discussions, group meetings, and other special events. Also, Dirk Barbi, Anne Dallmeyer, Veronika Gayler, Sebastian Rast, Wolfgang Cohrs are thanked for their technical support. I am very grateful to the POLMAR graduate school for the organized courses which I was able to avail of during my PhD years.

Finally, I also want to thank my family and my friends for fun times and encouraging me to never give up. These guys always had my back and were able to support me in both the best and worst of times — thank you all, I will never forget you.

CONTENTS

ACRONYMS

AEJ African Easterly Jet

AEW African Easterly Waves

AGCM atmosphere general circulation model

AMIP Atmospheric Model Intercomparison Project

AMO Atlantic Multidecadal Oscillation

BASIN Biogeosphere-Atmosphere Stable Isotope Network

CRU Climatic Research Unit

ECMWF European Centre for Medium-Range Weather Forecasts

ENSO El Niño-Southern Oscillation

GCM general circulation model

GPCP Global Precipitation Climatology Project

GNIP Global Network of Isotopes in Precipitation

GMWL Global Meteoric Water Line

IAEA International Atomic Energy Agency

IPCC Intergovernmental Panel on Climate Change

ITCZ Intertropical Convergence Zone

ITD Intertropical Discontinuity

MARUM Center for Marine Environmental Sciences University of Bremen

MIBA Moisture Isotopes in Biosphere and Atmosphere

RMSE root mean square error

SIC sea ice cover

SLP sea level pressure

SST sea surface temperature

TEJ Tropical Easterly Jet

V-SMOW Vienna Standard Mean Ocean Water

WMO World Meteorology Organisation

1

GENERAL INTRODUCTION

1.1 MOTIVATION

Extreme events such as heat waves, droughts, or floods dominate the media coverage of climate change. The reactions to the reports of the Intergovernmental Panel on Climate Change (IPCC) show that climate change and climate prediction are not only a scientific issue but have also become important for the politics (first IPCC report: [IPCC, 1990]; political reactions: e. g., the Kyoto Protocol, [UNFCCC]). Regions with extreme conditions, such as the ice-covered poles as well as monsoon regions, are particularly prone to climate change. One of these regions is North-West Africa, in particular the Sahel[1] region, where most of the annual precipitation is falling during the monsoon season. Observations over the last century show a high interannual variability of rainfall amount [Nicholson, 2000]. Modern climate models are able to reproduce the present day climate globally and in those regions fairly well [e. g., Lau et al., 1996]. Numerical climate simulations project an increase of the North-West African temperature and a higher frequency of potential drought events for future warming scenarios [Parry et al., 2007]. But how well can these models predict possible future climate conditions and do they depict all climate feedback mechanisms correctly? One way to answer these questions is to evaluate the climate models on past geological epochs, comprising different climate states. Even if the forcing mechanisms triggering climate changes in the past are different then for the present or future climate projections, the underlying regional feedback mechanisms reveal a basic understanding of the climate system. Therefore it is mandatory to understand them.

One of the key parameters for long-term changes[2] in Earth's climate are variations of the orbital parameters, which are influencing the distribution of insolation [Milanković, 1969]. By changing these parameters, eccentricity, obliquity, and precession, mainly the spatial and seasonal distribution of incoming solar radiation varies. In the Subtropics most important for variations of the incoming solar radiation during the current epoch,

1 The Sahel is a semi-arid transition zone from the Sahara desert in the north to the dry or humid savanna in the south.

2 Long-term changes, also called 'changes on an orbital timescale', are variations on timescales from 10,000 to 100,000 years.

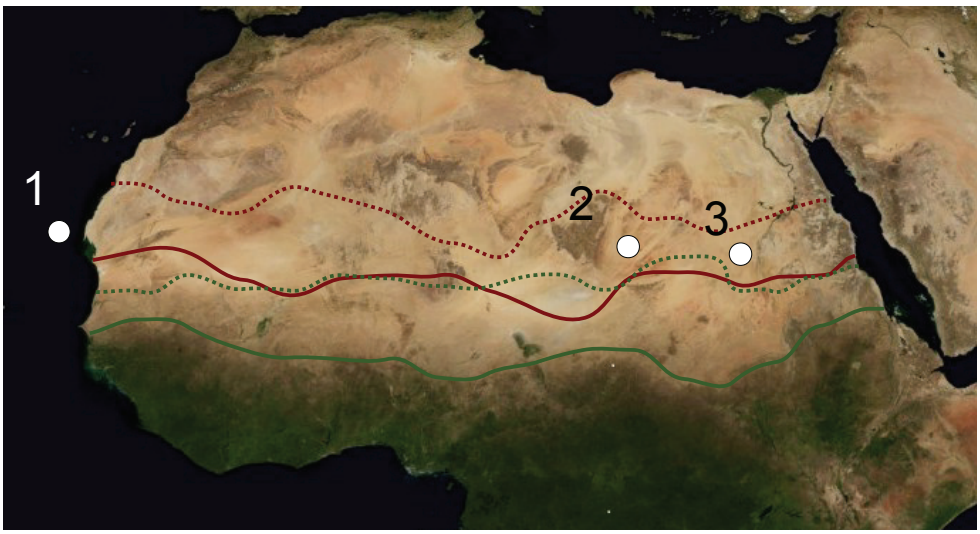

Figure 1.1.: The approximately southern border of the Sahara (red) and the Savanna (green), for present day (solid line) and 8,000 before present (dotted line) in North Africa. [Borders are reproduced after "Map of the Climatic Changes in the Sahara Desert", National Geografic Maps, 2008]. Positions marked by white circles: The approx. location of sediment-core depicted in Fig. 1.2a (1), the pollen record pictured in Fig. 1.2b (2), and excavation site for the findings shown in Fig. 1.3 (3). [Background map: http://visibleearth.nasa.gov, NASA]

the Holocene[3], is the precession parameter, which amplifies the seasonal cycle. Since the North-West African monsoon is triggered by the differential heating between ocean and land surface, Kutzbach [1981] has suggested that changes of incoming solar radiation control the strength of the monsoons over orbital timescales. According to this theory, the North-West African monsoon was intensified during the early- and mid-Holocene compared to present day. Therefore the conditions in North Africa were more humid and more vegetated (see Fig. 1.1).

This theory has been confirmed by numerous proxy[4] studies; two examples are shown in Fig. 1.2. Studies of marine [e. g., deMenocal et al., 2000; Weldeab et al., 2007; Dupont, 2011] or lake [e. g., Gasse, 2002; Kröpelin et al., 2008] sediment cores illustrate the shift from more humid conditions during early- and mid-Holocene to present dry conditions. Also, archaeological records (examples are shown in Fig. 1.3) of the formerly resident population, such as skeletons, cave paintings, rock engravings etc. confirm, that some parts of modern Sahara were inhabited during the early- and mid-Holocene [McIntosh and McIntosh, 1983; Sereno et al., 2008].

3 The Holocene is a geological epoch which began approx. 12,000 years before present (BP) and continues to the present. It is characterized by the ongoing warm period.

4 A proxy is an indirect indicator of the climate, which was recorded in natural archives such as e. g. ice cores, corals, sea or ocean sediments, pollen, tree rings, and human archives as historical records. Proxies can be used to reconstruct the climate of the past, when there was no instrumental recording.

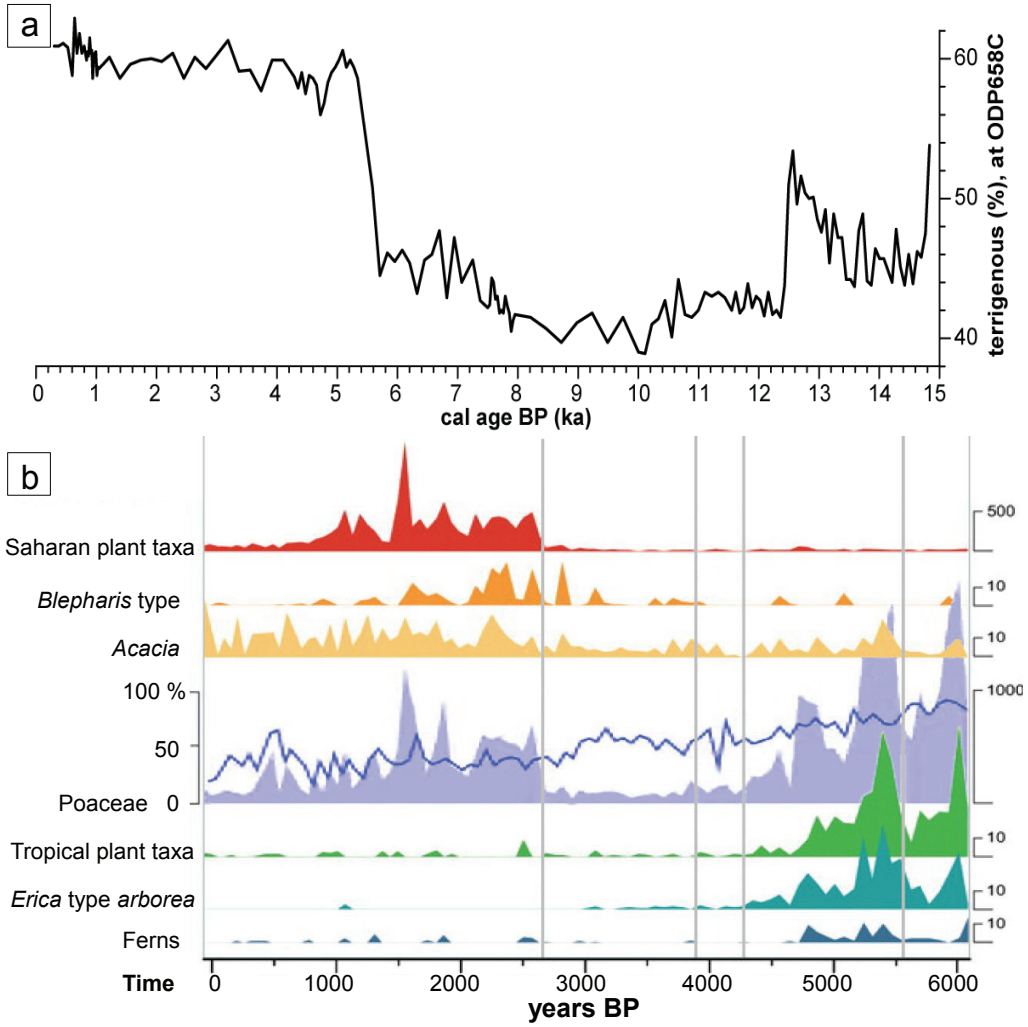

Figure 1.2.: (a) Terrigenous material measured in sediment core ODP658C (Fig. 1.1, location 1), is interpreted as showing an abrupt end of the African Humid Period [deMenocal et al., 2000]. (b) Pollen record of Lake Yoa (Fig. 1.1, location 2), is interpreted as showing a more gradual transition from wet to dry conditions [Kröpelin et al., 2008].

Over the past decades, progress has been made in understanding the underlying mechanisms of the evolution of the North-West African climate. Increased summer insolation, due to changes of the orbital parameters, enlarged the surface temperature gradient between the Atlantic ocean and the land — which results in an amplified boreal summer monsoon [Kutzbach and Street-Perrott, 1985]. Further studies identified positive feedback mechanisms, e. g. between monsoon changes and sea surface temperature (SST) as well as sea level pressure (SLP) [e. g., Kutzbach and Liu, 1997], open water bodies on land-surface [e. g., Krinner et al., 2012], vegetation [e. g., Claussen and Gayler, 1997; Kutzbach et al., 1996], or land albedo [e. g., Vamborg et al., 2011; Stärz et al., 2013].

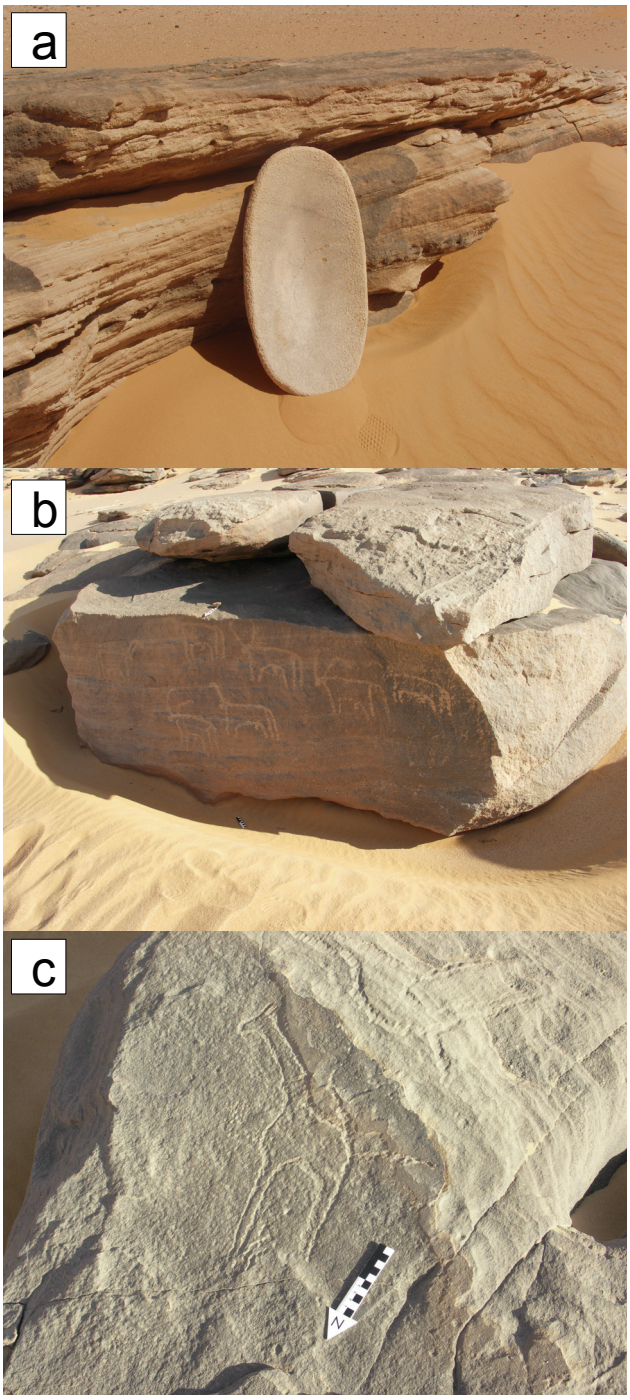

Figure 1.3.: (a) Bowl of the formerly resident population (Fig. 1.1, location 3) indicates that this region was inhabited [A. Gundelwein, personal communication]. The rock engravings, (b) a cattle herds [Ossing, 2012, page 91]. (c) A giraffe [A. Gundelwein, personal communication], dated of approx. 8,000–5,000 years before present (Fig. 1.1, location 3), suggests that the region was populated by humans and animals.

However, there is still an ongoing debate if the transition from more humid conditions during early- and mid-Holocene towards dry modern conditions was abrupt or gradual. Both theories are supported by proxy data and results from model studies. The theory of an abrupt degeneration of the vegetation [e. g., proxy data: deMenocal et al., 2000; Adkins et al., 2006; model-studies: Claussen et al., 1999; Liu et al., 2007] is based on the assumption that the gradual declining summer insolation triggered a strong atmosphere land surface feedback mechanism which led to an abrupt desertification of the Sahara. In contrast, e. g., Weldeab et al. [2007], Kröpelin et al. [2008] (proxy data) and e. g., Braconnot et al. [2007a], [2007b] (model studies), have proposed a gradual change in precipitation amount and vegetation cover.

1.2 OBJECTIVES AND RESEARCH QUESTIONS

The overall goal of this work is an improved understanding of the hydrological evolution and variability of the North-West African monsoon system. A special interest lies on drastic "regime shifts", such as from vegetated and wet conditions during the Holocene towards present day dry conditions or, more recently, the Sahel drought during the 1970s and 1980s. In particular, the variations in amount of Sahelian precipitation and the changes of its isotopic composition are examined.

Since the pioneering work of Dansgaard [1964], the coherence between the isotopic composition of $H_2^{16}O$, $H_2^{18}O$, and HDO in precipitation and climate variations is used to reconstruct paleo climate states. These reconstructions are possible because the isotopic composition in precipitation depends on the surrounding environmental conditions during phase transitions of a water mass, with, temperature or amount of the formed precipitation as key influencing parameters. Since stable water isotopes differ by mass and symmetry of their molecules, they behave differently during any phase transition. While the heavier molecules $H_2^{18}O$ and HDO tend to stay in the liquid or solid phase, the lighter $H_2^{16}O$ molecules evaporate more easily. The strength of this partitioning effect is called fractionation [Friedman and O'Neil, 1977].

As a first step, the coupled atmosphere-land surface model ECHAM5-JSBACH is enhanced by a stable water isotope diagnostic module for $H_2^{18}O$ and HDO. For the investigation of the Holocene climate and its hydrological evolution this ECHAM5-JSBACH-wiso model is used, which allows an explicit comparison between the simulated isotopic composition within the hydrological cycle and the isotopic composition retrieved from proxy data. In this work, the recently reconstructed isotopic signal of sediment cores in the coastal area of North-West Africa are used for the model-data comparison. This

reconstruction has been derived as part of the HYDRACENE[5] project by the Center for Marine Environmental Sciences University of Bremen (MARUM).

In detail, this thesis addresses the following questions:

1. **How much do fractionation processes over land surface influence the global distribution of the isotopic composition in precipitation?**

   Within this PhD study, the isotope-enabled model ECHAM5-JSBACH-wiso has been developed. The evaluation of this new model can be divided into two research questions: (1) What are the implications of using the coupled ECHAM5-JSBACH-wiso instead of the stand-alone ECHAM5-wiso model? To answer this question, the key variables of JSBACH, which can influence the atmospheric water cycle in ECHAM5, and the related changes of the isotopic composition of precipitation are examined. (2) Which impact has the isotopic fractionation over land surface on the isotopic composition of precipitation? The determining factor here is the evapotranspiration, so three different setups for the implementation of fractionation processes over land are taken into consideration. First, it is assumed that no fractionation during evapotranspiration occurs at all, similar to the approach used in the ECHAM5-wiso model [Werner et al., 2011]. Second, the assumption that fractionation only occurs during evaporation from bare soil but not during transpiration by plants is taken. And last, the theoretical case that fractionation processes take part during both evaporation and transpiration of water from land surface is considered.

2. **What is the relation between the amount of precipitation and its isotopic composition in North-West Africa?**

   For answering this question a 45-years ECHAM5-JSBACH-wiso experiment is performed over the simulation period 1958–2002. To retrieve realistic results, the ECHAM5-JSBACH-wiso model is nudged to ERA40 re-analysis data [Dee et al., 2011] of the variables temperature, surface pressure, divergence, and vorticity. The simulated variations of precipitation and its isotopic composition are utilized to evaluate how well ECHAM5-JSBACH-wiso reproduces the North-West African hydrology. As a last step, the relation between the amount of precipitation and its isotopic composition has been estimated for present-day conditions.

5 The project HYDRACENE (A new hydrogen-isotope approach to understand North African monsoon changes in the Holocene) is funded by Deutsche Forschungsgemeinschaft (DFG) as part within the framework of the Special Priority Programme INTERDYNAMIK.

3. **Was the change of the hydrology in North-West Africa characterized by a more gradual or abrupt transition during the Holocene?**

   In order to investigate the Holocene transition of the North-West African climate, a transient model experiment performed by Fischer and Jungclaus [2011] with the fully coupled Earth system model COSMOS[6] is used. Based on this experiment, the evolution of precipitation and vegetation is examined. Furthermore, time slice simulations are carried out with the coupled atmosphere-land surface model ECHAM5-JSBACH-wiso. Model results are used to investigate the spatial distribution of the isotopic composition, and its dependance on the amount of precipitation and the local wind pattern. To complete the picture, the simulated isotopic composition of precipitation is directly compared to reconstructed Holocene isotope values retrieved from marine sediment cores from the North-West African coast.

This PhD thesis is organized as follows: Chapter 2 gives an overview of the physics of stable water isotopes, followed by a detailed description of the hydrological system of North-West Africa in Chapter 3. The model ECHAM5-JSBACH-wiso, which has been developed within this PhD study, is described in Chapter 4[7]. This chapter also contains a description of the other models which are used in this study. The Chapters 5, 6, and 7 discuss the research questions outlined above. A final conclusion and outlook are given in Chapter 8.

6 The Earth system model COSMOS consists of the following components: the atmosphere model ECHAM5, the ocean model MPI-OM, and the land surface scheme JSBACH.

7 The Chapters 4 and 5 are partly published in Haese et al., (2013)

2

STABLE WATER ISOTOPES

In the last decades, stable water isotopes have proven to be a useful tool for understanding climate variations in the past. In order to understand the role of stable water isotopes as a climate proxy, it is required to know their physical characteristics. This chapter will give an overview about the physical behavior of the stable water isotopes.

Isotopes of an element have nuclei with the same number of protons, but different numbers of neutrons. Therefore, they have identical chemical properties, but due to their different masses their have slightly different physical characteristics. For both components of H_2O, the hydrogen as well as the oxygen, stable isotopes exist (see Tab. 2.1). Most important formations of the water molecule H_2O in climate science, beside the normal water $H_2^{16}O$, are $H_2^{18}O$ and $^1H^2H^{16}O = HDO$[1]. Usually, the concentration of the heavier isotopes is expressed as a ratio in comparison to a standard. The internationally accepted protocol used in this work is the Vienna Standard Mean Ocean Water (V-SMOW standard), which defines reference isotope ratios $\frac{^{18}O}{^{16}O} = (2005.20 \pm 0.45) \times 10^{-6}$ and $\frac{D}{H} = (155.95 \pm 0.08) \times 10^{-6}$, measured in [ppm], [IAEA/WMO, 2006].

Oxygen			Hydrogen	
^{16}O	^{17}O	^{18}O	^1H	$^2H = D$
99.76	0.04	0.20	99.985	0.015

Table 2.1.: Natural averaged abundances of oxygen and hydrogen isotopes, measured in [%]. [Gat et al., 2001]

Often, the isotopic compositions and their variations are expressed by a δ-notation measured in [‰], as a ratio with respect to the V-SMOW standard, which is given by:

$$\delta^{18}O = \left(\frac{(\frac{^{18}O}{^{16}O})_{sample}}{(\frac{^{18}O}{^{16}O})_{V-SMOW}} - 1 \right) \cdot 1000, \tag{2.1}$$

$$\delta D = \left(\frac{(\frac{D}{H})_{sample}}{(\frac{D}{H})_{V-SMOW}} - 1 \right) \cdot 1000. \tag{2.2}$$

1 The isotope ^2H is also called deuterium (D).

2.1 FRACTIONATION PROCESSES

Depending on the different atomic mass, the isotope species have slightly different physical characteristics. This leads to fractionation processes during phase changes. This isotopic fractionation consists of two parts: equilibrium fractionation and kinetic fractionation.

- **Equilibrium fractionation** is based on the reduction of the vapor pressure due to incorporation of the heavier isotopes in the water molecule. The quantum levels and the occupation numbers change in the intermolecular potentials and thus the strength of the intermolecular bonds in the liquid phase is changed. By reducing the vapor pressure, the heavier molecules are depleted on the vapor phase with respect to the liquid phase. This depletion is described by the equilibrium fractionation factor α (here as an example for ^{18}O for evaporation):

$$\alpha(H_2^{18}O)_{liquid-vapor} = \frac{(R_{H_2^{18}O})_{liquid}}{(R_{H_2^{18}O})_{vapor}} = \frac{p_0(H_2^{16}O)}{p_0(H_2^{18}O)} > 1 \tag{2.3}$$

  Here $R_{H_2^{18}O}$ is the mixing ratio of $H_2^{18}O$ and $H_2^{16}O$, and p_0 is the saturated vapor pressure above water. The temperature dependency of α, measured by Majoube [1971a]; [1971b], can be written as:

$$\begin{aligned}
\ln \alpha(H_2^{18}O)_{liquid-vapor} &= \frac{1137}{T^2} - \frac{0.4156}{T} - 0.0020667 \\
\ln \alpha(H_2^{18}O)_{ice-vapor} &= \frac{11.839}{T} - 0.028224 \\
\ln \alpha(HDO)_{liquid-vapor} &= \frac{24844}{T^2} - \frac{76.248}{T} + 0.052612 \\
\ln \alpha(HDO)_{ice-vapor} &= \frac{16.288}{T^2} - 0.0934
\end{aligned} \tag{2.4}$$

  The Equations 2.4 also shows that the fractionation effect is reduced by increasing temperature T, [Roedel and Wagner, 2011].

- The thermodynamic equilibrium between liquid (solid) and gaseous phase is not always given under natural conditions. If the liquid (solid) and gaseous phase are not equilibrated, an additional fractionation process occurs during the transfer through the water-air interface. This fractionation is described by the **kinetic fractionation** factor (α_k). The α_k is controlled by the individual diffusion coefficients for molecules of different weights. Since the heavier isotopes $H_2^{18}O$ and

HDO have a smaller diffusion coefficient than $H_2^{16}O$, an additional depletion of heavy isotopes at the vapor phase compared to the liquid (solid) phase occurs. Kinetic fractionation mainly takes place during evaporation in an undersaturated atmosphere (e. g., evaporation over the ocean) or during the formation of ice at very low temperatures. [Dansgaard, 1964]

Generally, one can distinguish between two systems (explained in detail by Dansgaard [1964]), which describe the effect of isotope fractionation:

1. **Closed system:**
   In a closed system the product of the phase change remains in the system and during the entire process the isotopes are poised. This system can be described, for each time t in the time interval [0,τ], by the following equations:

$$R_c(t) = \frac{c_x(t)}{c(t)} = \alpha(T)\,\frac{\nu_x(t)}{\nu(t)} = \alpha(T)\,R_\nu(t), \tag{2.5}$$

   and

$$\begin{cases} c_x(0) & = 0, \\ c_x(t) & = \nu_x(0) - \nu_x(t), \end{cases} \tag{2.6}$$

   with $x \in \left\{H_2^{16}O, H_2^{18}O, HDO\right\}$, c as the liquid (solid) condensate, and ν as the water vapor. With f defined as $f := \frac{\nu(t)}{\nu(0)}$, it can be concluded:

$$\frac{c_x(t)}{c(t)} = \frac{\nu_x(0) - \nu_x(t)}{\nu(0) - \nu(t)} = \frac{\nu_x(0)}{\nu(0)}\frac{1}{1-f} - \frac{\nu_x(t)}{\nu(t)}\frac{1}{f^{-1}-1} \tag{2.7}$$

   Here, the isotope ratio decreases approximately linearly with the amount of the generated condensate. The closed system can be used to describe e. g., the forming of cloud droplets inside a cloud before the rain-out, [Roedel and Wagner, 2011].

2. **Open system (Rayleigh system):**
   In the Rayleigh system the product of the phase changes is instantly removed from the system and therefore not longer in contact with the remaining source. To formulate the Rayleigh system the following differential equation is used:

$$\frac{dc_x}{dc} = \alpha(T)\frac{\nu_x}{\nu(t)}. \tag{2.8}$$

   With $dc_x = -d\nu_x$ follows $-\frac{d\nu_x}{dc} = \alpha(T)\frac{\nu_x}{\nu(t)}$. By integration from o to t is obtained:

$$\ln \nu_x\,|_0^t = \bar{\alpha}\ln \nu\,|_0^t \Rightarrow \frac{\nu_x(t)}{\nu_x(0)} = \left(\frac{\nu(t)}{\nu(0)}\right)^{\bar{\alpha}} \Rightarrow \frac{\nu_x(t)}{\nu(t)} = \frac{\nu_x(0)}{\nu(0)} f^{\bar{\alpha}-1}. \tag{2.9}$$

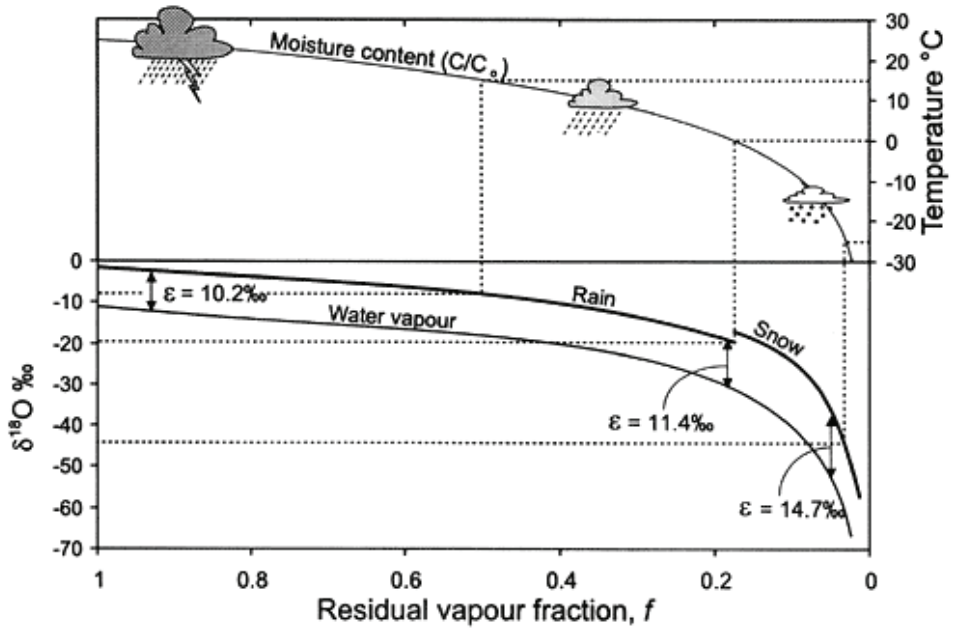

Figure 2.1.: Change of $\delta^{18}O$ of precipitation according to a Rayleigh distillation, starting with $\delta^{18}O_v = -11‰$, $T = 25°C$, and final $T = -30°C$. Below 0°C the fractionation between rainwater and vapor has been replaced by the fractionation between snow and vapor. The fraction of remaining vapor f has been calculated from the decrease in moisture carrying capacity of air at lower temperatures. Dashed lines link $\delta^{18}O$ of precipitation with temperature of condensation. [http://web.sahra.arizona.edu/programs/isotopes/oxygen.html, SAHRA; reproduced after Clark and Fritz, 1997]

$\bar{\alpha}$ is the mean value of $\alpha(T)$ during the time interval [0,t]. During the Rayleigh process the isotopic composition of the vapor as well as of the condensate depletes in order of the power function of the residual water content. The Rayleigh model can be used to describe e. g. the process of rain out of clouds (see an example in Fig. 2.1), [Roedel and Wagner, 2011].

2.2 DISTRIBUTION OF STABLE WATER ISOTOPES

The hydrosphere of the Earth describes the entirety of all water masses on the planet. Due to the physical characteristics of stable water isotopes, the various water reservoirs of the hydrosphere have different isotopic compositions (shown in Tab. 2.2).

Reservoir	Volume [%]	$\delta^{18}O$ [‰]	δD [‰]
Ocean	97.2	0 ± 1	0 ± 5
Ice caps and glaciers	2.15	-30 ± 15	-230 ± 120
Groundwater	0.62		
Vadose water		-5 ± 15	-40 ± 70
Dilute groundwater		-8 ± 7	-50 ± 60
Brines		0 ± 4	-75 ± 50
Surface waters	0.017		
Freshwater lakes		-8 ± 7	-50 ± 60
Saline lakes and inland seas		-2 ± 5	-40 ± 60
River and stream channels		8 ± 7	-50 ± 60
Atmospheric water	0.001	-20 ± 10	-150 ± 80

Table 2.2.: Approximate volumes and typical isotopic composition of different hydrosphere reservoirs. [Criss, 1999]

2.2.1 *Effect of climate variations on the isotopic composition of precipitation*

In 1964, Dansgaard has shown how climate variations effect the isotopic composition in precipitation and introduced the following concepts:

- A linear relationship exists between the composition of isotopes in precipitation and the local temperature (the so-called **temperature effect**). This temperature effect can be seen in the depletion of stable water isotopes in precipitation from the tropics to the high latitudes.
- In the tropics this linear relation collapses and is replaced by a weaker relation between the amount of precipitation and its isotopic composition (the **amount effect**). The amount effect describes for example changes in the isotopic composition over the seasons, thus explains the isotopic depletion of precipitation in the rainy season and the relatively high isotope values during the dry season.
- The **continental effect** describes the gradual rain out over the land mass. This effect may be represented relatively well by a Rayleigh model approach.
- The relation between the isotopic composition in precipitation and the altitude, the **altitude effect**, is temperature-related and states that the isotope values are gradually deplete with increasing elevation.

2.2.2 *The deuterium excess and the Meteoric Water Line*

The isotopic relation of δD versus $\delta^{18}O$ of global precipitation can be approximately described by the Global Meteoric Water Line (GMWL), shown in Fig. 2.2, which was given by Craig [1961] as: $\delta D = 8 \cdot \delta^{18}O + 10$ [‰]. The GMWL is governed in the first order, by the slope of 8, the relation between the equilibrium fractionation factors of the isotopes ^{18}O and D. In the second order, it shows a positive excess of δD, which is globally approximated by 10 [‰]. This excess of δD is caused by the kinetic fractionation effects[2].

In 1964, Dansgaard has defined the quantity "deuterium excess" (dex) as:

$$dex = \delta D - 8 \cdot \delta^{18}O \text{ [‰]}. \tag{2.10}$$

The deuterium excess transports information about the atmospheric conditions during evaporation to the place of precipitation. Thus, the deuterium excess indicates with values of $dex < 10$ ‰ ($dex > 10$ ‰) humid (arid) conditions at the vapor source.

2.3 STABLE WATER ISOTOPES IN CLIMATE MODELS

The isotopic composition of past environmental water has been recorded in various paleo climate archives, e. g., ice cores [e. g., Petit et al., 1999], plant waxes [e. g., Collins et al., 2013], corals [e. g., Giry et al., 2013], or speleothems[3] [e. g., McDermott et al., 2011]. However, the interpretation of these proxy data is often not straight forward, as the measured isotopic signal combines diverse fractionation processes of the water's history. For instance a δ-signal retrieved from plant waxes often records, beside fractionation during precipitation and evaporation, local hydrology and biochemical processes. Including stable water isotopes as tracers in the hydrological cycle of climate models may help to improve the understanding of the isotopic composition recorded in the climate archives.

Since Dansgaard [1964] has shown the coherence between the isotopic composition of precipitation and climate variations, the investigation of numerical models, equipped with stable water isotopes, has started as well. Dansgaard [1964] has explained several climatic effects of stable water isotopes with a simple Rayleigh-type model. The most complete kind of models representing the isotopic composition in the hydrology of the Earth are general circulation models (GCMs) equipped with a stable water isotope diagnostic. An important gain of incorporation stable water isotopes in GCMs is that

2 The diffuseness of deuterium is larger as for ^{18}O, thus the deuterium is less effected by kinetic fractionation effects, [Hoffmann, 1995].

3 A speleothem (or cave formation) is a secondary mineral deposit formed in a cave.

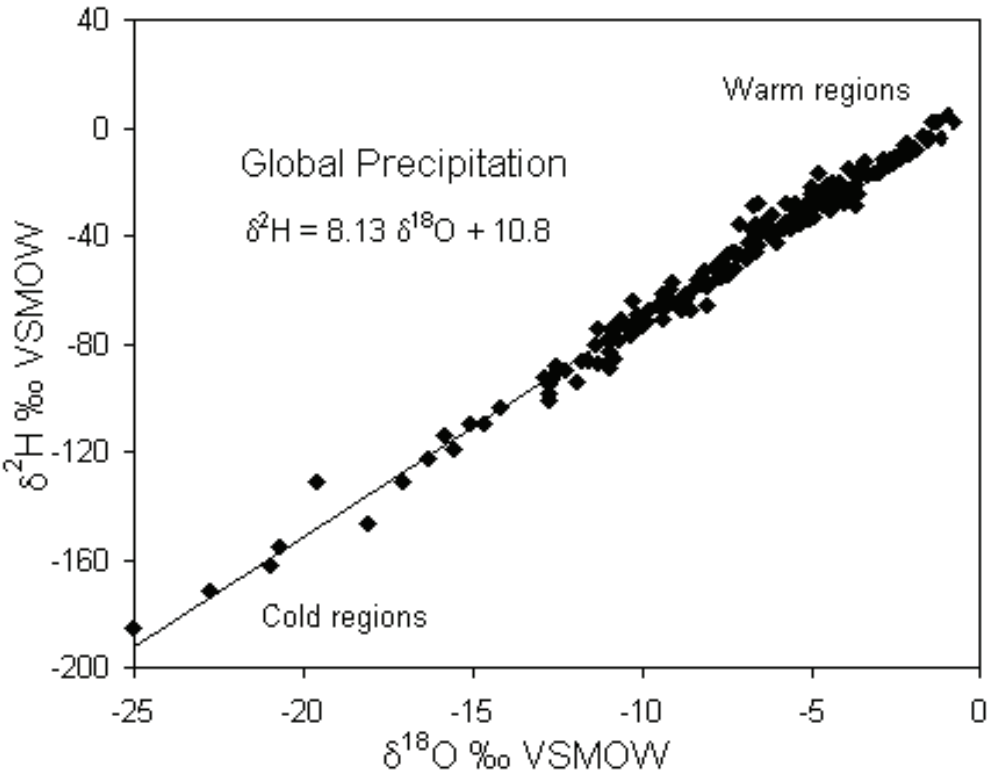

Figure 2.2.: Meteoric relationship of $\delta D = \delta^2H$ and $\delta^{18}O$ in precipitation. Data are weighted average annual values for precipitation monitored at stations in the IAEA global network. [Clark and Fritz, 1997]

the model system is closed and all relevant parameters, crucially for the intensity and evolution of fractionation processes, are calculated by the model itself.

Following the pioneering work of Joussaume et al. [1984], several atmospheric general circulation models (AGCMs) were enhanced with modules for modeling stable water isotopes in the hydrological cycle [e. g., Jouzel et al., 1987; Hoffmann et al., 1998; Noone and Simmonds, 2002; Lee et al., 2007; Risi et al., 2010; Werner et al., 2011]. Moreover, ocean general circulation models (OGCMs) [e. g., Schmidt, 1998; Xu et al., 2012], coupled atmosphere-ocean models [e. g., Schmidt et al., 2007; Tindall et al., 2009], land surface models [e. g., Riley et al., 2002; Cuntz et al., 2003; Braud et al., 2005; Yoshimura et al., 2006; Fischer, 2006], and coupled atmosphere-land surface models [Aleinov and Schmidt, 2006] have also been equipped with a stable water isotope diagnostics. An overview of the existing GCMs including an isotope module is given by Sturm et al. [2010].

Including stable water isotopes into GCMs enables the possibility of investigation of the relationship between isotopic concentration and climate variables, such as temperature or the amount of precipitation, within the Earths various water reservoirs. Moreover,

the isotope diagnostic within the climate models allows a direct model-data comparison and analysis of the water's history. The benefit of proxy data interpretation by addition of isotope modeling results is shown in various studies [e. g., Jouzel et al., 2000; Vuille and Werner, 2005; Herold and Lohmann, 2009; Risi et al., 2010].

2.4 STABLE WATER ISOTOPES IN LEAF WAXES

In this doctoral study, model simulations are compared to the δD signal incorporated in terrestrial leaf waxes [Niedermeyer et al., 2010; Beckmann et al., 2013, Beckmann, personal communication]. In order to interpret the isotopic data in leaf waxes correctly, one has to understand how the stable water isotopes are incorporated into the proxy.

Leaf waxes secure the leaf from environmental impact and control the evaporation and hydration, especially in warm climates. Leaf waxes consist mainly of various *n*-alkanes[4]. As a source for the hydrogen the plants use the environmental water. Since plants produce leaf waxes over their whole lifetime, they incorporate a continuous isotopic signal.

The relation between the isotopic composition of precipitation and the isotopic signal contained in leaf waxes is shown in the conceptual scheme from Sachse et al. [2012] in Fig. 2.3. The soil water taken up by the plant is, due to the evaporation, relatively enriched with deuterium compared to the precipitation. This water is transported within the plant via the xylem into the leafs, where it can transpire to the atmosphere. Until leave cells are replenished with water, a fractionation process occurs during transpiration between liquid water and water vapor in the stomata[5]. Therefore, the δD of the remaining water in the leaf is relative enriched compared to the soil water. However, the most important change in the isotope ratio is caused by the biosynthesis. During incorporation of hydrogen into the *n*-alkanes, the δD signal of the leaf waxes gets strongly depleted compared to the δD of the water. The factor of depletion is dependent on the plant type, as for example trees, shrubs, warm- or cold-season grasses [Sachse et al., 2012]. These plant types can be classified into the functional plant groups of C_3 and C_4. While the C_3 plant type includes e. g. nearly all trees, could season grasses, and cold season sedges, the C_4 plant type enfolds e. g. warm season grasses and sedges [Sachse et al., 2012].

Since the magnitude of the apparent fractionation within the plants is dependent on the functional plant type, it is necessary to calculate the fraction of C_3 and C_4 vegetation

4 *n*-alkanes are characterized by the formation of linear and unbranched chains, which are only represented by carbon and hydrogen. The general chemical formula is given by: C_nH_{2n+2}

5 Stomata are guard cells of the epidermis, which are used for internal and external gas exchange of a plant.

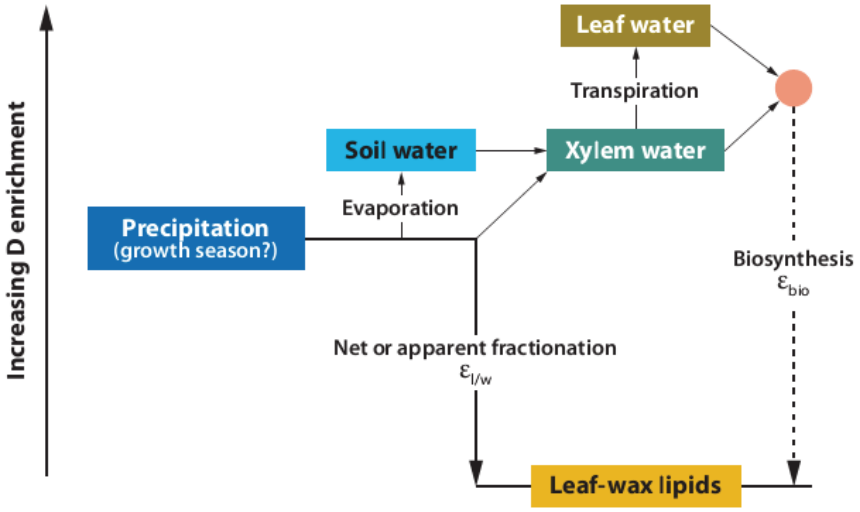

Figure 2.3.: Conceptual model of the relation between environmental precipitation and δD in *n*-alkanes from leaf wax. The red dot illustrates a hypothetical biosynthetic water pool, ϵ_{bio} is the biosynthetic hydrogen isotopic fractionation, and $\epsilon_{l/w}$ denotes the isotopic fractionation between lipids and source water. [Sachse et al., 2012]

in order to estimate the δD in precipitation (δD_P) from the δD-signal in *n*-alkanes. The reconstruction of the $\frac{C_4}{C_3}$ plant ratio has been explained in detail by Castañeda et al. [2009]. Based on the estimated $\frac{C_4}{C_3}$ plant ratio the δD_P can be estimated by using the net fractionation $\epsilon_{l/w}$ of the related functional plant types. However, since the maximum error of the calculation of the functional plant types is approx. ±20% [Castañeda et al., 2009], the estimated δD_P values also include relatively high uncertainties.

3

NORTH-WEST AFRICAN MONSOON SYSTEM

The hydrology in North-West Africa is mainly driven by the North-West African monsoon system, which is the second largest monsoon system of the Earth [Fink, 2006]. In this chapter, a short review of the main characteristics of this monsoon system is given. Furthermore, the reasons for its variability on different timescales and some feedback-mechanisms are summarized.

3.1 NORTH-WEST AFRICAN MONSOON SYSTEM — PRESENT-DAY

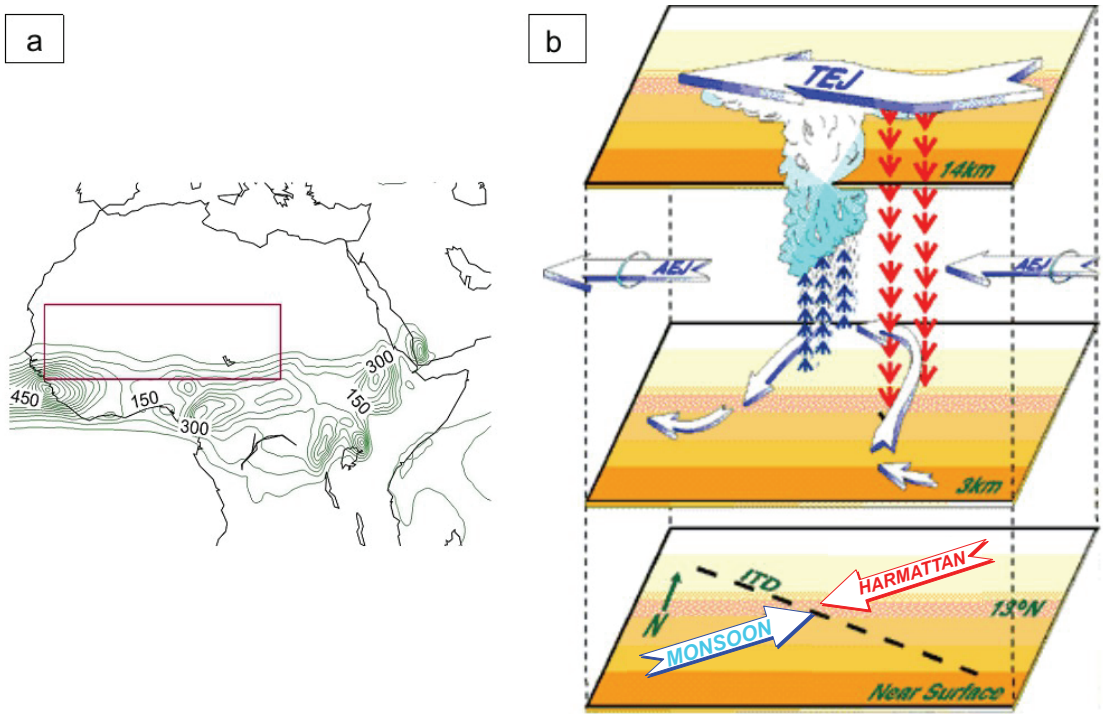

Figure 3.1.: (a) North Africa with the observed (ERA40) strength, in [mm/month], and position of the North African rain-belt during the rainy season (mean over June–September). The position of the wind system depicted in panel (b) is approximated by the red box. (b) Scheme of the wind system over North-West Africa [after Druyan, 1996].

Most of the annual precipitation of North Africa occurs in the monsoon season, which lasts from June to September. The North-West African monsoon system can be related to the occurrence of the following wind systems: the Tropical Easterly Jet (TEJ), the African

Easterly Jet (AEJ), and the southwesterly monsoon flow which is crossing the northeast Harmattan trade winds (see Fig. 3.1b). The area where the monsoon winds meet the Harmattan winds is called Intertropical Discontinuity (ITD). These wind systems define the position of the North African rain belt and control its intensity [Nicholson, 2009]. The key components of the North-West African monsoon system can be described as follows:

- The core region of the **TEJ** is located in approx. 150–200 hPa and 7°N. This jet is a result of the increased geopotential gradient given by the anticyclone of the Sahara desert. Since the intensity of the TEJ differs strongly between dry and wet years in the Sahel region, it could have a strong influence on the intensity of the rainy season [Grist and Nicholson, 2001; Yeshanew and Jury, 2007]. The TEJ is able to create local convergent or divergent areas, which are able to produce vertical velocity and interact with the large scale circulation. Thus, the shift of the TEJ core position between East and West Africa results in an amplified near surface convergence at the Central Sahel region [e. g., Nicholson and Grist, 2003].

- The **AEJ** is located approx. at 650 hPa and 5° north of the ITD, which is in summer approx. 14°N. It is driven by the temperature gradient between the Sahara and the Atlantic. During most of the rainy season the AEJ achieves the barotrope instability criterion of a barocline jet stream [Charney and Stern, 1962]. As a result of the barotropic instability the African Easterly Waves (AEW) arise at approx. 14°E on the jet niveau. Along the AEW, squall lines are formed which generate storms of low pressure. These storms cause much of the precipitation in this region [Fink, 2006].

- The main driving mechanism of the **monsoon wind** is the different heating of the North African land masses and Atlantic ocean. The strongest temperature gradient exists during the summer months [Ramel et al., 2006]. This temperature gradient is caused by the larger heat capacity of the ocean compared to the land. As a result, the land surface heats up much faster during the boreal summer than the surface layer of the ocean. Additionally, due to the current circulation of the ocean, warm surface water is mixed with deeper and colder layers of water in the ocean. In contrast, on land surface heat transport only takes place by diffusion, thus the annual variations of temperature are only dependent on radiation. As a result of those two mechanisms, a gradient of geopotential height is developed, which causes an air flux from the Atlantic in the direction of the strongest warming on the continent. These monsoon winds transport moisture to the land mass. On land surface the monsoon wind is crossing at approx. 20°N in West Africa (15°N in East Africa)

with the dry North-East Harmattan winds. In this zone the ITD, which is characterized by a shift of temperature and dew point, is forming. In literature, the ITD is often equated with the Intertropical Convergence Zone (ITCZ), which is defined as the area with the maximal troposphere water vapor convergence column. At present, the ITCZ has its northernmost position in August at approx. 11°N. While over the ocean the ITD, ITCZ and the area of maximal precipitation are mostly at the same position, on the African continent they are separated [Nicholson, 2009].

During the boreal winter, when the solar radiation is weaker, the monsoon wind reverses. Caused by the weaker insolation the air above the land mass cools more rapidly than the air above the relatively warm ocean. This results in a gradient of geopotential height with high pressure above the land mass and low pressure above the ocean.

- The North African rain belt is formed by a couple of cloud systems, which are highly dependent on the wind system. Thus, it also has a strong seasonal cycle. While during winter northern Africa is influenced by the dry Harmattan winds, during summer the rain belt is moving in northern direction. It is intensifying by the wave activity of the AEJ at approx. 10°N. The northernmost position of the rain belt is in August at approx. 20°N [Nicholson, 2009].

3.2 INFLUENCE OF LAND SURFACE CONDITIONS

The monsoon wind is triggered by the diversity of surface warming between ocean and land surface, therefore the characteristics of the North African monsoon system are also influenced by the land surface.

- Charney [1975] has presumed that the droughts in the Sahel could be triggered by feedback mechanisms between land surface and the monsoon system. This theory relies on the mechanism of radiation in subtropical deserts. Although the Sahara has a higher albedo than vegetated land surfaces, the absence of clouds above the desert allows a strong surface warming. Therefore, the Sahara is a net radiation sink relative to the surrounding environment. To obtain the thermodynamic equilibrium, the air masses above the Saharan desert are forced to sink over large scale areas. The sinking motion leads to the heating of the air, a reduction in relative humidity and the dissolution of clouds. This in turn lowers the probability of rain and consolidates the desert state. Moreover, Claussen [1997] has shown that a decrease in albedo reverses this processes, and the vegetation spreads further north and the precipitation increases.

- Even if the albedo is the determining factor in the relationship between land surface and atmosphere [Levis et al., 2004], other parameters such as vegetation, surface roughness, soil water holding capacity, and open water resorts have to be taken into account as well. These parameters provide the strength of evaporation and transpiration and therefore they affect also the energy budget. Those changes of the surface energy budget are strong enough to provide modifications on the large scale circulation. This in turn influences the strength and position of the North African rain belt [see e. g. Nicholson, 2000].

3.3 CLIMATE VARIABILITY IN THE SAHEL ON DIFFERENT TIMESCALES

The factors responsible for climate variability can generally be divided into two classes: boundary forcing and internal dynamics [Shukla, 1981]. While interannual variations are mostly triggered by internal dynamics, the long term evolution is often driven by changes of the boundary conditions (for example insolation or green-house gases).

3.3.1 *Variability of present-day precipitation*

North-West Africa, especially the Sahel, is a region with a high interannual or multi-year variability in the amount of precipitation. There is also a large variability of the spatial scale of precipitation in the Sahel. Depending on the spatial coherence, the literature distinguishes between two common rainfall anomaly patterns: a dipole anomaly pattern with the pivot approx. 10°N (Fig. 3.2, left panel) and a non dipole pattern (Fig. 3.2, right panel). The result are four different anomaly configurations which have varying atmospheric and surface conditions. Nicholson and Grist [2001] have presumed different causes for the dipole and non-dipole anomaly pattern. They were proposing that, while the dipole pattern is mainly connected to a shift of the AEJ, the non-dipole pattern is caused by factors which change the rainfall intensity. It has to be kept in mind, that the distinction between the dipole and non-dipole patterns is useful in order to detect the main differences in the rain belt. But in reality, climate processes on global and regional scale compete and interact.

The displacement of the AEJ, and the resulting predominance of the more dipole pattern is assumed to be triggered by regional changes of SST and SLP [Ward, 1998]. Due to amplified SST and SLP gradients, the monsoon flow is strengthened (and vice versa). Nicholson and Grist [2001] were proposing that the northward shift of the AEJ during wet years is caused by a well-developed monsoon flow. It can also be observed that the wet year anomaly corresponds to a weakened AEJ and an amplified TEJ [Nicholson and

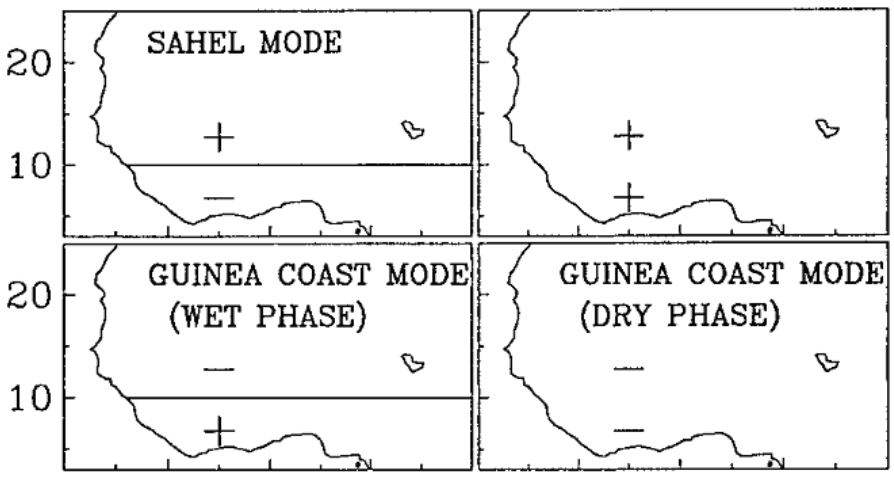

Figure 3.2.: Illustration of the prime annual rainfall anomaly pattern over North-West Africa. [after Nicholson and Grist, 2001]

Webster, 2007]. The opposite effect can be seen in dry years [Nicholson and Webster, 2007]. Variations of the regional SST pattern may, for example, caused by the Atlantic Multidecadal Oscillation (AMO). Mohino et al. [2011] have proposed that a positive phase of AMO leads to enhanced Sahelian rainfall. Furthermore, theirs results indicate that the Sahel drought in the 1980s can be related to the change of the AMO to a negative phase.

While the dipole rainfall anomaly pattern is linked to regional changes of SST and SLP, the non-dipole pattern is more related to the global scale El Niño-Southern Oscillation (ENSO) [Ward, 1998]. Its warm phase is accompanied by reduced rainfall in the Sahel and higher SLP in the tropical North Atlantic. While July–September tends to be drier in the Sahel and Sudan regions during warm events, June and October tend to be wetter [Ward, 1998].

Other factors, which are influencing the intensity of precipitation, are for example aerosols. Haywood et al. [2013] have investigated the impact from stratospheric aerosols on the Sahelian rainfall. They have shown, while volcanic eruptions in the northern hemisphere lead to dry Sahelian summers, aerosol injections in the southern hemisphere result in an enhanced Sahelian precipitation. Furthermore, Ackerley et al. [2011] have analyzed the sensitivity of Sahel rainfall on greenhouse gas and sulfate aerosol forcing. Their results have shown that an increase of greenhouse gases cause an increase in precipitation while an increase in aerosols leads to a reduction. Moreover, on a more decadal time scale the climate variability in the Sahel is enhanced by vegetation and soil moisture feedback mechanisms [Zeng et al., 1999].

3.3.2 *Evolution over the Holocene*

Climate variability on orbital time scales is mainly forced by changes of the incoming solar radiation. Changes in insolation are described by the Milanković theory [Milanković, 1969]. The Serbian geophysicist and astronomer Milutin Milanković proposed how the cyclic variations in eccentricity, obliquity, and precession of the Earth collectively may control the long term evolution of the climate. The combination of these three parameters change the solar constant[1] by approx. 5% to 10%, which highly effects the spatial and intra-annual distribution of solar radiation.

- **Eccentricity** varies in two cycles, a 100,000 year cycle and a 413,000 year cycle. The eccentricity describe the deviation of the elliptic orbit with respect to a circle, by changes of it the Earth's orbit became more or less elliptic. Variations in eccentricity result in a change in the amount of solar radiation reaching the Earth at perihelion (Earth's nearest position to the sun) and aphelion (Earth's farthest position to the sun) position. Therefore, it influences the relative intensity of the seasonally incoming solar radiation. It has opposite effects on northern and southern hemisphere.
- The cycle of **obliquity** continues over 41,000 years. Obliquity describe variations on the tilt of Earth's rotation axis and varies within the range 22.2° and 24.5°. It changes the strength of the seasons. The strongest responses are noticeable in the high latitudes. Here, the effect on the northern and southern hemisphere is the same.
- The **precession** parameter describe the orientation of the rotation axis of the Earth and its shift follows an approx. 23,000 year cycle. Variations in precession results mainly in changes of incoming solar radiation in (sub)tropical regions, which are influencing the strength of seasonality in these regions. It has an opposite effect on the hemispheres.

Since the North-West African monsoon system is triggered by the different heating of ocean and land surface, most important for its variations on orbital time scales is the modification of the precession. During the early- and mid-Holocene, stronger summer and weaker winter insolation were occurring (Fig. 3.3, panel A). The stronger summer insolation amplified the differential warming between land and ocean and therefore the low pressure system over North Africa. This results in a strengthening of the North-West African summer monsoon (Fig. 3.3, panel B). Compared to the present, the weaker

1 The solar constant is the averaged intensity of solar radiation measured outside Earth's atmosphere and at Earth's mean distance from the sun.

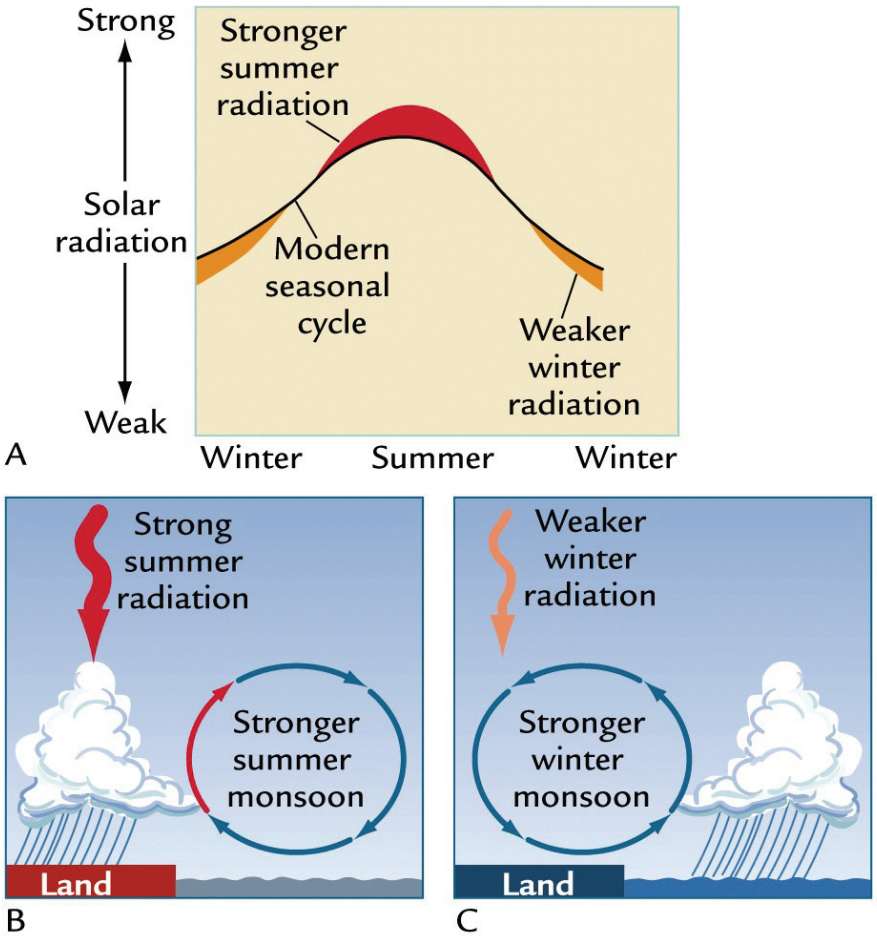

Figure 3.3.: Panel A: Modifications of the boreal seasonal cycle of insolation. Panel B: Influence of insolation on the summer monsoon. Panel C: Same as B but for the winter monsoon. [Ruddiman, 2008]

solar radiation during boreal winter induced cooler land surface temperatures. This, in turn, amplified the winter monsoon (Fig. 3.3, panel C). Consequently, the region of North-West Africa was wetter and more vegetated than today. [Ruddiman, 2008]

4

MODEL DESCRIPTION

Models give the opportunity to investigate single trigger of climate change or feedback mechanisms by changing initial or boundary conditions, and/or forcing factors. In general a GCM is a numerical model, which is representing the physical laws and processes which govern the climate. It can be distinguish between an atmosphere general circulation model (AGCM), a ocean GCM, and fully coupled atmosphere ocean models. In an AGCM, the atmosphere is split into a three dimensional grid (see Fig. 4.1), where for each grid box the following fundamental equations need to be solved: Conversation of energy, conversation of momentum, conversation of mass, ideal gas law, and the hydrostatic equation.

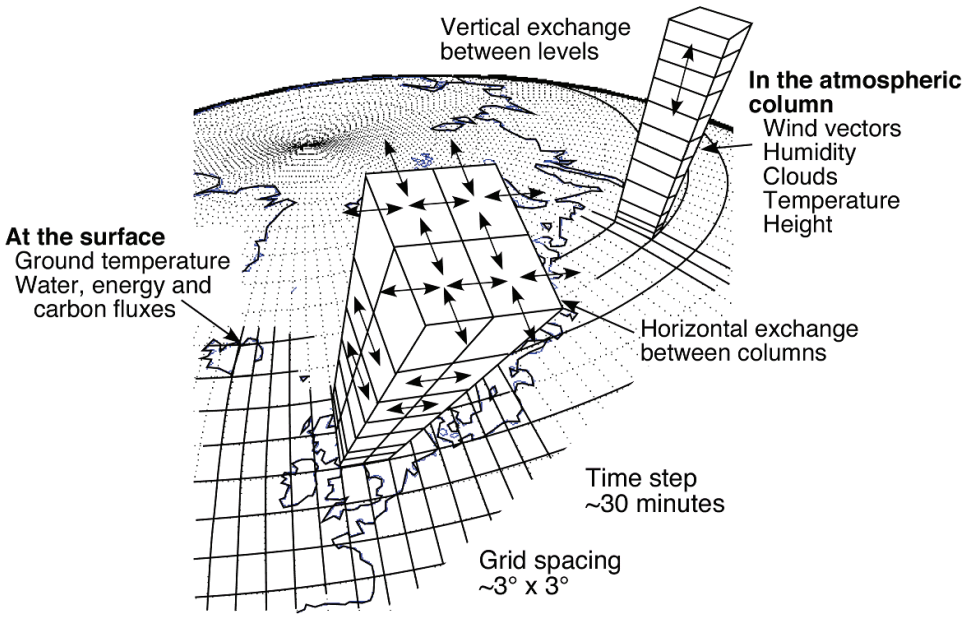

Figure 4.1.: Numerical principal of an atmosphere general circulation model [M. Werner, personal communication; after McGuffie and Henderson-Sellers, 2005].

The first two parts of this chapter introduce briefly the fully coupled (atmosphere-ocean-land surface) GCM COSMOS and the coupled atmosphere-land surface model ECHAM5-JSBACH. In Chapter 4.3, a detailed description of the isotope module embedded in ECHAM5-JSBACH, called ECHAM5-JSBACH-wiso, is given. The ECHAM5-JSBACH-wiso model has been developed within this work.

4.1 THE EARTH SYSTEM MODEL — COSMOS

The "Community Earth System Models" (COSMOS) describe a full coupled Earth system model with the components ECHAM5 as the atmosphere model, MPI-OM as the ocean model, and JSBACH as the land surface scheme. Each model component can be used also as a stand alone version. The atmosphere-ocean model ECHAM5-MPI-OM is described in Jungclaus et al. [2006]. The ocean component MPI-OM, in particular its numerical treatment, was introduced by Marsland et al. [2003]. For the full coupled model COSMOS the land surface scheme JSBACH [Raddatz et al., 2007] is embedded into the atmosphere model ECHAM5 and replaced the representation of the land surface from the stand alone ECHAM5 model. JSBACH including also a dynamic module for vegetation [Brovkin et al., 2009].

4.2 THE ATMOSPHERE-LAND SURFACE MODEL — ECHAM5-JSBACH

ECHAM5 is an AGCM, developed mainly at the Max Planck Institute for Meteorology, Hamburg, that consists of a spectral, dynamical core based on the equations of conservation of momentum, mass, and energy. This set of equations is completed by the hydrostatic equation, the continuity equation, and a prediction equation for the surface pressure [Roeckner et al., 2003]. The hydrological cycle in the model consists of the formulations for evaporation of ocean water, evapotranspiration of terrestrial water, two schemes for the formation of large scale and convective clouds, as well as an independent advective transport of vapor, liquid, and frozen water within the atmosphere. A detailed description of the physics of the model as well as changes to the earlier model version can be found in Roeckner et al. [2003].

For the coupled ECHAM5-JSBACH model, the JSBACH routines calculate the terrestrial boundary conditions for ECHAM5 over the land surface for each time step. This includes a simulation of the exchange of energy, water, and momentum between the land surface and the atmosphere. JSBACH is based on the ECHAM3 surface hydrology scheme [DKRZ, 1992], which is also used by ECHAM5, and the biosphere model "Biosphere Energy Transfer and Hydrology scheme", called BETHY [Knorr, 2000]. The basic idea of the model structure is a partitioning of the land surface. Each grid cell includes 8 tiles, which represent the fraction covered by one of the plant functional types (PFTs), distinguishing between tropical and nontropical as well as deciduous and evergreen trees, deciduous and evergreen shrubs, C3 grasses, and C4 grasses, as well as seasonally bare soil and permanently bare soil, i. e. desert [Raddatz et al., 2007]. The simulated vegetation is based on temporal change of growing, natural mortality, and disturbance

mortality (e. g. wind, fire). The modeling of vegetation and its dynamics are explained in detail by Brovkin et al. [2009].

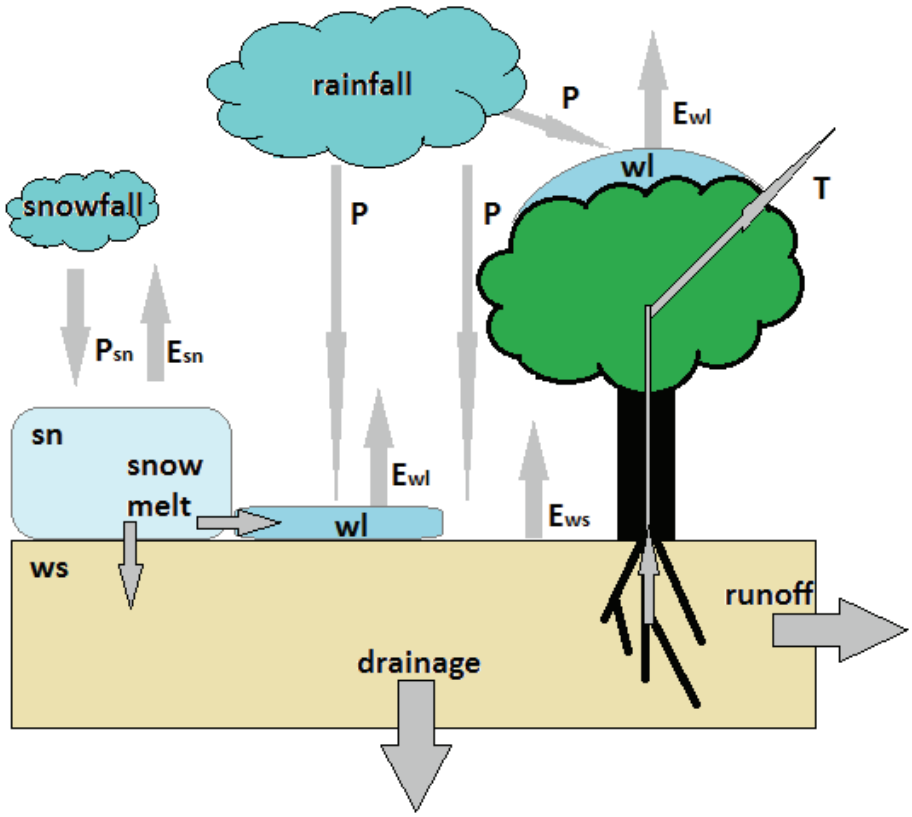

Figure 4.2.: ECHAM5-JSBACH soil scheme with the three water reservoirs: snow layer (*sn*), water at the skin layer (*wl*), and a soil water layer (*ws*). The incoming precipitation (P) can be distinguished in snowfall and rainfall. The water may leave a grid cell via evaporation (E) and transpiration (T), runoff, or drainage. The only water exchange between the water reservoirs occurs during snow melt.

In ECHAM5-JSBACH the same land hydrology model is used as in the stand alone version ECHAM5. The model comprises three surface water reservoirs: a snow layer (*sn*), water at the skin layer of the canopy or bare soil (*wl*), and a soil water layer (*ws*). These three types are each represented by a single layer bucket model, and the reservoirs *wl* and *ws* have a prescribed maximum field capacity. The snow reservoir is filled by snowfall and depleted by snow melt or sublimation. The skin layer and the soil layer are filled by rainfall and snow melt in the following order: first the skin layer is filled until its water holding capacity is exceeded, and secondly the non intercepted water fills the soil reservoir. The modeled depletion of the skin layer can only occur by evaporation, the depletion of the soil water reservoir occurs by evapotranspiration. There is no exchange between these two reservoirs. If the soil water reservoir is saturated, surface runoff occurs. Drainage occurs independent of the new precipitation, and it is calculated if the

amount of soil water reaches 5% or more of the maximal soil water capacity. The runoff respectively drainage scheme is based on examination of variations of the field capacity for soil water over the land surface [Dümenil and Tondini, 1992].

Furthermore, lakes are prescribed in ECHAM5-JSBACH by a lake mask. To calculate the evaporation over larger lakes (i. e., grid cells with a lake fraction greater than 50%) the same numerical scheme as for the ocean is used. A more detailed description of the land hydrology model can be found in Roeckner et al. [2003].

4.3 STABLE WATER ISOTOPES IN ECHAM5-JSBACH — ECHAM5-JSBACH-WISO

As in the stand alone atmosphere model ECHAM5-wiso the water isotope tracers in ECHAM5-JSBACH-wiso are implemented parallel to the normal water cycle. Fractionation of $H_2^{18}O$ and HDO versus $H_2^{16}O$ occurs during any phase change. Aside from fractionation during evapotranspiration from the land surface, all fractionation processes in ECHAM5-JSBACH-wiso are implemented in an identical manner to ECHAM5-wiso. For evaporation over the ocean, the bulk formula described by Hoffmann et al. [1998] is used. This equation includes the dependence of the isotope evaporation flux on the isotopic compositions of water vapor close to the ocean surface, evaporation temperature, relative humidity, and wind speed at the ocean surface [Hoffmann et al., 1998]. The implementation of fractionation processes inside the cloud schemes, specifically during cloud formation, are described in detail by Werner et al. [2011]. Furthermore, as in ECHAM5-wiso the assumption is used that convective showers generate primarily large raindrops equilibrating isotopically to only 45% as they fall through an undersaturated atmosphere, and that large-scale clouds generate smaller rain drops equilibrating nearly completely (95%) with their surrounding [see Hoffmann et al., 1998 for details].

Except for the process of evapotranspiration, the water isotope tracers are almost passive in the land surface scheme JSBACH. For example, during surface runoff and drainage the stable water isotopes are completely passive tracers and follow the normal water. The runoff is calculated as a composition of precipitation and snow melt. The same is valid for the calculation of its isotope ratio. The drainage has the isotopic composition of the soil water. It is also assumed that no fractionation during snow melt occurs. Thus, the melt water has the same isotopic composition as the snow. The melt water is added to the skin reservoir and the soil reservoir, respectively. After these reservoirs are filled the residual melt water is added to the runoff.

In order to calculate the evapotranspiration in ECHAM5-JSBACH, each grid cell is divided into four cover fractions: the fraction C_{sn} covered by snow, the fraction $(1 - C_{sn})C_{wl}$ covered with water in the skin reservoir, the fraction $(1 - C_{sn})(1 - C_{wl})C_{veg}$

covered by vegetation, and the fraction $(1 - C_{sn})(1 - C_{wl})(1 - C_{veg})$ covered by bare soil. The complete evapotranspiration flux is calculated by the weighted sum of evapotranspiration fluxes occurring over these four fractions. The evapotranspiration from the surface to the atmosphere is implemented with a negative sign convention. A positive flux can be interpreted as dew formation. In order to incorporate the stable water isotopes in ECHAM5-JSBACH the same convention is followed.

Water sublimates from snow at a potential evaporation rate, which is given by the following equation:

$$E_{sn} = \rho \, C_V \, |\vec{v}_h| \, (q_{vap} - q_{sat}), \tag{4.1}$$

with q_{sat} as the saturation specific humidity at the corresponding surface temperature, q_{vap} as the humidity of the air level direct above surface, $\vec{v}_h$ as the horizontal wind speed at the surface, C_V as the drag coefficient for water flux, and ρ as the density of air. Since the diffusion rate in the ice crystal structure is very low, it is assumed that no fractionation occurs during sublimation, which leads to the model assumption that the evaporative flux from snow has the same isotopic composition as the snow itself $\left(\frac{E^x_{sn}}{E_{sn}} = \frac{I^x_{sn}}{I_{sn}} = R^x_{sn}\right)$. (Here, and in the following paragraph I^x is used for the amount of an isotopic species and R^x for the ratio of a isotope species with respect to H_2O, with $x \in \left\{H_2^{16}O,\ H_2^{18}O,\ HDO\right\}$.) This assumption leads to the following equation for the isotope flux during snow sublimation:

$$E^x_{sn} = R^x_{sn} \, \rho \, C_V \, |\vec{v}_h| \, (q_{vap} - q_{sat}). \tag{4.2}$$

Analogously to Eq. 4.1 evaporation from the skin layer (wl) in ECHAM5-JSBACH is calculated as:

$$E_{wl} = \rho \, C_V \, |\vec{v}_h| \, (q_{vap} - q_{sat}). \tag{4.3}$$

The skin layer wl is modeled as a thin layer of water, which in general evaporates completely within a few model time steps. If this entire water reservoir evaporates, the total flux has an identical isotopic composition as the water source and no fractionation occurred. As this study focuses on temporal isotopic changes occurring over many time steps, for simplification is assumed that no fractionation occurs during evaporation from skin layer at any time step, which is expressed as:

$$E^x_{wl} = R^x_{wl} \, \rho \, C_V \, |\vec{v}_h| \, (q_{vap} - q_{sat}). \tag{4.4}$$

In ECHAM5-JSBACH, the following equation is used for the evaporation from bare soil (bs):

$$E_{bs} = \rho \, C_V \, |\vec{v}_h| \, (q_{vap} - h_{ws} \, q_{sat}), \tag{4.5}$$

with h_{ws} as the relative humidity of the soil surface [DKRZ, 1992].

To calculate the fractionation during evaporation over land surface the same bulk formula is used as described by Hoffmann et al. [1998]. To calculate the fractionation during evaporation, the equilibrium fractionation factor $\alpha^x(T)$, with T as surface temperature, obtained from Majoube [1971b], and a factor for kinetic fractionation (α_k) are used. Furthermore the mixing ratio of the water isotopes in the layer above the surface q^x_{vap} and the isotopic ratio of the saturation mixing ratio q^x_{qsat} analogue to Eq. 4.5 are needed. While $q^x_{vap} = R^x_{vap} \cdot q_{vap}$ is known in the atmosphere above the surface, q^x_{qsat} can be calculated with $q^x_{qsat} = R^x_{qsat} \cdot q_{sat}$. Here R^x_{qsat} is the isotopic ratio of the saturation specific humidity. If the equilibrium fractionation factor is used, R^x_{qsat} can be expressed by using the isotopic ratio of soil water with $R^x_{qsat} = \frac{R^x_{ws}}{\alpha^x(T)}$. So, the evaporation from land surface enhanced with fractionation is described by:

$$E^x_{bs} = \rho \, C_V \, |\vec{v}_h| \, \alpha_k \left(q^x_{vap} - \frac{R^x_{ws}}{\alpha^x(T)} \, h_{ws} \, q_{sat} \right). \tag{4.6}$$

The term α_k in Eq. 4.6 includes the non-equilibrium fractionation effects, taking into account the kinetics during the diffusion of vapor from a thin layer just above the soil water into the free atmosphere. For the calculation of the kinetic fractionation two different approaches are tested.

First, it is assumed, that the same kinetic fractionation factor as for evaporation over the ocean can be used over land as well:

$$\alpha_k = 1 - \lambda k \tag{4.7}$$

$$\text{with } k = \begin{cases} 0.006 & \text{if } |V_s| \leqslant 7[m/s] \\ 0.000285 \times V_s + 0.00082 & \text{if } |V_s| > 7[m/s] \end{cases}, \lambda = \begin{cases} 1 & \text{for } {}^{18}O \\ 0.88 & \text{for D} \end{cases}.$$

Here V_s is the horizontal wind speed at the surface and λ describes the ratio of the isotope molecular diffusivity in air. In this approach α_k is depending on the molecular and turbulent resistance of water vapor, and it has been described in detail by Merlivat and Jouzel [1979]. Typical values of α_k for H^{18}_2O range between 0.994 and 0.998, and according to Eq. 4.7 the values for HDO are slightly larger.

The second approach is presented by the study of Mathieu and Bariac [1996], where α_k is calculated as the nth power of the molecular diffusivity ratio in air:

$$\alpha_k = \left[\frac{d^x_v}{d_v} \right]^n, \tag{4.8}$$

with d_v (d^x_v) as the vapor diffusivity in air (vapor diffusivity of the isotopic species x). The exponent n includes the influence of the turbulent and molecular resistance. As

suggested by Riley et al. [2002], $n = 0.67$ is used in this study, which results in $\alpha_k = 0.981$ for $H_2^{18}O$ and $\alpha_k = 0.984$ for HDO.

The impact of these two different kinetic fractionation factors on the isotopic composition of the different modeled water reservoirs is analyzed and discussed in detail in Chapter 5.5.3.

Additionally to Eq. 4.6 a second approach for evaporation from bare soil is evaluated, based on the assumption that no fractionation during evaporation over land surfaces occurs. This leads to the modified formulation of Eq. 4.6 with:

$$\tilde{E}^x_{bs} = R^x_{ws}\ \rho\ C_V\ |\vec{v}_h|\ (q_{vap} - h_{ws}\ q_{sat}), \tag{4.9}$$

which is identical to the implementation of evaporation from bare soil in ECHAM5-wiso. This setup allows a comparison between the two models.

Since the hydrology inside the plants is not described by ECHAM5-JSBACH, the transpired water is modeled as a potential transpiration flux:

$$T = \rho\ C_V\ |\vec{v}_h|\ S^{-1}\ (q_{vap} - q_{sat}). \tag{4.10}$$

The factor S^{-1} is the transpiration efficiency, which includes among others the stomatal resistance of canopy. A detailed description can be found in DKRZ [1992]. Gat [1996] has shown that there is no isotopic fractionation as roots take up water. This leads to the model assumption that the isotopic composition of water inside the plants (R^x_{veg}) is identical to the isotopic composition of the soil water ($R^x_{ws} = R^x_{veg}$). If no fractionation occurring during transpiration is assumed, the transpiration isotope flux is calculated as follows:

$$T^x = R^x_{ws}\ \rho\ C_V\ |\vec{v}_h|\ S^{-1}\ (q_{vap} - q_{sat}). \tag{4.11}$$

To estimate the potential maximum fractionation effect for the combined evapotranspiration flux over land surface, an additional sensitivity study is performed. Here, the assumption is taken that the equilibrium fractionation occurs during both evaporation and transpiration. As the JSBACH model does not resolve the hydrology inside the plants and does not simulate the amount of leaf water, it is assumed that the whole amount of transpired water can fractionate. This leads to the altered Eq. 4.11:

$$\tilde{T}^x = \rho\ C_V\ |\vec{v}_h|\ S^{-1}\ \left(q^x_{vap} - \frac{R^x_{ws}}{\alpha^x(T)}\ q_{sat}\right). \tag{4.12}$$

It has to be kept in mind that this sensitivity study does not mimic the natural process of isotope changes during transpiration [e. g. described by Sachse et al., 2012]. Nevertheless, the study is rated as a useful simulation for estimating the upper limit of isotope changes related to the simulated evapotranspiration in ECHAM5-JSBACH-wiso.

5

MODEL-EVALUATION

In this chapter the model ECHAM5-JSBACH-wiso is evaluated. The first two sections describe the experimental setup and the observational data set. They are followed by the analysis of the spin-up period and the hydrological balance equation (Chapter 5.3) as well as the influence of coupling between the atmosphere model ECHAM5 and land surface scheme JSBACH (Chapter 5.4). The sensitiviy of fractionation processes over land is investigated in Chapter 5.5. The last section of this chapter discusses the results of the model evaluation.

5.1 EXPERIMENTAL SETUP FOR THE MODEL EVALUATION

All simulations used in Chapter 5 are run under present-day conditions with a prescribed vegetation distribution over a simulation period of 10 years after a spin-up period of 2 years. It is distinguished between the model resolutions T31L19 (horizontal grid size $3.8° \times 3.8°$, 19 vertical model levels) and T63L31 ($1.8° \times 1.8°$, 31 levels). The simulations are performed with AMIP-conform (Atmospheric Model Intercomparison Project) present-day boundary conditions including prescribed climatological sea surface temperatures and sea ice cover for the period 1979-1999 [see Taylor et al., 2000]. The lower oceanic boundary condition for the atmospheric ^{18}O isotopic composition is based on the data set described by LeGrande and Schmidt [2006]. This is a global gridded data set for sea surface water and sea ice. No equivalent data set is available for the composition of HDO. Therefor, the lower oceanic boundary condition for the isotopic composition of deuterium is derived from the observed relation for meteoric water on a global scale [Craig and Gordon, 1965] and it is assumed that $\delta D = 8 \cdot \delta^{18}O$ for sea surface water and sea ice.

To evaluate the sensitivity of the fractionation processes over land a set of present-day simulations with various fractionation schemes is performed. The fractionation process over land will be varied between no fractionation (simulation named noF, Chapter 4.3, Eq. 4.9 and 4.11), fractionation occurring during evaporation only (FE, Chapter 4.3, Eq. 4.6 and 4.11), and the idealized setup where fractionation occurs during both evaporation and transpiration (FET, Chapter 4.3, Eq. 4.6 and 4.12). These three cases are all performed without any additional kinetic fractionation ($\alpha_k = 1$).

In order to investigate the influence of the kinetic fractionation of terrestrial evaporation on the isotopic composition of the different water reservoirs the FE fractionation scheme is used and extended by two different calculations of the kinetic fractionation factor α_k. The first setup, called $\mathrm{FEK}_{openwater}$, uses the same kinetic fractionation factor over land surface as over the ocean (Chapter 4.3, Eq. 4.7). The second setup calculates α_{kin} in dependence on the diffusion resistance and is called $\mathrm{FEK}_{diffres}$ (Chapter 4.3, Eq. 4.8).

For a comparison of the ECHAM5-JSBACH-wiso results with them of the stand-alone ECHAM5-wiso model, two comparable present-day ECHAM5-wiso control simulations in T31L19 and T63L31 resolution [published in Werner et al., 2011] are used.

5.2 OBSERVATIONAL DATA

As observational data for evaluating the model results the Global Network of Isotopes in Precipitation (GNIP) database is chosen. Since 1961, the International Atomic Energy Agency (IAEA) and the World Meteorology Organisation (WMO) have collected monthly precipitation samples at more than 800 meteorological stations in 101 countries. Additional information and the available data can be found in IAEA/WMO [2006]. For this study 248 GNIP stations are chosen where isotope data has been recorded for at least three consecutive years within the time period 1961 to 2008, and where at least 10 months of data per year are available. As a further restriction, only stations are used, which provide a full monthly mean data set, including values of 2 m air temperature (T_{2m}), precipitation amount (P), and the isotopic composition of precipitation (hereafter named $\delta^{18}O_P$ and δD_P). One has to be aware that a period of three years is perhaps too short to represent a long-term climatological mean value at the stations' locations. On the other hand there are only 74 GNIP stations which have collected 10 years or more of data. Since most of them are located in central Europe, many regions in Asia, Americas, Africa, and Australia would be underrepresented in such a limited data set. Therefore a three-year time period is chosen in order to be able using a globally more representative sample distribution.

5.3 ANALYSIS OF THE SPIN-UP PERIOD AND THE HYDROLOGICAL BALANCE

5.3.1 *Spin-up period*

For all experiments in this chapter a spin-up period of two years is used. Figure 5.1 displays monthly mean values of the global amount of soil water and precipitation over

the simulation period of 10 years plus the two years spin-up time and the corresponding δ-values of the three implemented model setups noF, FE, and FET. It is shown that the simulated atmosphere reaches its equilibrium within the first simulation year, while the land surface reaches its equilibrium after the first two years. One could argue that there is still a small trend in the global values of $\delta^{18}O$ of soil water (hereafter named $\delta^{18}O_{ws}$) during the simulation years 3–5, but this trend is negligible for all findings in this study.

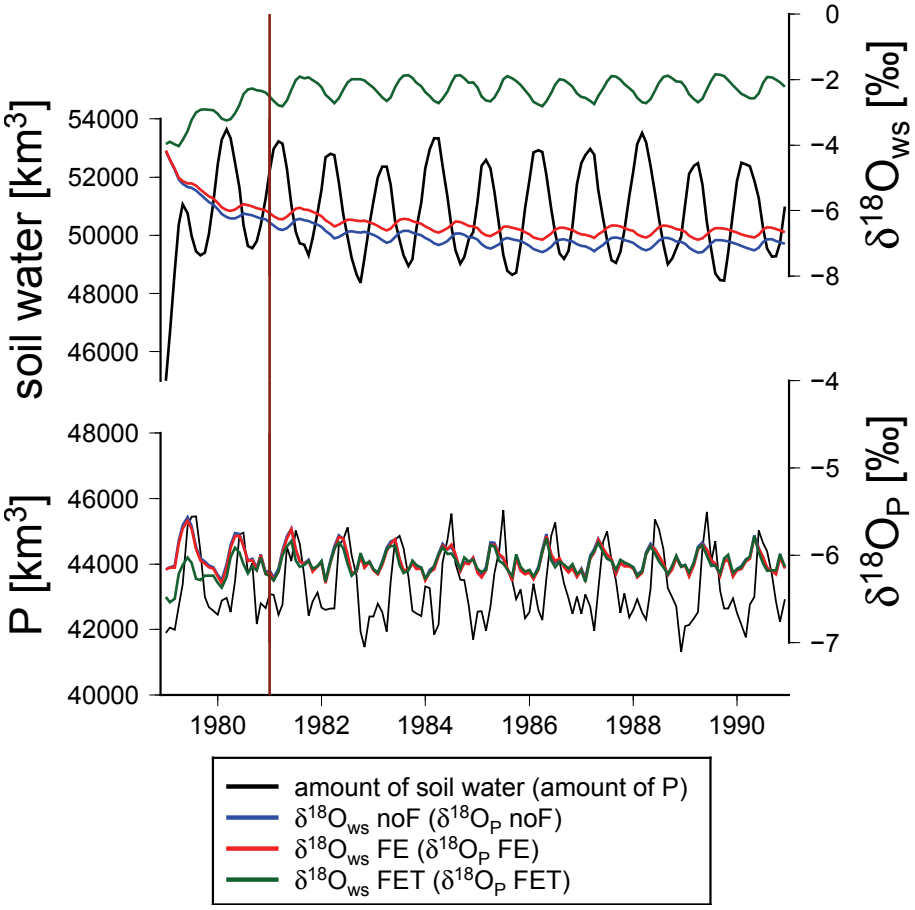

Figure 5.1.: (Top) Global amount of soil water (black) in [km^3] and it's isotopic composition $\delta^{18}O_{ws}$ for the noF-setup (blue), FE-setup (red) and the FET-setup (green) in [‰]. (Bottom) The same as in the top panel, but for precipitation. The ruby line marks the end of the spin-up period.

5.3.2 *Global water budget*

For an investigation of the hydrological cycle it is relevant to know, if the global water balance equation $precipitation = evapotranspiration$ is solved. In the ECHAM5-JSBACH-wiso model the global water balance equation is, with a deviation of less then 0.004% between precipitation and evapotranspiration, solved by the model (see Table 1).

The absolute amounts of $H_2^{18}O$ in precipitation and evapotranspiration correspond to an isotopic composition of -6.1‰ for all model setups.

		precipitation	evapotranspiration	deviation [%]
H_2O [km^3]		519356.000	521431.000	-0.003995
$H_2^{18}O$ [km^3]	noF	1035.080	1039.180	-0.003961
	FE	1035.080	1039.170	-0.003951
	FET	1035.080	1039.170	-0.003951

Table 5.1.: Global annual amount of precipitation and evapotranspiration for H_2O and $H_2^{18}O$.

5.4 IMPACT OF THE COUPLING FROM ECHAM5 AND JSBACH

To get an impression of how the overall model results change by using ECHAM5-JSBACH-wiso instead of ECHAM5-wiso first the simulated surface temperature, precipitation amount, and soil wetness results of both models are compared. All these variables are independent of the isotope diagnostic scheme, and differences between simulation results of both models are related to the changed representation of land surface processes in ECHAM5-JSBACH as compared to the stand-alone ECHAM5 model. Then, the simulated $\delta^{18}O_P$ is analyzed. As no fractionation for evaporation and transpiration processes has been assumed in the ECHAM5-wiso model by Werner et al., [2011], the analogous ECHAM5-JSBACH-wiso setup (noF) is used for this comparison.

5.4.1 *Surface temperature, precipitation amount, and soil wetness*

Figure 5.2a and 5.3a show the mean annual temperature and soil wetness as simulated by ECHAM5-JSBACH-wiso for the model resolution T31L19. The corresponding anomaly as compared to the comparable ECHAM5-wiso simulation is pictured in Fig. 5.2b and 5.3b. The modeled temperature difference varies from a $-2.7°C$ and $-1.4°C$ decrease over Antarctica and Greenland to a warming of $+0.5°C$ to $+2°C$ over Eurasia and North America. The strongest change is shown in North-East Russia with $+2.1°C$. These temperature changes are strongly related to the variation of the simulated surface albedo (Fig. 5.4a), which shows an increase over Antarctica as well as Greenland and a decrease over North America and Eurasia. For the finer resolution T63L31 (not shown) most of the anomaly pattern are similar. Only in some regions, due to the finer descrip-

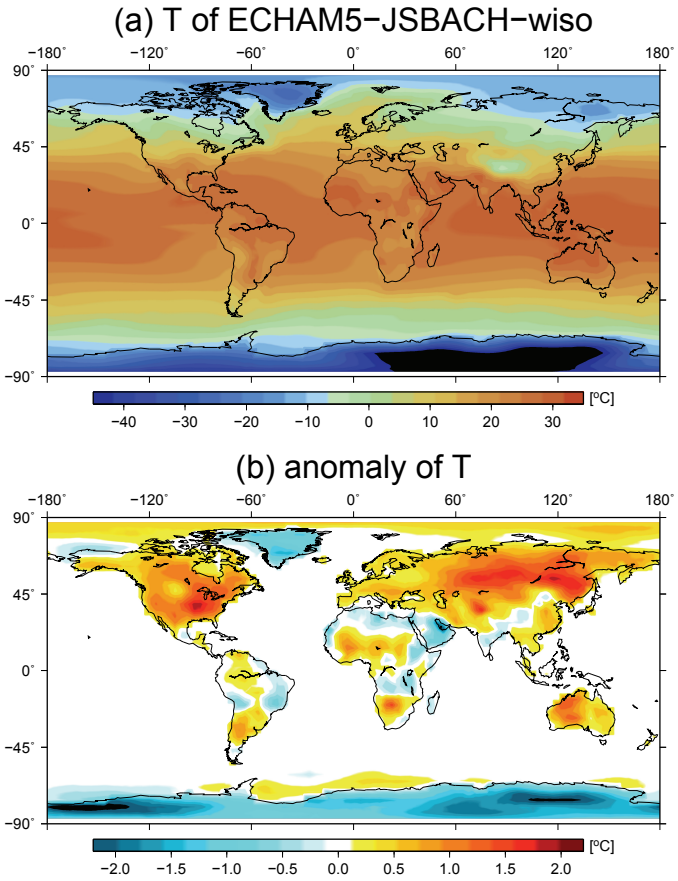

Figure 5.2.: Comparison of ECHAM5-JSBACH-wiso and ECHAM5-wiso at resolution T31L19: (a) the annual mean values of surface temperature (T) as well as (b) the anomaly between ECHAM5-JSBACH-wiso and ECHAM5-wiso are shown.

tion of regional attributes, deviations between the anomalies are detected. Simulated surface temperatures differ by 1°C, or less between the resolutions.

The simulated soil wetness differs between both models as well (Fig. 5.3b). The most notable changes are in the Amazon region, where an increase of 0.2 m is present, and in South Africa, where a decrease of 0.25 m can be seen. There is also a clear increase in a range of 0.08 m to 0.15 m over the Sahara. Most locations displaying a decrease in soil moisture generally show also an increase of evapotranspiration, which can be linked to changes in the simulated surface temperature. The increase of soil moisture in the Amazon region and the Saharan Africa can be directly linked to an increase of the prescribed maximum soil water capacity (Fig. 5.4b). This difference between ECHAM5-wiso and ECHAM5-JSBACH-wiso was introduced to enable a more realistic simulation of vegetation coverage over the tropical regions [Hagemann et al., 1999]. It was only introduced for the T31L19 resolution. Consequently, no similar soil water anomalies are found in the corresponding T63L31 simulation. Furthermore, in T63L31 a slight increase

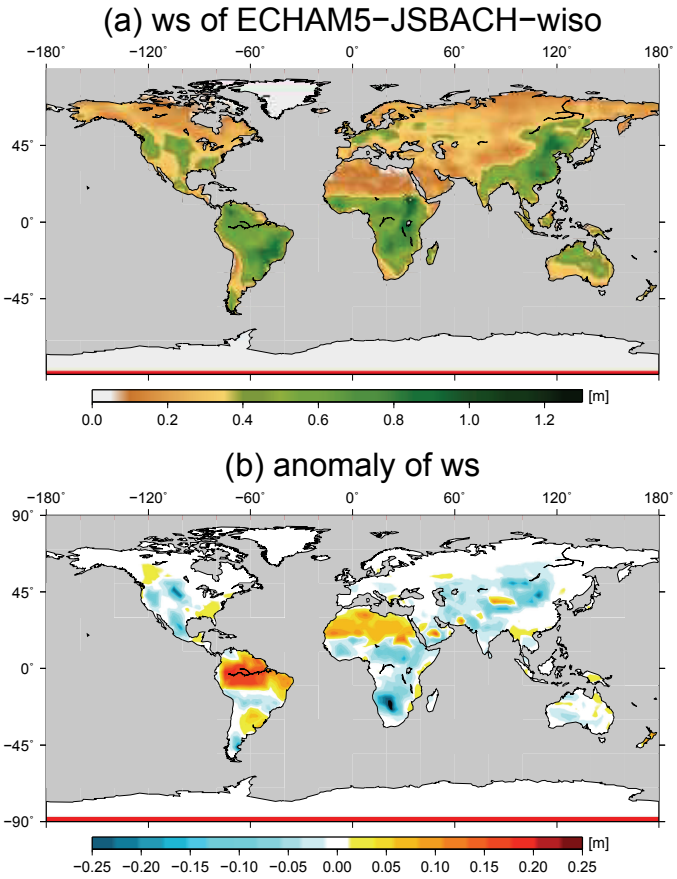

Figure 5.3.: Same as Fig. 5.2, but for soil wetness.

of soil wetness is simulated over Australia. This could be related to the finer resolution of albedo which results in a temperature change.

The simulated mean annual precipitation amount (not shown) shows nearly the same pattern in both models. For ECHAM5-JSBACH-wiso less annual mean precipitation in the range of 30-60 mm/month (which corresponds to 0.5–4% of the annual mean precipitation amount at the various locations) is simulated over middle and South Africa and over India.

5.4.2 *Isotopic composition of precipitation*

Figure 5.5 shows the simulated $\delta^{18}O_P$ using the noF setup (no fractionation during evaporation and transpiration) of ECHAM5-JSBACH-wiso for both model resolutions, T31L19 (Fig. 5.5a) and T63L31 (Fig. 5.5b). Both simulations depict the typical $\delta^{18}O_P$ pattern described by Dansgaard [1964]. One can see a depletion from the tropics to the high latitudes (temperature effect) as well as a depletion from the oceans to the land

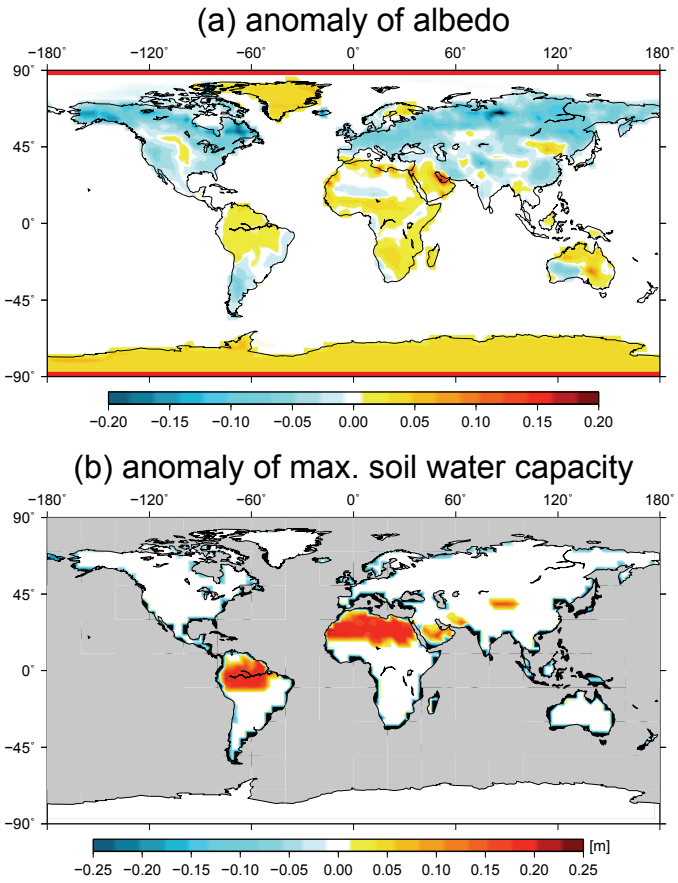

Figure 5.4.: Anomaly plot between ECHAM5-JSBACH-wiso and ECHAM5-wiso: (a) annual mean values of albedo, and (b) annual mean values of maximal soil water capacity.

masses of North America and Eurasia (continental effect). A depletion of $\delta^{18}O_P$ above the mountain areas can also be identified (altitude effect), for example for the Andes. However, Fig. 5.5b also shows that the altitude effect is better represented in the higher model resolution T61L31. The root mean square error (RMSE) between the simulations and the GNIP data is 2.15‰ for T31L19 and 1.78‰ for T63L31, which shows that the simulated $\delta^{18}O_P$ values generally improve for a higher ECHAM5-JSBACH-wiso model resolution. For the analogue simulations with the ECHAM5-wiso model the calculated RMSE with respect to the same set of GNIP stations is 2.25‰ for T31L19 and 1.89‰ for T63L31. Thus, both models show similar results for $\delta^{18}O_P$ on a global scale.

In order to further analyze the impact of the coupling of ECHAM5 with JSBACH for the simulation of stable water isotopes, the difference of $\delta^{18}O_P$ between the ECHAM5-JSBACH-wiso and the ECHAM5-wiso simulations is calculated for both resolutions (Fig. 5.6). Due to the relative short simulation period of 10 years, in the analysis of $\delta^{18}O_P$ changes in the range of -1‰ to +1‰ are excluded, as such small differences might be

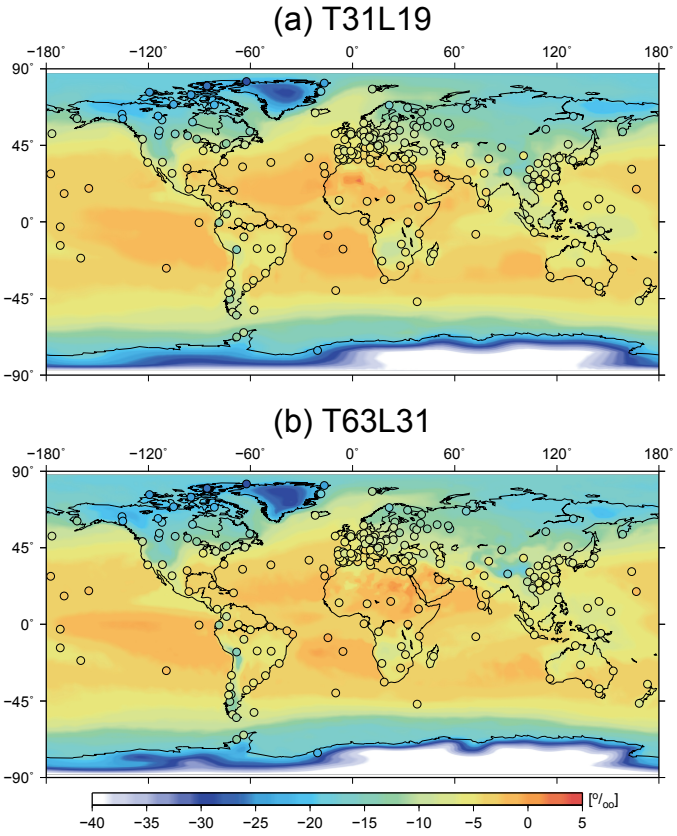

Figure 5.5.: Global map of observed $\delta^{18}O_P$ values (circles) and by ECHAM5-JSBACH-wiso simulated present-day annual mean $\delta^{18}O_P$ values (background map) for the model resolutions (a) T31L19 and (b) T63L31.

caused by internal model variability, only. For T31L19, the strongest differences with an increase up to approx. +4‰ are located in the region North Africa to the Arabian Peninsula. This anomaly can be related to a decrease in the amount of precipitation in ECHAM5-JSBACH-wiso related to ECHAM5-wiso. Negative anomalies, which are below -1‰, are only simulated in the high latitudes over Greenland, Antarctica and North-East Russia. Over Antarctica and Greenland the changes are most likely due to the different temperatures simulated in this region (see Fig. 5.2). The anomalies over North-East Russia can be linked to an increase of precipitation. Largest differences between the model resolutions are found for North-East Russia, wich is most likely linked to warmer temperatures and reduced regional precipitation in the T63L31 simulation.

For a further model evaluation the relationship between $\delta^{18}O_P$ and 2m temperature above the surface ($\delta^{18}O_P - T_{2m}$) as well as $\delta^{18}O_P$ and the amount of precipitation ($\delta^{18}O_P - P$) are investigated. For the $\delta^{18}O_P$-temperature relationship those 186 GNIP stations, where the annual mean temperature is below 20°C are used. Figure 5.7 displays

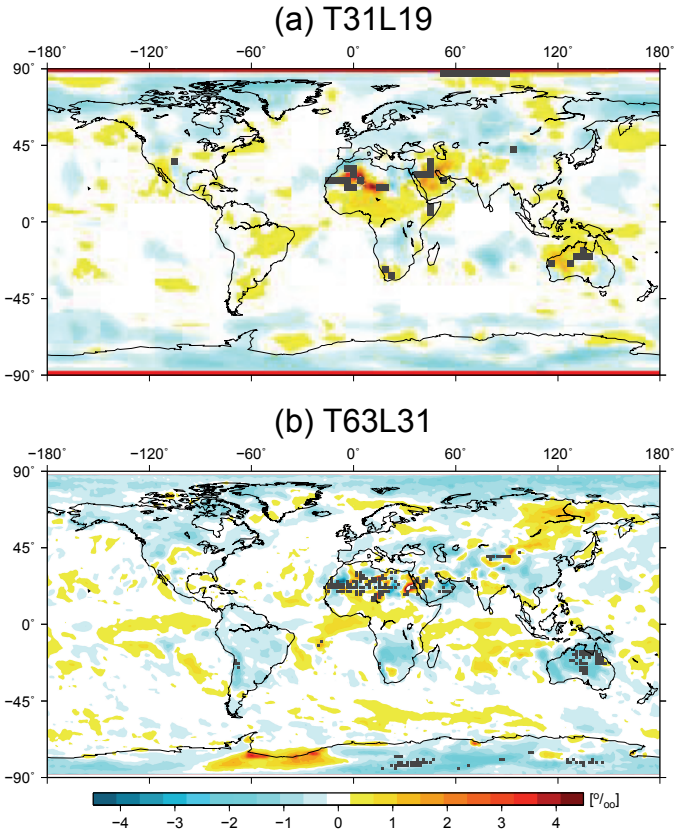

Figure 5.6.: Anomaly of ECHAM5-JSBACH-wiso - ECHAM5-wiso of annual mean $\delta^{18}O_P$ values for the model resolutions (a) T31L19 and (b) T63L19. The gray areas in the figures mark those grid boxes where the simulated interannual variability of ECHAM5-JSBACH-wiso or ECHAM5-wiso is larger than 2‰.

the simulated $\delta^{18}O_P - T_{2m}$ relation for both ECHAM5-JSBACH-wiso and ECHAM5-wiso. Both models show a similar $\delta^{18}O_P - T_{2m}$ relation as derived from the GNIP data, but slightly overestimate $\delta^{18}O_P$. The simulated strong correlation between $\delta^{18}O_P$ and T_{2m} in ECHAM5-JSBACH-wiso is statistically significant for both model resolutions (Pearson Correlation coefficient: $r = 0.816$ for T31 and $r = 0.845$ for T63), similar to the observed correlation at the GNIP stations ($r = 0.909$). As seen in Fig. 5.7, the simulated $\delta^{18}O_P - T_{2m}$ relation also slightly improves for the finer model resolution T63L31. For the correlation of $\delta^{18}O_P$ and precipitation 62 GNIP stations with a mean annual temperature above or equal to 20°C are chosen. The simulated relation fits quite well to the observed one for both model resolutions (Fig. 5.8) with a slight tendency to underestimate the $\delta^{18}O_P - P$ relation in the T31L19 resolution (both ECHAM5-wiso and ECHAM5-JSBACH-wiso). In this study it is refrained from a more quantitative analysis of the simulated $\delta^{18}O_P - T_{2m}$ and $\delta^{18}O_P - P$ relation as both the simulated and ob-

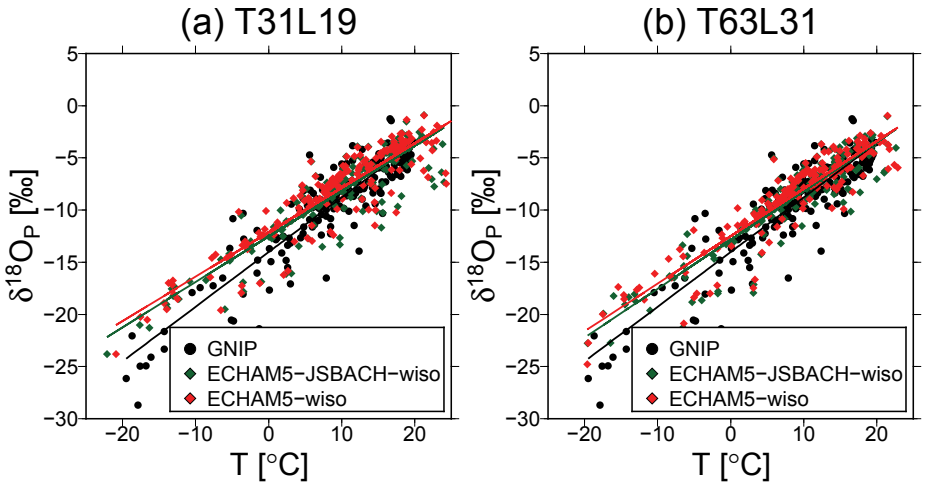

Figure 5.7.: Comparison of the simulated $\delta^{18}O_P - T_{2m}$ relation of ECHAM5-JSBACH-wiso (noF) with ECHAM5-wiso for the resolutions (a) T31L19 and (b) T63L31. For comparison with the observed relation, the data from those GNIP stations, where the annual mean temperature is below 20°C is used.

served mean $\delta^{18}O_P$, T, and P values may contain relatively large uncertainties due to the short simulation (10 years) and GNIP observation (3 years or more) period.

In summary, the analysis show that the coupling of the atmosphere model ECHAM5 with the surface scheme JSBACH has a detectable impact on the simulated temperature, evapotranspiration, and soil wetness. These changes are related to the alteration in the simulated surface albedo parameters and the prescribed maximum soil wetness. The simulated precipitation amount is less strongly influenced by the coupling. Since the isotopic composition of precipitation highly depends on these variables, the coupling of ECHAM5 with JSBACH also has a noticeable impact on the simulated $\delta^{18}O_P$ values in various regions. However, the analysis also reveal that the ECHAM5-JSBACH-wiso model is capable of simulating a global distribution of $\delta^{18}O_P$ in a good overall agreement with available observations from GNIP stations, similar to previous results retrieved with the stand-alone ECHAM5-wiso model [Werner et al., 2011].

5.5 FRACTIONATION PROCESSES OVER LAND SURFACES

In this part the sensitivity of the ECHAM5-JSBACH-wiso simulation results regarding different assumptions for both the equilibrium fractionation (Chapter 5.5.1 and 5.5.2) as well as the kinetic fractionation (Chapter 5.5.3) over land surface is investigated. All simulations in this part are performed at resolution T31L19.

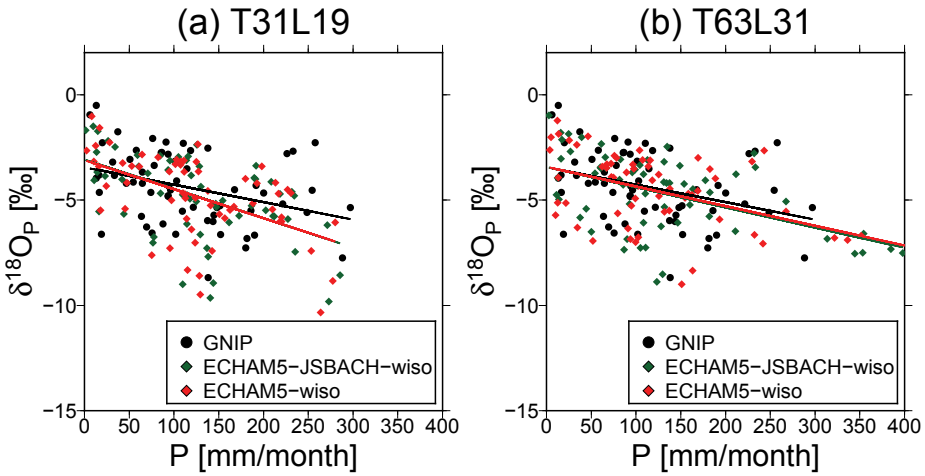

Figure 5.8.: Comparison of the simulated $\delta^{18}O_P - P$ relation of ECHAM5-JSBACH-wiso with ECHAM5-wiso for the resolutions (a) T31L19 and (b) T63L31. For comparison with the observed relation, data from those GNIP stations, where the annual mean temperature is above or equal 20°C are used. Please note that the linear fits of the ECHAM5-JSBACH-wiso experiment (green line) and the ECHAM5-wiso experiment (red line) are almost identical and strongly overlap in the plot.

5.5.1 *Equilibrium fractionation during evaporation and transpiration*

When water evapotranspirates from the land surface, it can evaporate from bare soil or skin layer, sublimate from snow, or transpire through the vegetation. According to Wang and Dickinson [2012], transpiration is the largest contributor to evapotranspiration on a global scale. This relevance of transpiration is also seen in the ECHAM5-JSBACH-wiso simulations. In Fig. 5.9 the modeled annual mean evapotranspiration flux from land surface (Fig. 5.9a) and the fraction of evaporation in relation to the total evapotranspiration flux (Fig. 5.9b) are shown. Especially in the (sub)tropical regions, transpiration is the dominant water flux from land surface to the atmosphere, while evaporation dominates over transpiration mainly in northern high latitude regions as well as the Tibetan Plateau.

For the incorporation of stable water isotopes in GCMs or land surface schemes various assumptions for the description of the equilibrium fractionation process during evapotranspiration have been utilized. In order to investigate the influence of fractionation processes over land surface on the isotopic composition of precipitation two extreme cases for transpiration are assumed in this sensitivity studies: For one model setup (named FE, see Chapter 4.3, Eq. 4.6 and Eq. 4.11) isotope fractionation is assumed during evaporation processes, only, and for another setup (FET, see Chapter 4.3, Eq. 4.6 and Eq.

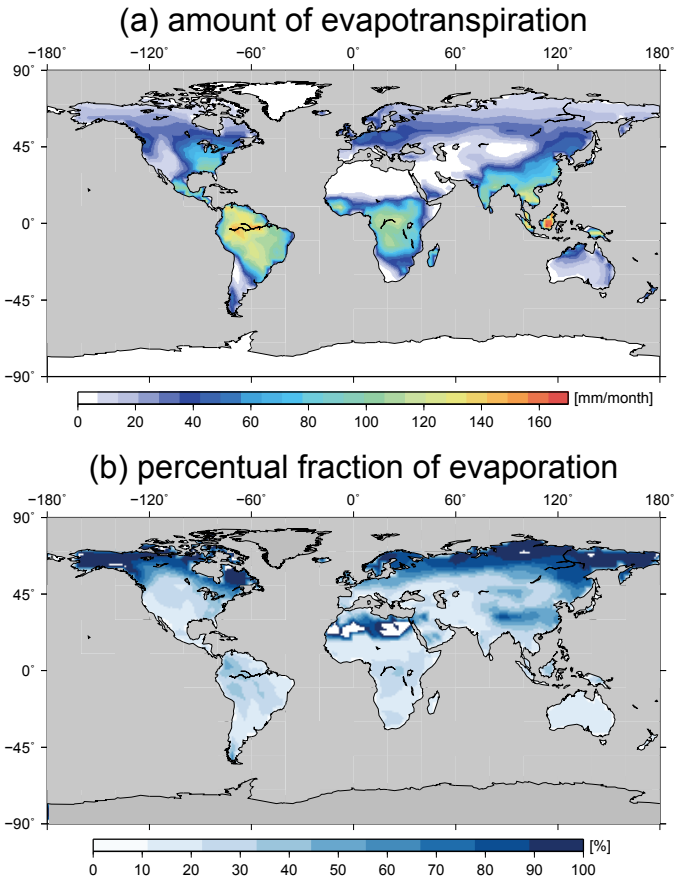

Figure 5.9.: Panel (a) shows the annual mean amount of evapotranspiration from land surface, and (b) the fraction of evaporation expressed as percentual amount of total evapotranspiration.

4.12) isotope fractionation is assumed for the complete simulated evapotranspiration flux. As a third case comparable to many previous GCM studies another setup (noF, see Chapter 4.3, Eq. 4.9 and Eq. 4.11) is examined in which no fractionation occurs during evaporation and transpiration, at all.

Figure 5.10 shows the anomalies of the modeled annual mean $\delta^{18}O_{ws}$ between the FE − noF (Fig. 5.10a) and the FET − noF setup (Fig. 5.10b). For the comparison of FE and noF (Fig. 5.10a) a relative stronger enrichment of $\delta^{18}O_{ws}$ is seen in the FE setup from 0.5‰ to 4‰ in regions with a relatively high evaporation rate (Fig. 5.9). The fractionation during evaporation leads to a relative depletion of near-surface vapor in the FE setup as compared to the noF setup. Due to this variation in vapor a slight depletion of $\delta^{18}O_P$ in the FE setup, compared to the noF one, ranging from -0.7‰ to -0.1‰ can be detected over the regions of North America, most parts of Eurasia, the Amazon region, and southern Africa (Fig. 5.11a). However, over the Tibetan Plateau and North-East Africa, the $\delta^{18}O_P$

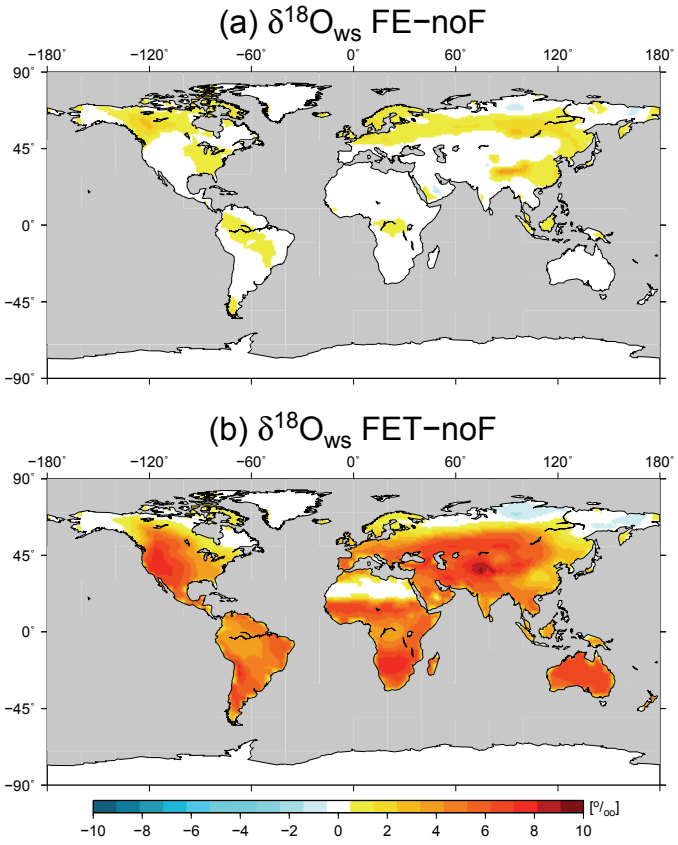

Figure 5.10.: Annual mean values of the simulated anomaly of $\delta^{18}O_{ws}$ for (a) FE − noF and (b) FET − noF.

in the FE setup is relatively more enriched than in the noF setup with differences in the range of 0.1‰ to 0.9‰. These enrichments are most likely a result of recycling of relative enriched local soil water. A detailed explanation, how local recycling may lead to positive anomalies, is given in Appendix A.

The anomaly plot of the isotopic composition of soil water of FET − noF (Fig. 5.10b) reveals a stronger enrichment of $\delta^{18}O_{ws}$ for the FET setup relative to the noF setup, as well as to the FE setup, over the tropics and mid latitudes. The range of this enrichment is 0.2‰ to 10‰. Only at North-East Russia a slight depletion of $\delta^{18}O_{ws}$ of approx. 0.1‰ in FET setup compared to noF setup is shown, which can be linked to the depletion of precipitation in this area. When using the FET setup instead of the noF one, a relative stronger enrichment of modeled annual mean $\delta^{18}O_P$ in the range of 0.1‰ to 0.8‰ is detected over the a region stretching from North Africa via the Arabian Peninsula to the Tibetan Plateau, South Africa, Central America, the Amazon region and North Australia (Fig. 5.11b). This enrichment is most likely caused by the recycling of the modeled enriched soil water due to the relatively high evapotranspiration rate at these areas (see

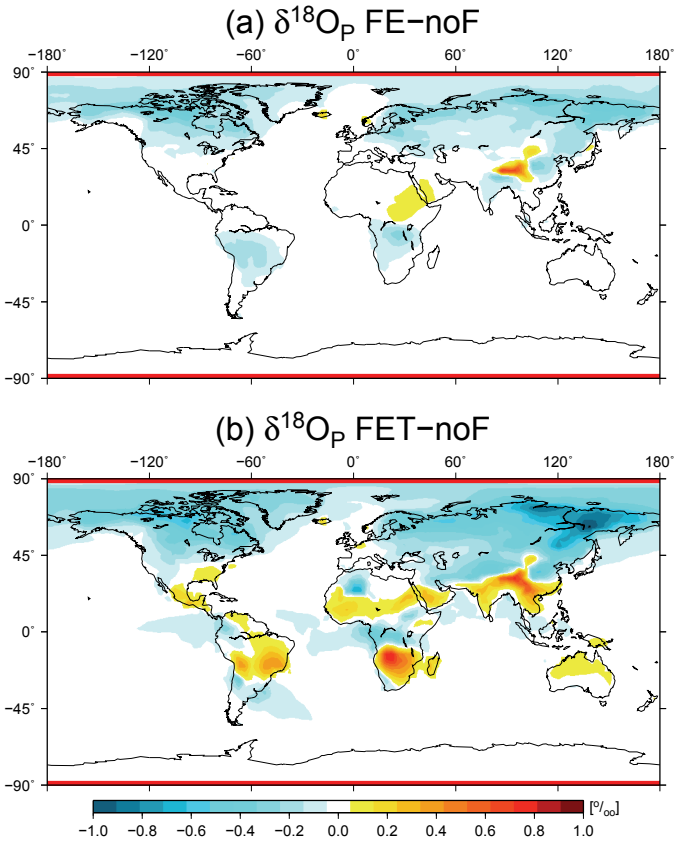

Figure 5.11.: The same as Fig. 5.10 but for $\delta^{18}O_P$.

also Appendix A). Furthermore, a stronger depletion of $\delta^{18}O_P$ from -1‰ to -0.2‰ is simulated over North America and North Eurasia, where the strongest anomaly is shown over North-East Russia.

Next, it is analyzed how accurately the different setups FE, FET, and noF simulate the $\delta^{18}O$ (δD) values in precipitation as compared to the various present-day GNIP observations. For this calculation, the set of 248 GNIP stations described in Chapter 5.2 is used and again it is distinguished between GNIP data of stations with a mean annual temperature $T < 20°C$ (Fig. 5.12a) and those stations with a mean annual temperature $T \geqslant 20°C$ (Fig. 5.12b). Table 5.2 shows the calculated correlation between simulated and observational values. For all three model setups, the calculated correlation between simulated and observational values is significant for $\delta^{18}O_P$ and δD_P (see Table 5.2) and very similar for all setups. However, Fig. 5.12a also shows that all three simulations overestimate $\delta^{18}O_P$ for most of these GNIP stations. A slightly different result is found for GNIP stations with $T \geqslant 20°C$ (Fig. 5.12b). For these stations, the $\delta^{18}O_P$ is in numerous cases underestimated in all setups.

Simulation Setup	$\delta^{18}O_p$		δD_p	
	r	RMSE	r	RMSE
noF ($T < 20°C$)	0.891	2.40	0.911	18.09
FE ($T < 20°C$)	0.892	2.38	0.911	17.84
FET ($T < 20°C$)	0.893	2.36	0.912	17.64
noF ($T \geqslant 20°C$)	0.769	1.34	0.768	11.15
FE ($T \geqslant 20°C$)	0.771	1.35	0.776	11.11
FET ($T \geqslant 20°C$)	0.769	1.30	0.766	10.91

Table 5.2.: Pearson Correlation Coefficient r and root mean square error RMSE of observed and by ECHAM5-JSBACH-wiso simulated $\delta^{18}O_p$ (δD_p) values.

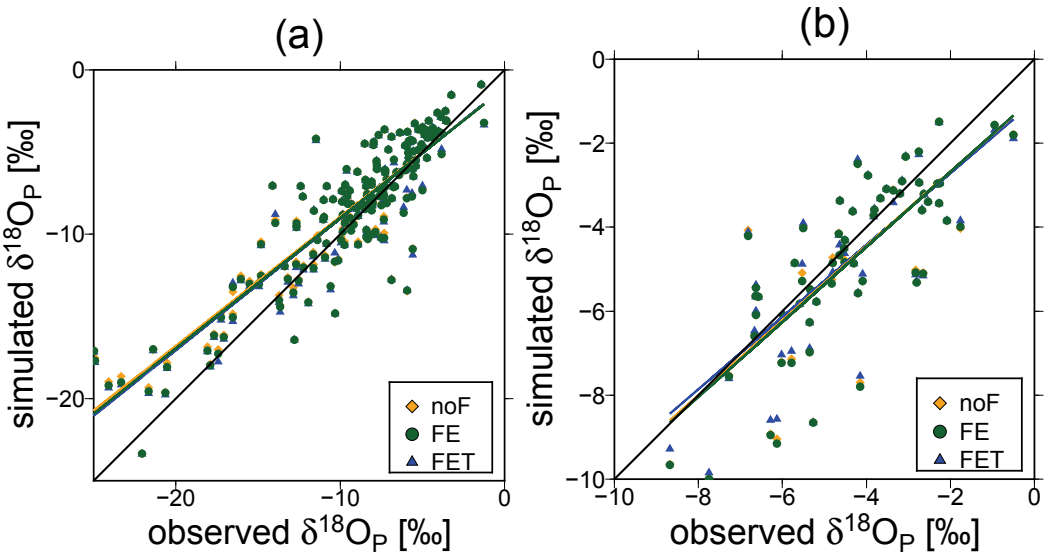

Figure 5.12.: Comparison of ECHAM5-JSBACH-wiso simulated and observational data of $\delta^{18}O_P$: (a) $T < 20°C$ and (b) $T \geqslant 20°C$.

5.5.2 *Seasonal changes due to equilibrium fractionation*

In order to get a more detailed picture regarding the modeled isotope variations, the seasonal cycle of the simulations using the FE, FET and noF model setup is analyzed. For this purpose nine GNIP stations from different geographical positions, which differ in the seasonal cycle of vegetation, amount of precipitation, surface temperature and the

influence of evaporation over land, are chosen and the ECHAM5-JSBACH-wiso results are compared to these GNIP data.

The first two stations are located on islands, where the influence of evaporation from the land surface is negligible in comparison to evaporation from the surrounding ocean. The station Reykjavik is chosen to represent the high northern latitudes and the GNIP station in Jakarta represents the tropics. Since the only distinguishing factor between the three model setups is the fractionation of evapotranspiration over land, one can assume, that the model behaves similarly in all implementations for the selected islands. For Reykjavik (Fig. 5.13a) all simulations reveal a correct seasonal timing of temperature, precipitation, and $\delta^{18}O_P$. While the simulated $\delta^{18}O_{ws}$ shows an enrichment of +2‰ in the FE and FET setup in comparison to the noF setup, the simulated $\delta^{18}O_P$ is very similar in the three setups. For Jakarta (Fig. 5.13b) the simulated evaporation and transpiration from land as well as the simulated soil wetness are undefined. While the simulated surface temperature is in a good agreement with the observed values in Jakarta, the simulated precipitation is strongly overestimated in the period April till July. The $\delta^{18}O_P$ has a correct timing of the seasonal cycle, but slightly too enriched values in fall. For all three model setups the calculated $\delta^{18}O_P$ is very similar.

As most regions of strong depletion in $\delta^{18}O_P$ varying between the different ECHAM5-JSBACH-wiso sensitivity experiments are in North America and Eurasia (as seen in Fig. 5.11) three stations of these regions are chosen for comparison: Vienna, Ottawa, and Yakutsk. At all these locations, strong seasonal variations of vegetation and temperature exist, but the amplitude of the temperature variations varies strongly.

At Vienna (Fig. 5.14a), the simulated temperature fits well with the observations, but the modeled precipitation shows an overestimation during winter and spring. For all three model setups, the $\delta^{18}O_P$ displays the correct seasonality but a slight offset in the range of +1‰ to +2‰ as compared to the GNIP values. Only in spring and summer the three simulations differ in a range of ±1‰. The simulated temperature also fits well in Ottawa (Fig. 5.14b), however all simulation setups overestimate the seasonality of precipitation. For $\delta^{18}O_P$, the simulation results have a correct seasonal timing, but all simulations overestimate the seasonal $\delta^{18}O_P$ amplitude, especially in summer. For Yakutsk, all model experiments reveal a correct timing of the seasonality for temperature, precipitation, and $\delta^{18}O_P$ (Fig. 5.14c). While the seasonal amplitude of temperature and $\delta^{18}O_P$ agrees well with the GNIP observations, the ECHAM5-JSBACH-wiso model simulates too much summer precipitation in this region. For the noF, FE, and FET model setups, the simulated $\delta^{18}O_P$ is very similar except of the summer, there a difference up to 1‰ is detected between the simulations. By comparison of the simulated soil wetness for the three GNIP stations Vienna, Ottawa, and Yakutsk, differences in the amplitude can be de-

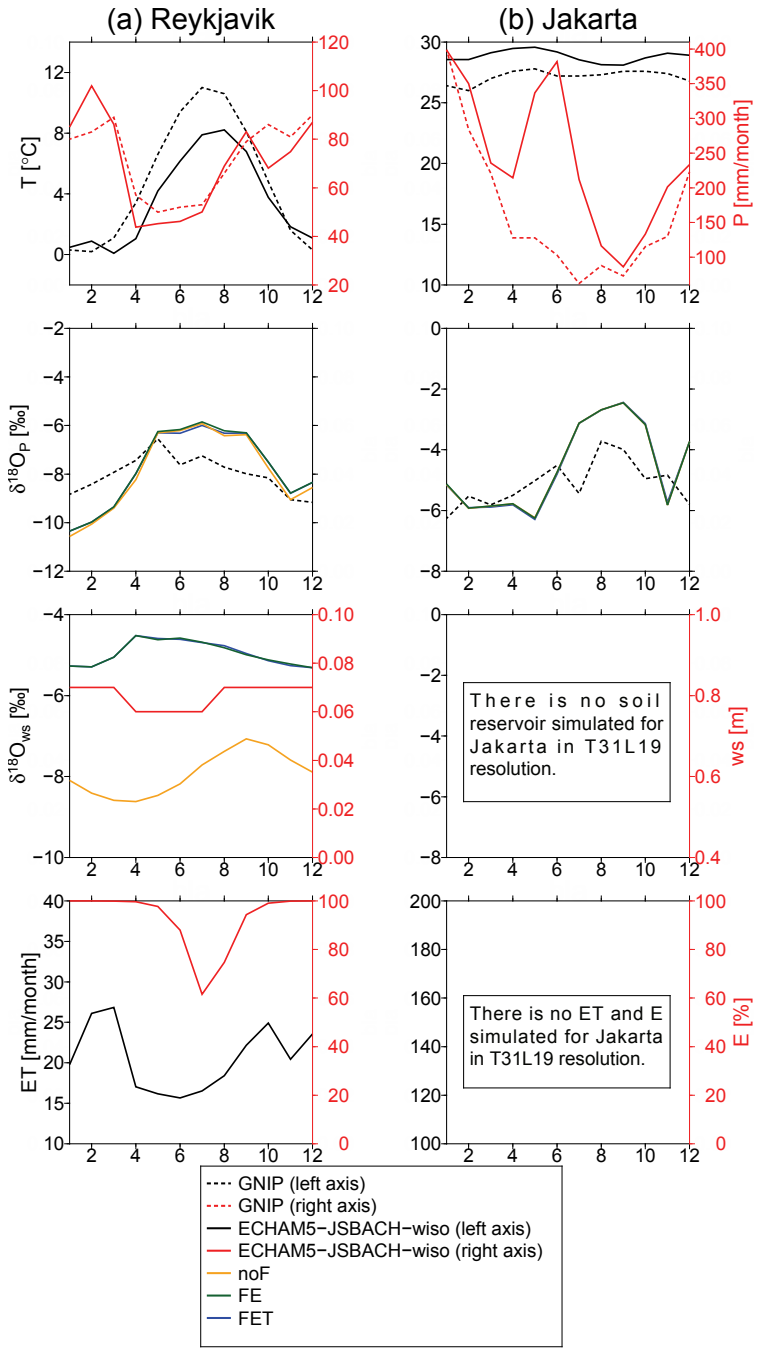

Figure 5.13.: Seasonal cycles of temperature T, precipitation amount P, isotopic composition of precipitation $\delta^{18}O_P$, isotopic composition of soil water $\delta^{18}O_{ws}$, depth of soil water bucket reservoir ws, evapotranspiration from land surface ET, and fraction of evaporation E for the locations (a) Reykjavik, (b) Jakarta. The dotted lines represent the observational GNIP values (left axis=black, right axis=red). For the simulations the black/red lines represent the simulated T, P, ET, ws and the fraction of evaporation E. The simulated $\delta^{18}O$ values in precipitation and the soil water bucket reservoir are the yellow (noF), green (FE) and blue (FET) lines.

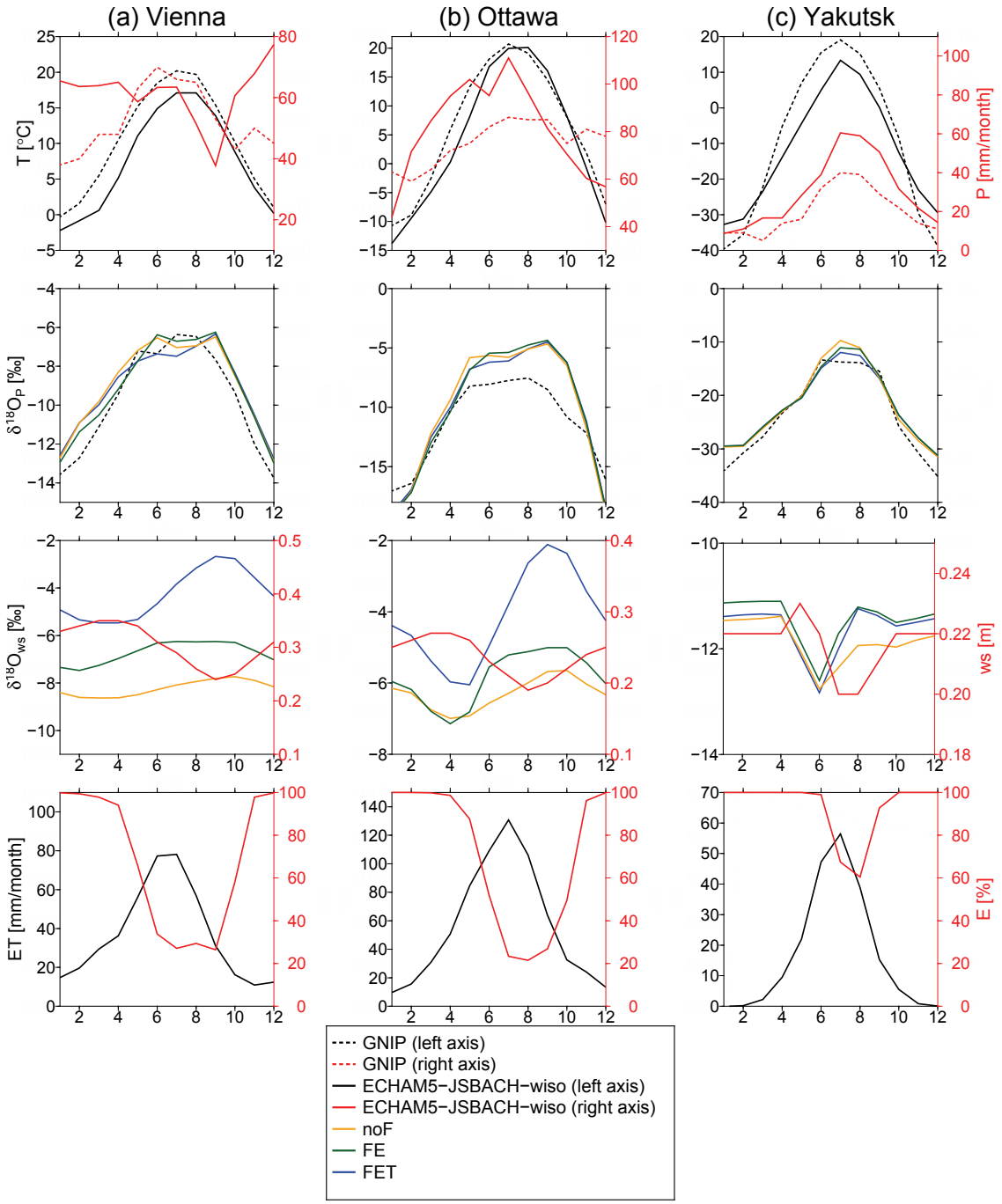

Figure 5.14.: As figure 5.13, but for the locations (a) Vienna, (b) Ottawa, and (c) Yakutsk.

tected. The calculated amplitudes of the seasonal changes of the soil water bucket depth are approximately 11 cm for Vienna, 8 cm for Ottawa, and 3 cm for Yakutsk, respectively. Furthermore, the time interval in which transpiration takes place varies for these three stations, the longest, with March to November, is simulated for Vienna, a similar range (April to November) is simulated for Ottawa, and for Yakutsk only an interval from June to October is calculated.

To analyze the model performance in arid areas or regions with strong seasonal precipitation changes, the stations Alexandria (Fig. 5.15a), Bamako (Fig. 5.15b), Kinshasa (Fig. 5.16a), and Addis Ababa (Fig. 5.16b) are examined. Alexandria is located in a very arid area with a dry season between May and September. This dry season is well simulated in ECHAM5-JSBACH-wiso, but the winter precipitation in the model is underestimated. Both temperature and $\delta^{18}O_P$ agree well with the GNIP observations with a slight overestimation of the simulated $\delta^{18}O_P$. Furthermore, the ECHAM5-JSBACH-wiso simulates a very thin soil bucket depth (approx. 0.05 m) as well as a very small evapotranspiration flux. While for FE and noF the simulated $\delta^{18}O_{ws}$ is nearly the same, the $\delta^{18}O_{ws}$ in the FET setup is approx. 0.5‰ heavier. For Alexandria all three simulations show the same weak seasonality for the isotopic composition of soil water. For Bamako (Fig. 5.15b), the simulated precipitation and temperature fit well with the observations. The simulated $\delta^{18}O_P$ values are approximately the same for all implementations, with too depleted $\delta^{18}O_P$ values in the dry season between January and May as compared to the GNIP data. The peak of the summer depletion is simulated with a delay of one month. For the soil water bucket depth, the ECHAM5-JSBACH-wiso model simulates a strong seasonality (from 0.4 m during the dry season to 0.85 m during the wet season), but the related $\delta^{18}O_{ws}$ values of the noF and FE setup display weak seasonal variations. Additionally, these two simulations have more or less the same $\delta^{18}O_{ws}$ values. Only for the FET setup, strong seasonal changes of $\delta^{18}O_{ws}$ are simulated.

Similarly to the situation at Bamako, the monthly model results of temperature and precipitation for Kinshasa (Fig. 5.16a) fit well to the observations. One major exception is an underestimation of the modeled precipitation amount in November. The simulation results reveal also a strong seasonality of the soil water bucket depth (from 0.20 m during the dry season to 0.40 m during the wet season). Again, the simulated $\delta^{18}O_{ws}$ values for FE and noF are more or less the same with weak seasonal variations, while the FET results show a strong seasonal cycle, inversely correlated to the seasonality of ws. Furthermore, the modeled $\delta^{18}O_{ws}$ values for the FET setup are stronger enriched by 3–8‰ when compared to the noF or FE setup. These differences of the noF or FE, and FET setup, in combination with the amount of evaporation, are directly imprinted in the simulated $\delta^{18}O_P$ values at the location Kinshasa. At Addis Ababa (Fig. 5.16b),

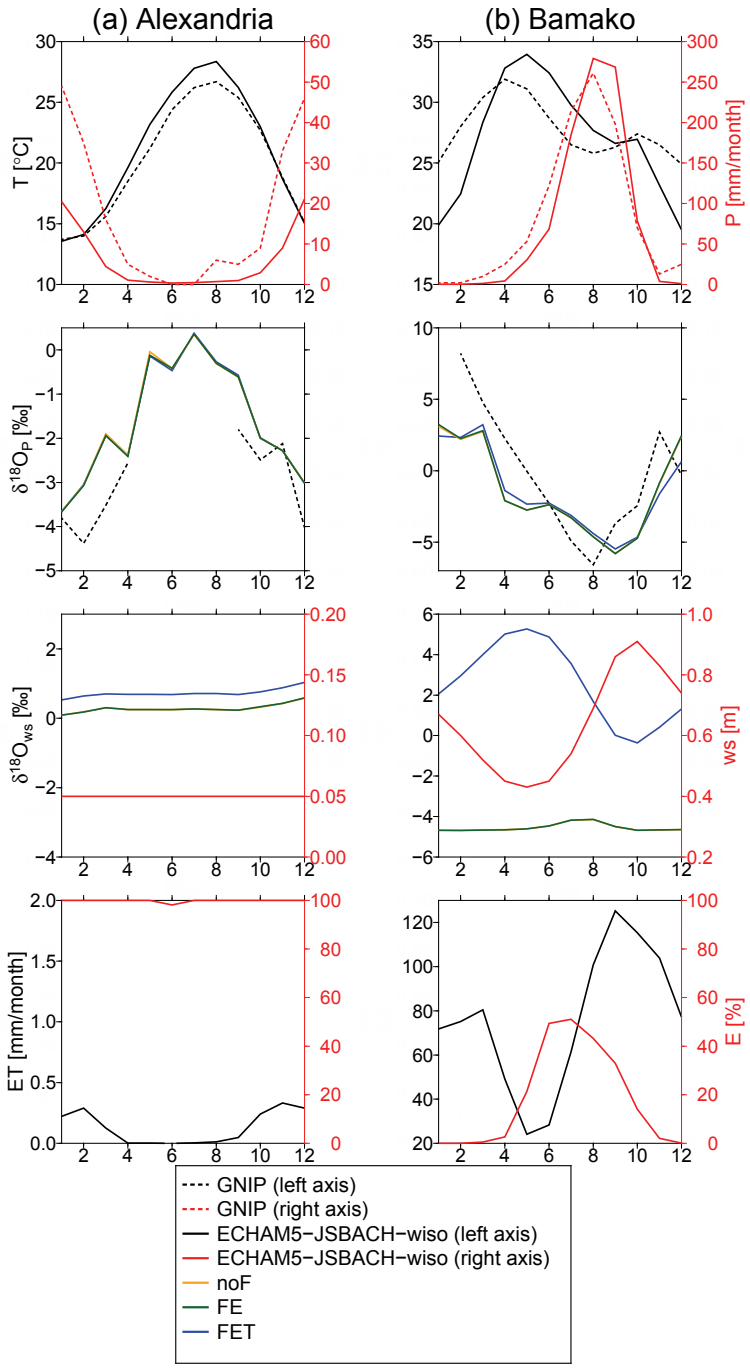

Figure 5.15.: As figure 5.13, but for the locations (a) Alexandria and (b) Bamako.

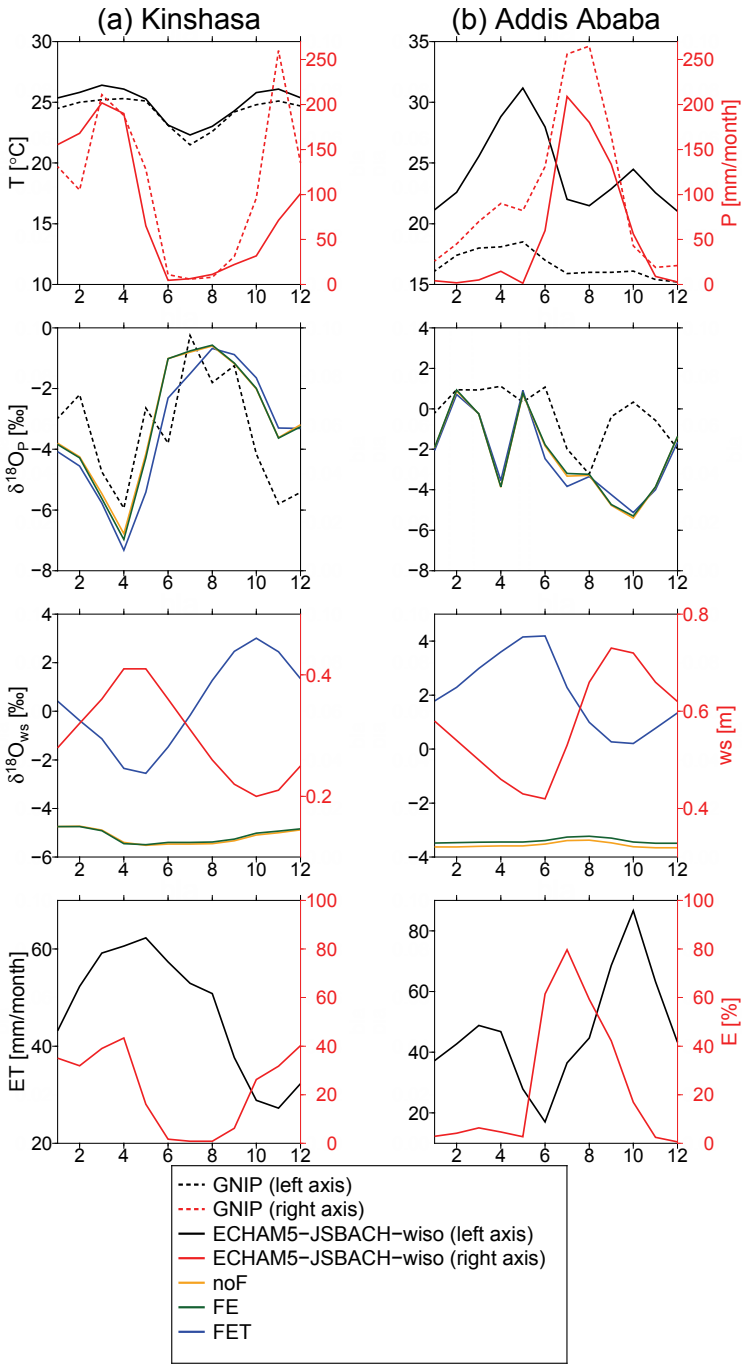

Figure 5.16.: As figure 5.13, but for the locations (a) Kinshasa and (b) Addis Ababa.

the simulated temperature is strongly overestimated by +5° to +12°C. Modeled precipitation values have a correct seasonal timing, but the amount of summer precipitation is underestimated. The simulated soil wetness also shows a strong seasonality, which lags the seasonal cycle of precipitation by 2 months. The modeled $\delta^{18}O_{ws}$ values are almost constant in the noF and FE setup, but the FET setup is slightly more enriched. While the FET setup shows seasonal changes in $\delta^{18}O_{ws}$ inversely correlated to the seasonal cycle of soil wetness, the simulated seasonal cycle of $\delta^{18}O_P$ in all model setups is more or less the same, but does not agree with the GNIP observations.

The performed sensitivity studies reveal that the various simulation results with the ECHAM5-JSBACH-wiso model are in relatively good agreement with the GNIP observations. In Fig. 9, it is shown that in many cases with a surface temperature $T \leqslant 20°C$ the model rather overestimates the isotopic values in precipitation while in cases with higher surface temperature ($T > 20°C$) the simulated values are more often underestimated. The incorporation of fractionation effects during evaporation and transpiration in FE and FET setup does not lead to substantial improvements for $\delta^{18}O_P$ as compared to the noF setup and the observations (Fig. 9, Table 5.2).

Part of the model mismatch is probably related to the rather simple one-layer bucket model of soil water, implemented in the coupled ECHAM5-JSBACH model. When using a simple bucket model for the soil water, the whole soil water reservoir does have an identical isotopic composition. Any vertical moisture dynamics and changes of the isotopic composition with the soil moisture depth are neglected. But it is well known from observations [see, e. g., Allison and Hughes, 1983; Hsieh et al., 1998] that strong vertical isotope gradients in soil can exist. Enrichment does mainly occur in the upper soil layers, while water in deeper soil layers, which can be used for plant transpiration, is more depleted. Thus, an one-layer bucked model will most likely result in too depleted isotope values of evaporated and too enriched isotope values of transpired water. Furthermore, in a previous study, Schulz et al. [2001] analyzed the results of coupling the ECHAM model with various land surface schemes of different complexity. They showed that a bucket model tends to calculate higher evapotranspiration amounts than more complex schemes. Such overestimation will result in a too strong influence of the isotopic composition of the soil water on the atmospheric isotopic composition, and consequently, on the isotopic values simulated in precipitation.

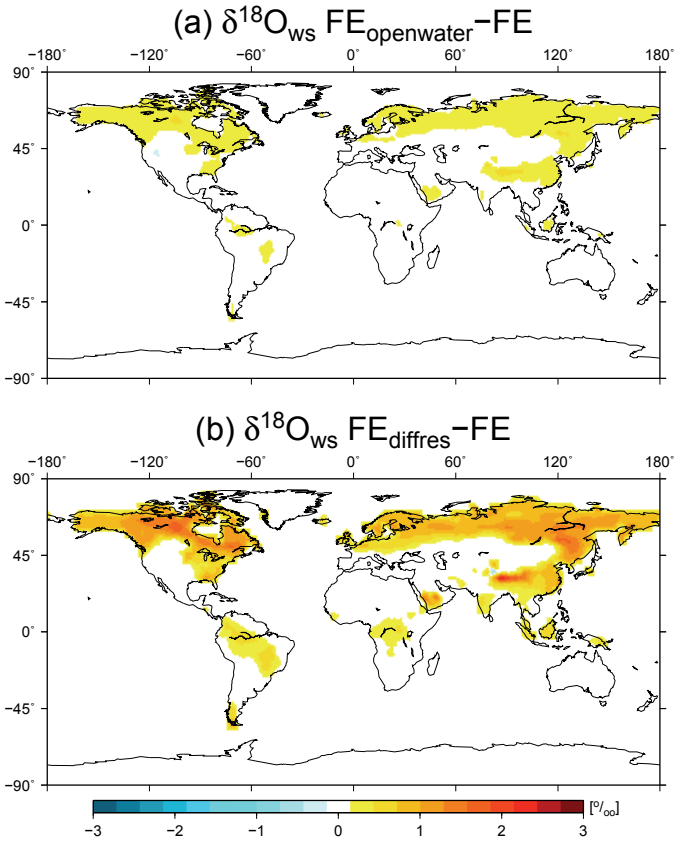

Figure 5.17.: Annual mean value of the simulated anomaly of $\delta^{18}O_{ws}$ for (a) $FE_{openwater} - FE$, (b) $FE_{diffres} - FE$.

5.5.3 *Sensitivity of kinetic fractionation*

In order to examine the influence of the kinetic fractionation coefficient α_k of terrestrial evaporation on the isotopic composition, the model setup FE (equilibrium fractionation occurring during evaporation only) extended by two calculations of the kinetic fractionation is used: For the first model setup (named $FEK_{openwater}$) the same kinetic coefficient as over the ocean (see Chapter 4.3, Eq. 4.7) is assumed, which is presented in the study given by Merlivat and Jouzel [1979]. The second setup ($FEK_{diffres}$) is based on the study given by Mathieu and Bariac [1996], where α_k is calculated as the nth power of the molecular diffusivity ratio (see Chapter 4.3, Eq. 4.8). As the third setup of the analysis the FE implementation is used, which has no kinetic fractionation included.

Figure 5.17 shows the anomalies of the simulated annual mean $\delta^{18}O_{ws}$ between the $FEK_{openwater} - FE$ (Fig. 5.17a) and the $FEK_{diffres} - FE$ setup (Fig. 5.17b). When using the $FEK_{openwater}$ or the $FEK_{diffres}$ setup instead of the FE one, a relative enrichment of $\delta^{18}O_{ws}$ in the range of 0.5‰ to 2.8‰ is detected in the areas where the evaporation

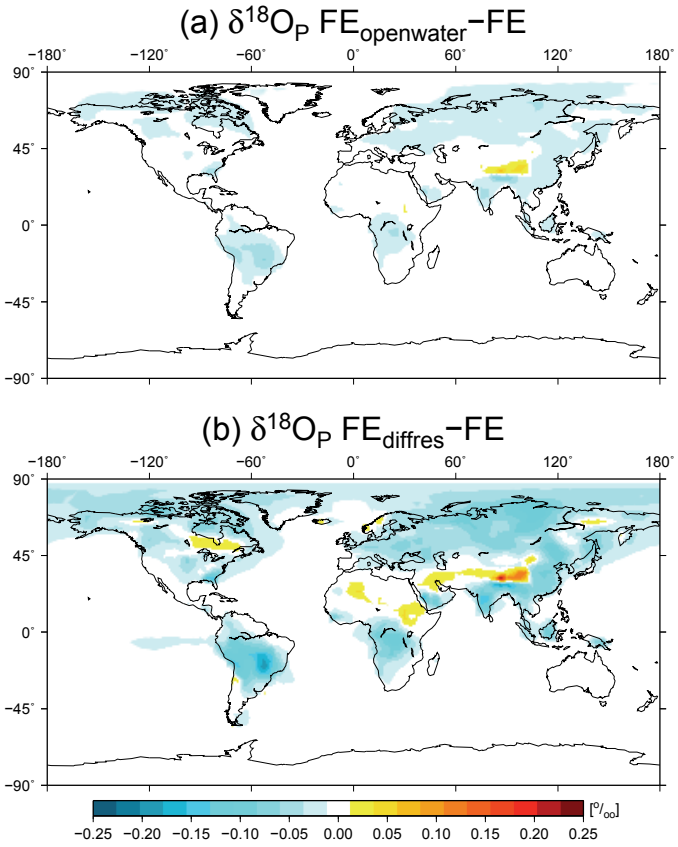

Figure 5.18.: Same as in Fig. 5.17 but for $\delta^{18}O_P$.

is relatively high (Fig. 5.9). Both setups, $FEK_{openwater}$ and $FEK_{diffres}$, simulate the strongest impact of the kinetic fractionation in the northern high latitudes, Amazon region, and southern Africa. This enrichment of soil water leads to a relative depletion of near-surface water vapor, as a result a stronger depletion of $\delta^{18}O_P$ is simulated for the setups including kinetic fractionation compared to the FE setup (Fig. 5.18). The anomaly of $FEK_{diffres} - FE$, with a depletion of -0.2‰ to -0.02‰(Fig. 5.18b), is stronger than the difference between $FEK_{openwater}$ and FE with a depletion in the range of -0.05‰ to -0.02‰.

Furthermore, the simulated $\delta^{18}O_P$ values as well as the simulated relation of δD_P and the deuterium excess (dex) are compared with the observational data. For these studies again those 248 GNIP stations described in Chapter 5.2 are used. Figure 5.19a depicts a comparison of the simulated annual mean $\delta^{18}O_P$ values with the observations. For all three model setups, the simulated $\delta^{18}O_P$ fits well with the observational values, but all three simulations overestimate the $\delta^{18}O_P$ for most of these GNIP stations. Moreover, Fig. 5.19a also shows that the calculated $\delta^{18}O_P$ is indistinguishable for the setups FE, $FEK_{openwater}$, and $FEK_{diffres}$. Figure 5.19b shows the simulated relation of δD_P and

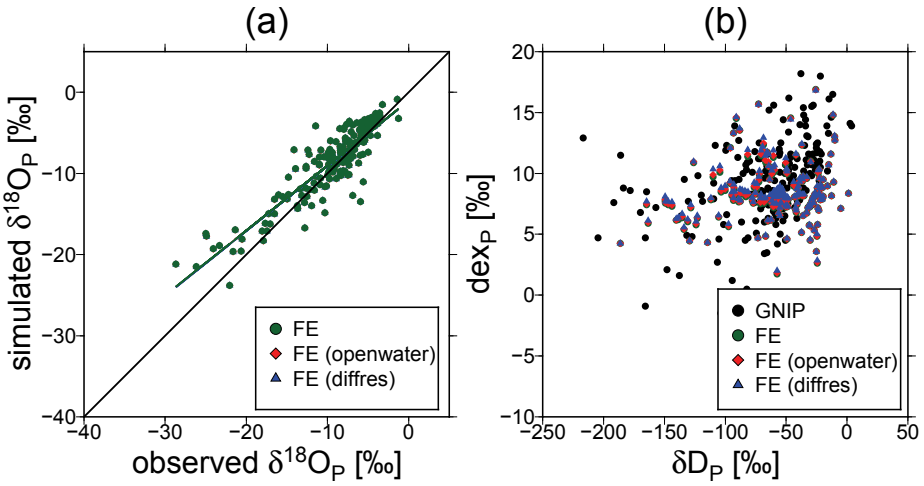

Figure 5.19.: Comparison of the kinetic fractionation factor for temperature below 20°C: (a) comparison of simulated and observed $\delta^{18}O_P$, and (b) relationship between Deuterium excess in precipitation (dex_P) and δD_P.

dex in precipitation (dex_P). It can be seen that the simulated $\delta D_P - dex_P$ relation behaves very similarly for all three setups and shows a similar distribution in comparison to the GNIP data.

The performed sensitivity tests for the kinetic fractionation factor α_k reveal that the setups FE, $FEK_{diffres}$, and $FEK_{openwater}$ of the ECHAM5-JSBACH-wiso model simulate a different isotopic composition of the soil water. The simulations have shown that the setup $FEK_{diffres}$ leads to the strongest fractionation in terms of $\delta^{18}O_P$ as well as in terms of dex_P (not shown). However, the simulations of $\delta^{18}O_P$ as well as at the simulation of the $\delta D_P - dex_P$ relation show no substantial difference between FE, $FEK_{diffres}$, and $FEK_{openwater}$.

5.6 CONCLUSION OF THE MODEL EVALUATION

The ECHAM5-JSBACH-wiso model is able to simulate the isotopic composition of precipitation ($\delta^{18}O_P$ and δD_P) in a comparably good manner as the stand-alone ECHAM5-wiso model. Furthermore it is demonstrated that the relation between simulated temperature and $\delta^{18}O_P$ and between precipitation and $\delta^{18}O_P$, respectively, is simulated in good agreement with the observations.

An analysis of the impact of the coupling of ECHAM5 and JSBACH reveals that the simulated land surface temperature and surface albedo are remarkably influenced by the coupled setup, which leads to some substantial regional changes of the hydrological cycle between the model ECHAM5-JSBACH and the stand-alone ECHAM5 model. This

results in differences of the modeled soil wetness and evapotranspiration fluxes between the two models.

To investigate the importance of isotope fractionation processes over land surfaces, three different model setups are used. The studies show that all three setups give relative similar results. All simulations including fractionation over land result in a slightly higher depletion of $\delta^{18}O_P$ of up to -1‰ for both the FE and FET setup. For the FET setup, an enrichment of $\delta^{18}O_P$ in the same order of magnitude can occur for some (sub)tropical regions. As an unrealistic fractionation of the total transpired water is assumed in the FET sensitivity studies, these enrichment effects are most likely much smaller (or even not existing at all) in reality. The inclusion of fractionation processes over land does not lead to a substantial improvement of the simulated $\delta^{18}O_P$ in ECHAM5-JSBACH-wiso (Table 5.2) on a global scale. As in most places $\delta^{18}O_P$ is in first order controlled by atmospheric processes, it would be expected that even with a highly realistic land surface scheme the simulated $\delta^{18}O_P$ would not substantially improve at such locations.

In contrast to the minor simulated changes of $\delta^{18}O$ in precipitation between the different model setups, differences of up to 5‰ for the FE setup (+10‰ for the FET sensitivity study) are simulated for the soil water reservoir in ECHAM5-JSBACH. At present, it is not possible to evaluate these simulated soil water changes by direct observations. A potential model-data comparison is hampered by the simple soil water scheme of ECHAM5-JSBACH. It is well known that the isotopic composition of soil moisture can strongly vary with depth [e. g., Allison and Hughes, 1983; Hsieh et al., 1998; Gazis and Feng, 2004]. But since in ECHAM5-JSBACH a one layer bucket model is used, it is not possible to simulate a vertical isotope profile within the soil. Thus, these simulation results can not be compared with available isotopic vertical profiles within the soil, yet. But such comparison should be possible for a more complex multi-layer soil scheme, which might be implemented in a future JSBACH model release.

Furthermore, recently started networks for isotopes in the biosphere, like Moisture Isotopes in Biosphere and Atmosphere (MIBA) or the Biogeosphere-Atmosphere Stable Isotope Network (BASIN), which monitor the isotopic compositions of soil water, have been operational for a limited time, so far. The available data does not represent long-term annual mean values, yet. But such data will hopefully become available during the next few years and will then allow a much more profound model-data comparison of the isotopic composition of soil moisture on a global scale.

6

VARIABILITY OF THE NORTH AFRICAN HYDROLOGY DURING THE 20TH CENTURY

The North-West African hydrology is subject to strong variations. The most recent shift in the hydrology occurred in the Sahel[1]. Nearly every year after 1968 the amount of annual precipitation was below the mean value of the 20th century (Fig. 6.1). Over large parts of this area the annual mean precipitation decreased by 30–40% relative to the long-term mean [Nicholson and Webster, 2007]. The reasons for this prolonged drought are not fully understood, yet. According to current knowledge, changes in the sea surface temperature (SST) and the resulting feedback mechanisms on the atmospheric circulation are important reasons [e. g., Ward, 1998; Nicholson and Grist, 2001]. However, changes of vegetation cover [e. g., Cadet and Nnoli, 1987] or in concentration of aerosols [e. g., Andreae, 1995; Ackerley et al., 2011] also play a role in the distribution of rainfall. More detailed information can be found in Chapter 3.

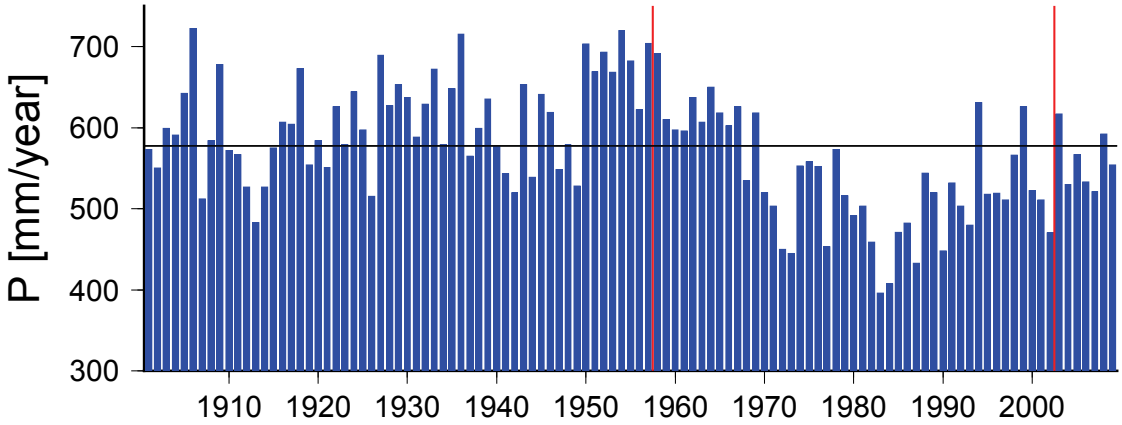

Figure 6.1.: Observed yearly precipitation from 1901 – 2009 [Harris et al., 2014] averaged over the area 20°W–10°E and 10°N–20°N. The time period between the red lines marks the simulation period and the black line marks the mean annual precipitation over the 20th century.

In this chapter an ECHAM5-JSBACH-wiso simulation, covering the period of time 1958–2002, is performed and its results are compared with climate re-analysis data [Dee et al., 2011], observational data [Harris et al., 2014; IAEA/WMO, 2006], and the compound-specific hydrogen isotope signal derived from sediment data [Beckmann

1 This chapter is focused on the West Sahel region, therefore in this chapter the wording 'West Sahel' is addressed to the area from 20°W–10°E and 10°N–20°N.

et al., 2013]. The aim is to answer the following questions: How well does the ECHAM5-JSBACH-wiso model simulate the present North-West African climatic conditions and its interannual variability? What do changes in δD in precipitation (δD_P) in the Sahel reveal about changes in amount of Sahelian precipitation? Is it possible, to infer quantitative changes of precipitation from the isotope signal of rain?

6.1 EXPERIMENTAL SETUP

To investigate the hydrological evolution over the last 50 years, an ECHAM5-JSBACH-wiso simulation, using the setup where no isotopic fractionation during evapotranspiration processes is assumed (Equations 4.9 and 4.11 in Chapter 4.3), has been performed with the resolution T63L31 (horizontal grid size $1.8° \times 1.8°$, 31 vertical levels). This experiment covers the simulation period 1956–2002; the first two years are used as spin up.

In order to produce highly realistic results, the ECHAM5-JSBACH-wiso model is nudged to the European Centre for Medium-Range Weather Forecasts (ECMWF) re-analysis data set ERA40 [Dee et al., 2011; Berrisford et al., 2009]. Every six model-hours the prognostic variables temperature, surface pressure, divergence, and vorticity are assimilated by linear relaxation (nudging) towards the ERA40 re-analysis data [Krishnamurti et al., 1991; implementation: Rast, 2013]. Additional boundary conditions are prescribed annual mean values of present-day greenhouse gases [IPCC, 2000] as well as reconstructed annual land use vegetation maps [Pongratz et al., 2007; description of reconstruction: Pongratz et al., 2008].

The lower isotopic oceanic boundary condition for the atmospheric ^{18}O is the same as described in Chapter 5.1. It is based on a data set described by LeGrande and Schmidt [2006]. The oceanic boundary condition for HDO is derived from the ^{18}O isotopic composition via the relation: $\delta D = 8 \cdot \delta^{18}O$ [Craig and Gordon, 1965].

6.2 OBSERVATIONAL AND PROXY DATA

The ECMWF re-analysis data set ERA40 [Dee et al., 2011] is used to evaluate the simulated climatology of North-West Africa. It consists of globally gridded climate variables, like temperature, precipitation, surface pressure, wind, or humidity, which are reconstructed from a large set of data, taking into account both, satellite data and instrumental measurements. The ERA40 data set covers the period from mid-1957 to mid-2002 with a spatial resolution of about $1° \times 1°$ (100×100 km).

In order to judge the evolution of the simulated amount of North-West African precipitation, the 0.5°×0.5° gridded Climatic Research Unit (CRU) TS3.10.01 data set of precipitation is utilized [Harris et al., 2014]. This CRU data set is based on monthly observations at meteorological stations distributed globally on land areas and covering the period from 1901 to 2009. Additionally, the simulated variability of δD_P is compared to the observational data provided by the Global Network of Isotopes in Precipitation (GNIP) [IAEA/WMO, 2006]. For this comparison the three Sahelian GNIP stations Bamako, Niamey, and N'Djamena are chosen.

As additional proxy data for the model-data comparison, the compound-specific hydrogen isotope values of land plant waxes derived from long-chain n-C_{31} alkanes are used (see also Chapter 2.4). This signal was measured in sediment multicore GeoB9501-4, which was retrieved at 16°50.38'N and 16°43.96'W in 330 m water depth [Mulitza et al., 2008], approximately 50 km north of the Senegal River mouth [Beckmann et al., 2013]. Beckmann et al. estimated the catchment area for the core data as the region 12°N–30°N and westward of 8°W.

6.3 SIMULATED MEAN CLIMATOLOGY

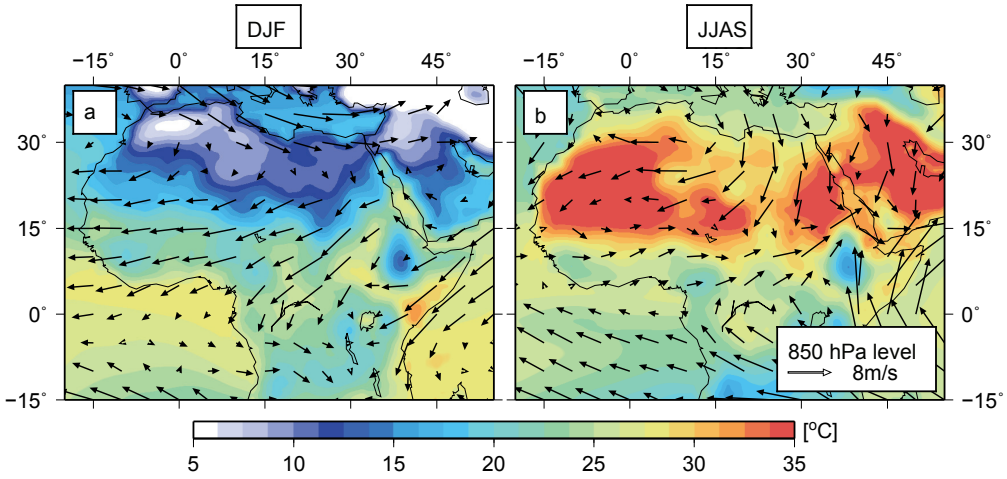

Figure 6.2.: Simulated mean surface temperature over the period 1958–2002 for (a) DJF and (b) JJAS (background map). The arrows depict the winds at 850hPa with respect to the season.

As mentioned in Chapter 3, the North African climate is highly dependent on the surface temperature pattern, which influences the atmospheric circulation and its seasonality. Figure 6.2 shows the simulated SST and the near surface winds for (a) December–February (DJF) and (b) June–September (JJAS). During boreal winter the North African

temperature increases from north to south with its maximum between 8°N and 15°N (Fig. 6.2a). While the North African coast is controlled by Mediterranean winds, the Sahara and Sahel region are governed by dry easterly winds. For the rainy season JJAS, the simulated temperatures illustrate a positive gradient from the Atlantic ocean to the Saharan desert (Fig. 6.2b). The West African monsoon flow, triggered by this temperature gradient, and the dry northeasterly Harmattan can also be identified in Fig. 6.2b.

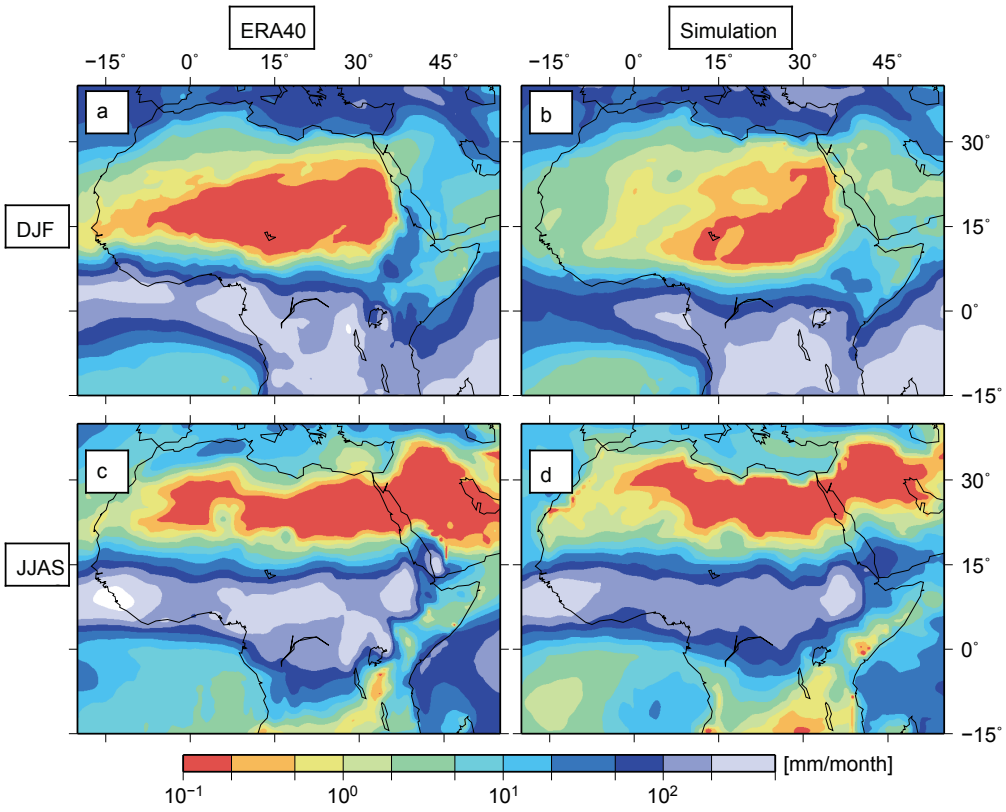

Figure 6.3.: Upper panels: monthly mean precipitation of the season DJF, for (a) ERA40 data and (b) ECHAM5-JSBACH-wiso simulation. Lower panels: same as upper panels, but for the season JJAS.

The simulated precipitation as well as the precipitation from the ERA40 data set, for boreal winter and summer, are presented in Fig. 6.3. While, during boreal winter, the North African coast is influenced by Mediterranean winds which bring some precipitation, the South Sahara and the Sahel are governed by dry easterly winds. In contrast to the ERA40 data the ECHAM5-JSBACH-wiso model tends to simulate too humid conditions over the western part of the Sahara and Sahel. Furthermore, the simulated African winter rain belt is approx. 5° further south than the observed one. During JJAS, the by ECHAM5-JSBACH-wiso simulated climate over the western part of South Sahara and

Sahel is wetter as compared to the ERA40 data set. However, the simulated African summer rain belt is too narrow and too weak compared to the observed one.

One possible reason for the poor simulation of the African rain belt could be the internal description of cumulus clouds in the model, which are a main contributor to the precipitation during JJAS [Dallmeyer, 2008]. Dallmeyer has proposed that in simulations performed with a vertical resolution of 31 level, compared to coarser vertical resolutions, the melt layer at approx. 600 hPa is relative well represented, which results in a high stability of this level. Thus, the cumulonimbus clouds can not penetrate easily into the upper troposphere. As a consequence the cloud cover at the mid troposphere increases, which yields in a cooling due to the increased water vapor. A further effect is that the cloud cover in the upper troposphere is reduced, which causes a decreased absorption of solar radiation. This in turn results in an additional cooling of the air [Roeckner et al., 2006]. Due to these cooling effects, the air has a smaller water saturation coefficient, which induces less water vapor transport and precipitation [Dallmeyer, 2008]. While over oceans the simulated precipitation becomes more realistic by increasing the vertical resolution [Hagemann et al., 2006], the simulated precipitation for the Sahel zone is too low as compared to observations [Dallmeyer, 2008].

Figure 6.4 shows the mean δD_P over (a) DJF, (b) the rainy season JJAS and (c) the year averaged over the period 1958–2002. Both seasonal δD_P pattern (Fig. 6.4a and b) illustrate the negative correlation between δD_P and amount of precipitation (which is also seen in Fig. 5.15 for DJF in Alexandria and for JJAS in Bamako). During boreal winter a relatively depleted δD signal, most likely caused by heavy Mediterranean rainfalls, can be detected at the North African coast and northern Sahara (Fig. 6.4a). Contrastingly, the δD signal of the rainy season in the Sahel (Fig. 6.4b) is dominated by the influence of the North-West African summer monsoon. Here, the relation between amount of precipitation and δD_P is most likely governing the δD signal (Fig. 6.4b), which is a common feature in the monsoon areas over the world [Rozanski et al., 1993]. However, during JJAS the simulated δD_P increases along the monsoon flow (Fig. 6.4b), which is inverse to the continental effect as observed e. g., in Europe [Cuntz et al., 2002]. Furthermore, the weighted long term means of GNIP stations also show a similar gradient, with -31‰ at Bamako, -27‰ at Niamey, and -21‰ at N'Djamena. One possible reason for this gradient could be an increased evaporation during rainfall [Gasse, 2002]. Another explanation could be the enriched recycled moisture from the African rainforest [Gasse, 2002], which is an important water source for the summer monsoon [Cadet and Nnoli, 1987]. The described seasonal effects can also be detected in the annual mean values (Fig. 6.4c).

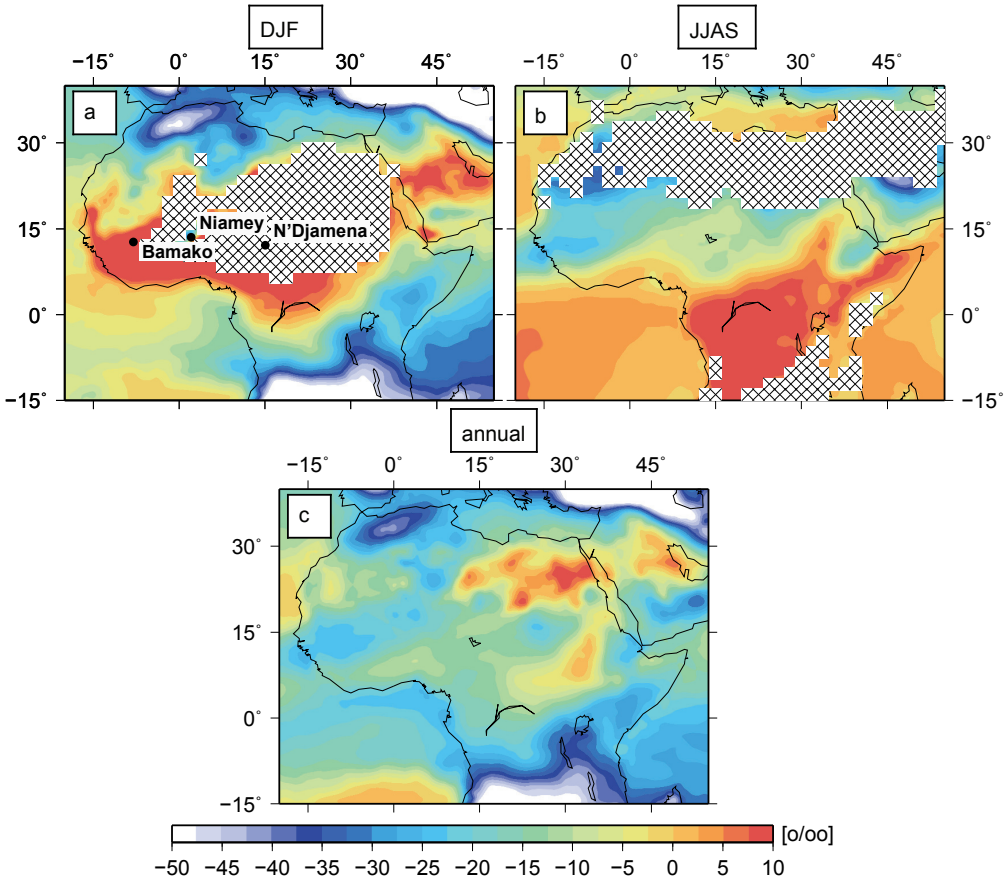

Figure 6.4.: Mean δD_P over the seasons (a) DJF, (b) JJAS, and (c) annual of North Africa, averaged over 1958–2002. The hatched areas mark regions where the mean precipitation during the time is less then 1 mm/month.

6.4 INTERANNUAL VARIABILITY IN PRECIPITATION

6.4.1 *Comparison between observed and simulated precipitation and its isotopic composition*

The chronology of monthly precipitation and δD_P at the Sahelian GNIP stations Bamako, Niamey, and N'Djamena are compared with the simulated ones in Fig. 6.5. The simulated precipitation (lower panels of Fig. 6.5) has the correct seasonal timing for all three stations, but the amount of precipitation during the wet seasons tends to be underestimated by the model. This agrees with the findings by Dallmeyer [2008], who has shown that ECHAM5 (resolution T63L31) simulates only 70% of the precipitation, averaged over the area 30°W–40°E, 0°N–32°N, observed by the Global Precipitation Climatology Project (GPCP). Nevertheless, the simulated δD_P (upper panels of Fig. 6.5) show a good agreement in amplitude and interannual variability with the observed GNIP values.

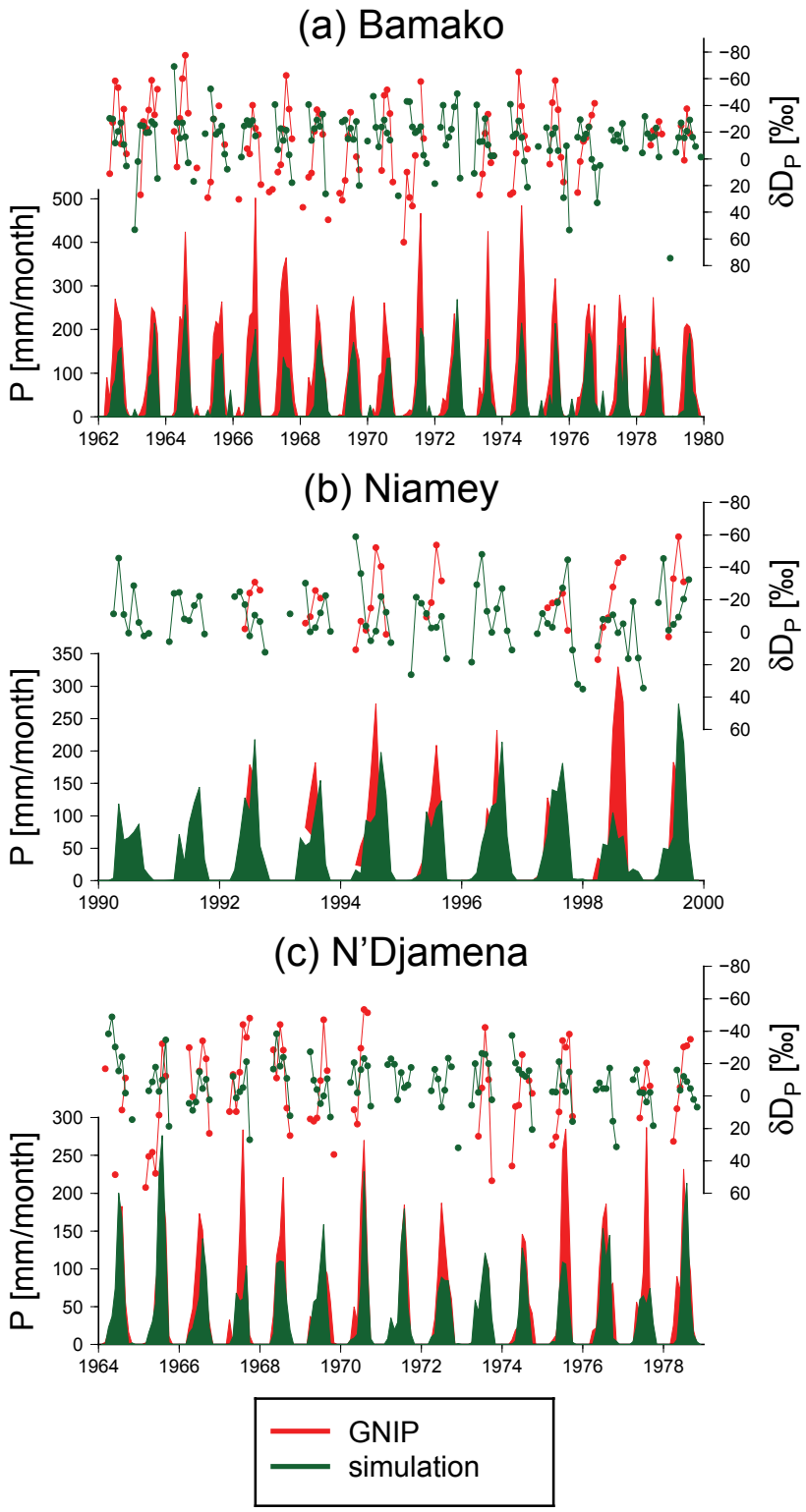

Figure 6.5.: Precipitation amount P (colored areas) and isotopic composition of precipitation δD_P (lines) for the locations (a) Bamako, (b) Niamey, and (c) N'Djamena. Red values represent the observational GNIP values and green values the simulation results.

6.4.2 *Simulated dry and wet year pattern*

In the literature, two common different rainfall anomaly patterns are described [e. g., Ward, 1998; Nicholson and Grist, 2001; Nicholson and Webster, 2007; see review in Chapter 3.3.1]:

1. a dipole pattern with the pivot at approx. 10°N, which results in abnormally wet (dry) conditions in the Sahel region and dry (wet) conditions at the Guinean Coast (called dipole wet (dry) Sahel mode);

2. a non-dipole pattern with abnormally wet (dry) conditions over the West Sahel and the Guinean Coast region (called non-dipole wet (dry) mode).

In this part of the study, it is tested whether the model is able to simulate these patterns and which influence the patterns have on the δD_P signal. Therefore, the simulated JJAS rainfall anomalies are classified into the anomaly patterns (see Appendix B), and for each configuration the year with the most pronounced anomaly pattern is chosen for this analysis.

Figure 6.6 shows the JJAS rainfall anomalies of 1961 (dipole wet Sahel mode), 1988 (dipole dry Sahel mode), 1984 (non-dipole wet mode), and 1998 (non-dipole dry mode) with respect to the whole simulation period. Due to the underrepresentation of Sahelian precipitation by the model (see Chapter 6.3), the simulated rain belt during wet years tends to start slightly more south as the observed one [compared to: Nicholson and Webster, 2007]. Furthermore, Fig. 6.6 illustrates, that the differences of the simulated annual amount of precipitation in the region of approx. 8°N – 22°N are governed by the rainfall in JJAS.

The simulated anomalies in δD_P with respect to mean δD_P within 1958–2002 are displayed in Fig. 6.7, (left) as mean over JJAS and (right) as the annual mean. Most notably, Fig. 6.7e – 6.7h, representing the years with non-dipole rainfall anomaly pattern, clearly illustrate the negative relation between δD_P and amount of precipitation, while Fig. 6.7a – 6.7d, representing the years with dipole rainfall anomaly pattern, depict positive and negative anomalies in δD_P. This is most likely caused by the history of the precipitated water. Cadet and Nnoli [1987] have demonstrated that the Gulf of Guinea is one source of moisture feeding the North-West African summer monsoon. Furthermore, they have pointed out the importance of evapotranspiration over the Guinean coast region, where the water vapor is recycled before it gets transported further north. Due to this dynamics in years with a more dipole wet Sahel configuration the relative enriched water vapor which would, under 'normal conditions' rain out over Guinea could travel further north and possibly causes local positive anomalies in δD_P. In contrast, dipole years with a

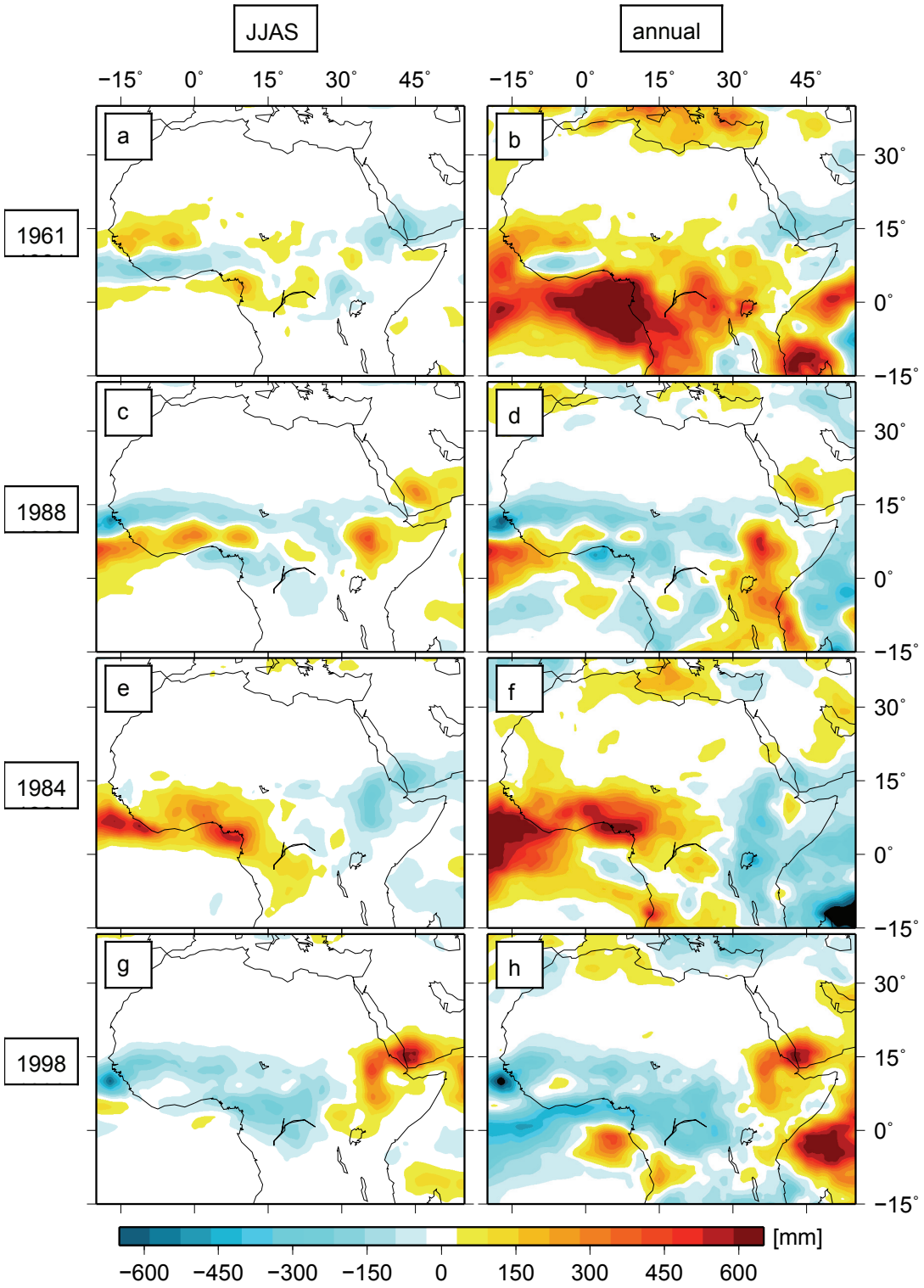

Figure 6.6.: North African spatial distribution of the precipitation anomalies for the years 1961 (dipole wet Sahel mode), 1988 (dipole dry Sahel mode), 1984 (non-dipole wet mode), 1998 (non-dipole dry mode) with respect to the mean precipitation over the period 1958–2002. The anomaly over the rainy season (left) and the annual anomaly (right).

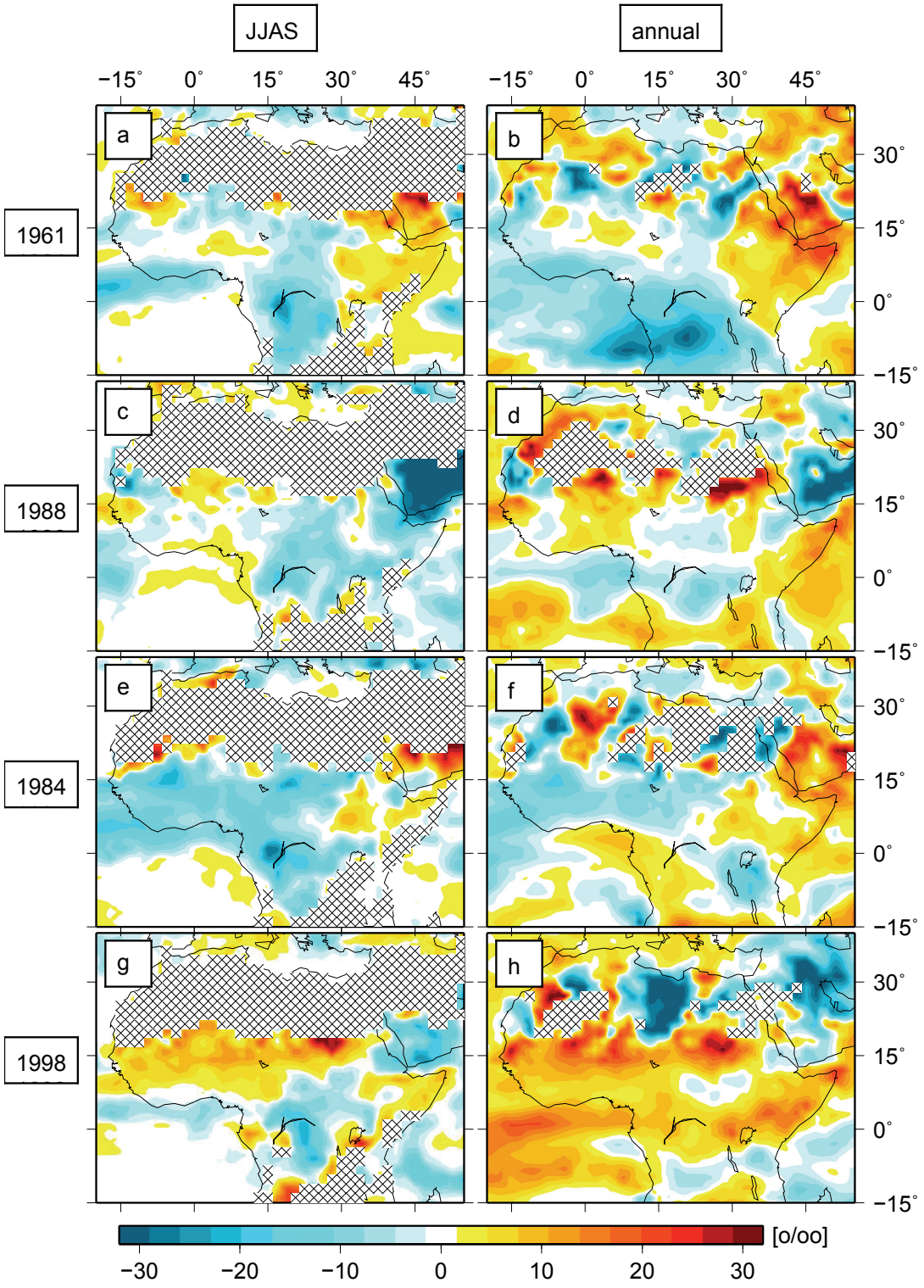

Figure 6.7.: Same as Fig 6.6 but for δD_P. The hatched areas in the figures mark those grid boxes where the simulated precipitation is less then 1 mm/month.

more dry Sahel mode providing stronger precipitation at the Guinean coast, which most likely results in a relative depletion of the moisture traveling northwards. Years with a non-dipole mode, however, provide more or less precipitation over the whole monsoon region. Consequently the anomalies in δD_P show a more uniform pattern over whole North-West Africa.

6.5 ANALYSIS OF THE SIMULATED TIME SERIES

6.5.1 *Evolution of the Sahel precipitation*

Figure 6.8 shows the comparison of the simulated and reconstructed annual precipitation in the West Sahel over the simulated period as absolute values and as a calculated rainfall index[2]. Similar to the underestimation of precipitation amount at Bamako, Niamey, and N'Djamena (Chapter 6.4), the model underestimates as well the Sahelian amount of precipitation. Moreover, while the CRU observational data set depicts the Sahel drought, with relatively more precipitation during the early 60's and drier conditions during the 70's and 80's, the simulated data does not indicate a longer drought period at all.

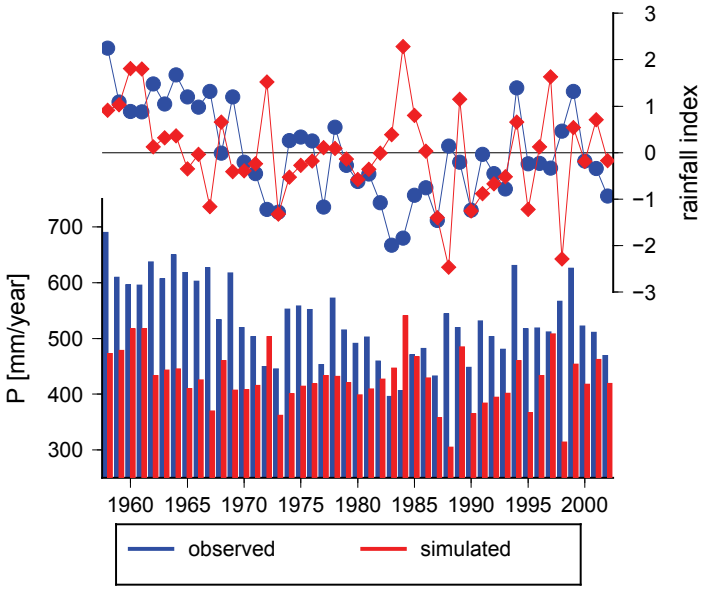

Figure 6.8.: Comparison of the simulated and observed [Harris et al., 2014] annual precipitation in the West Sahel from 1958–2002 as rainfall index (upper panel) and amount in per year (lower panel).

2 The rainfall index (RI) is calculated as deviation of the mean annual precipitation ($\bar{P}$, calculated over the time 1958–2002), normalized by the standard deviation: $RI_i = \frac{P_i - \bar{P}}{\sqrt{\frac{1}{44}\sum_{j=1}^{45}(P_j - \bar{P})^2}}$, with $i \in \{1958, 1959, ..., 2002\}$.

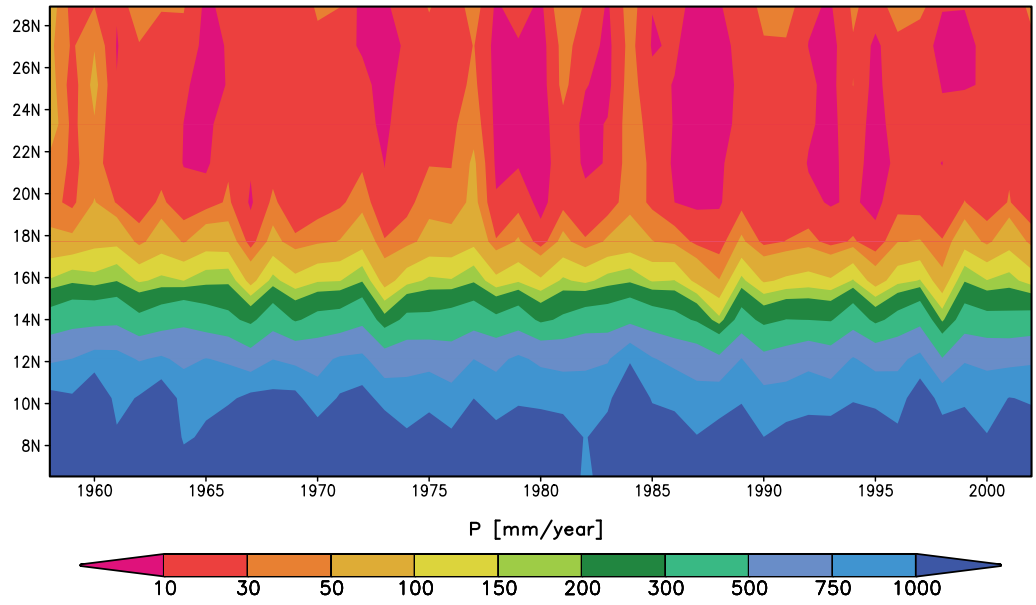

Figure 6.9.: Hovmoeller type diagram of simulated precipitation over the period 1958–2002 of zonal mean (averaged over land-area from 20°W–10°E) annual precipitation of North Africa.

In order to exclude the possibility that the Sahel drought is simulated with a spatial shift, the annual amount of precipitation is analyzed as a Hovmoeller type diagram, zonally averaged over 20°W–10°E, over the simulation period (Fig. 6.9). No drought period, but only a very slight southwards expansion of the drier conditions can be detected between 15°N and 20°N. This result is reflected by corresponding evolution of the isotopic composition of precipitation (Fig. 6.10). The simulated δD_P data show relative depleted values around 1960 implying wetter conditions, but again no sign for the Sahel drought is found in the simulated precipitation weighted δD_P.

The ECHAM-JSBACH-wiso experiment has been nudged to the re-analysis ERA40 data set, and as further boundary conditions annual mean values of present-day greenhouse gases as well as reconstructed annual land use vegetation maps have been used. Thus, it is unexpected, that the simulation results are inconsistent in such a degree with the observational data. A possible reason for this deficit of the model simulation could be the forcing data for the nudged experiment. Di Giuseppe et al. [2013] have shown, that the ERA-I climate is unrealistically wet at the Sahel in the 70's–80's, while at later periods it predicts more realistic values. Another explanation for this mismatch between observational and simulated data might be the absence of incorporated aerosols or dust in the ECHAM5-JSBACH-wiso model. The feedback mechanisms between Sahelian precipitation and atmospheric aerosols are not fully understood yet, but studies [e. g., Nicholson, 2000; Haywood et al., 2013] have proposed that including dust mobilization is needed

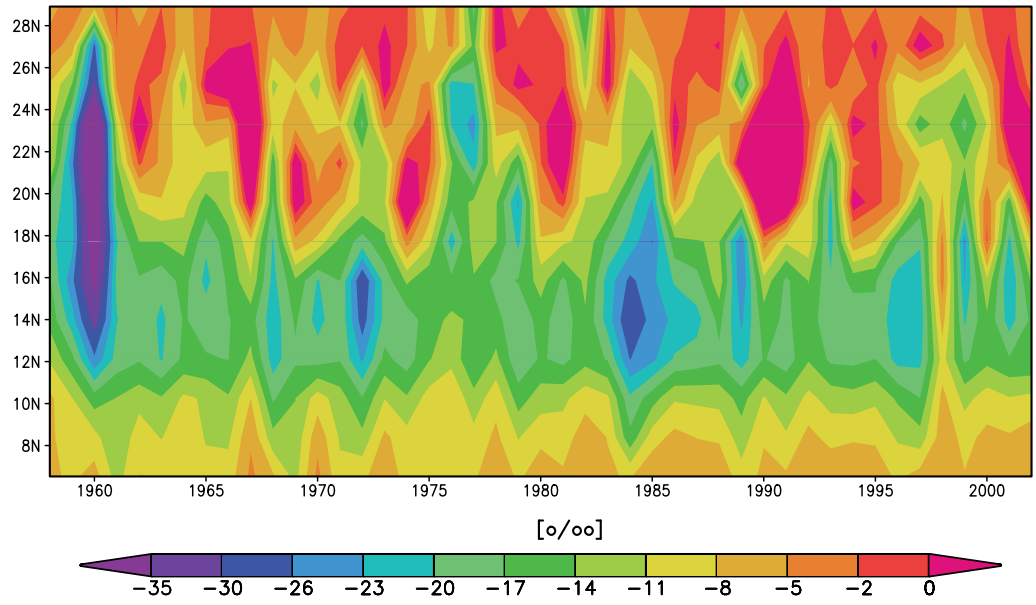

Figure 6.10.: Same as 6.9, but for precipitation weighted δD_P.

to simulate a realistic climate over the Sahel. Finally, the underestimation of convective precipitation [Hagemann et al., 2006; Dallmeyer, 2008, discussed in Chapter 6.3] may also be a reason for the absence of the particularly wet years during the 60's. It remains a question, if the model results may improve by incorporating one or all aspects into the simulation setup.

6.5.2 *Comparison between the model simulation and proxy data*

In order to further evaluate the simulated time series, the δD_P is compared to the compound-specific hydrogen isotope values of land plant waxes derived from long-chain *n*-alkanes of sediment core GeoB9501 [Beckmann et al., 2013]. The core's catchment area is situated between 18°W–8°W and 12°N–30°N. As illustrated in Fig. 6.11, both the calculated index of precipitation amount and the isotopic composition of precipitation in the core catchment area are linearly related to the corresponding values in the West Sahel. The annual amount of rainfall in these two areas is correlated after Pearson with the coefficient $r = 0.89$ for the observational data and $r = 0.69$ for the simulation. For the simulated δD_P the correlation coefficient is $r = 0.84$.

The comparison of the simulated δD_P, from 1958–2002, and the measured δD signal [Beckmann et al., 2013] is shown in Fig. 6.12. Since the δD signal in the *n*-C_{31} alkane is measured approximately every 5 years, for the model-data comparison a 5-year running

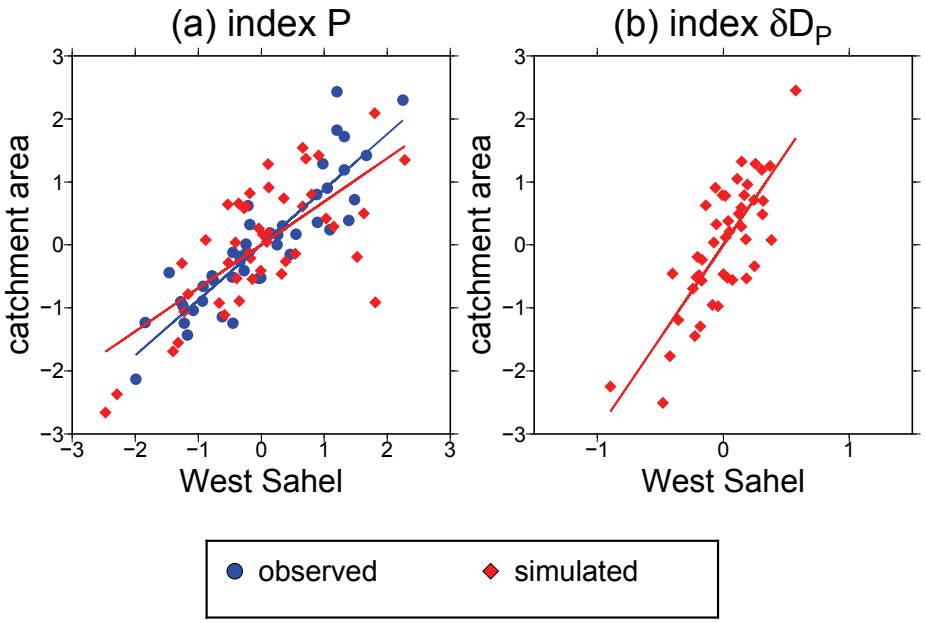

Figure 6.11.: Comparison of the calculated indices for amount of precipitation (left) and its isotopic composition (right) for the West Sahel and the catchment area.

mean is calculated for the model simulation and shown for all years in which measurements are available (Fig. 6.12, red).

Comparing the simulated δD_P and the measured δD of the *n*-C_{31} alkane, one can see that the variations in δD of the proxy are with approx. 10‰ (Fig. 6.12b) twice as high as for the calculated 5-years running mean of the simulation with 5‰ (Fig. 6.12a). The calculated index[3] of the δD variations from GeoB9501 (Fig. 6.12c, green) depicts more enriched isotope values compared to the average for nearly all measurements between 1970 and 1994. This is most likely a result of the negative relation between precipitation amount and δD_P and might indicate the dry conditions during the Sahel drought. The simulated index of δD_P (Fig. 6.12a, red) matches surprisingly well with the index of the proxy data. Between 1958 and 1980 both signals are nearly identical. Strikingly is the negative index value simulated in 1985, which highly overestimates the depletion of δD compared to the proxy data. In the 1990s the simulated index, calculated from the 5-year running mean of δD_P, reveals only slight variations, while the index of the proxy data shows high variations. This could be caused by the decreased integration time of the proxy signal during the 1990s. The influence of integration time on the results can also be seen for the simulation, if the simulated 5-year running mean (red) is compared to the annual values (gray) in Fig. 6.12c.

3 The index is calculated in an identical manner as the rainfall index described on page 71.

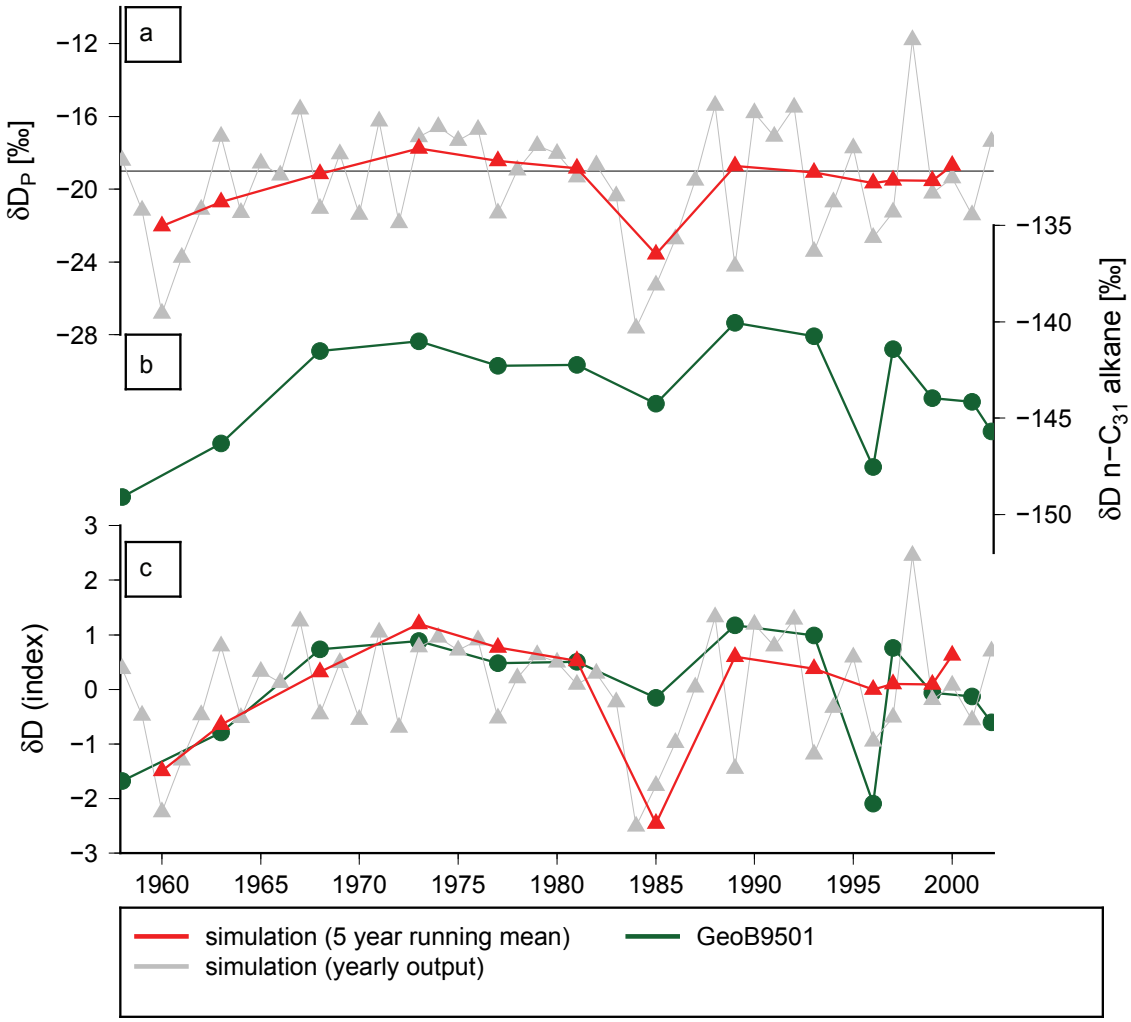

Figure 6.12.: (a) Simulated δD_P as 5 year running mean (red) and yearly data (gray). (b) Measured δD n-C_{31} alkane (green). (c) Index of the variations in δD of the simulated δD_P (red/gray), and the measured δD n-C_{31} alkane (green).

6.6 QUANTIFICATION OF THE RELATION BETWEEN RAINFALL AMOUNT AND DEUTERIUM

For the area of interest, two main different rainfall anomaly patterns, a dipole and a non-dipole pattern, have been described. In Chapter 6.4.2 it is shown that these patterns have a strong influence on the distribution of δD_P over North-West Africa. However, the question arises how these patterns affect the interpretation of the δD signal in proxy data. The relation between the simulated precipitation and its isotopic composition is illustrated in Fig. 6.13. The simulated δD_P in the West Sahel is, with a Pearson corre-

lation coefficient of $r = -0.71$ (calculated over the whole simulation period), linearly dependent on the amount of the Sahel precipitation.

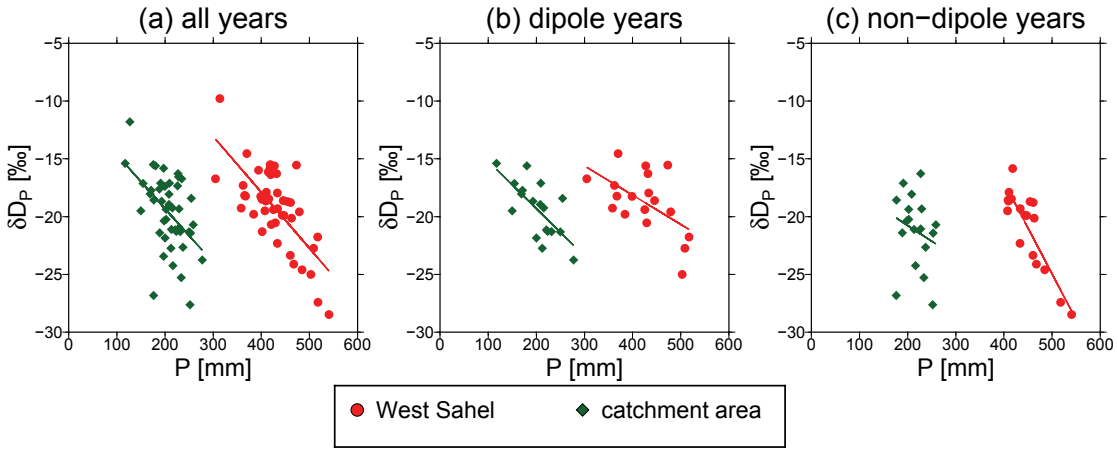

Figure 6.13.: Simulated relation between P and δD_P for the West Sahel (red) and the catchment area from GeoB9501 (green): (a) for all simulation years, (b) for years with a dipole rainfall anomaly pattern, and (c) for years with a non-dipole rainfall anomaly pattern.

By distinguishing between the anomaly patterns, it is found that in the more dipole like years the linear relation between precipitation amount in the Sahel and its δD_P is weaker ($r = -0.56$) than in the non-dipole years ($r = -0.84$). Thus, years with a more non-dipole like pattern anomaly tend to have stronger variations in the isotopic composition in the West Sahel (see Appendix B, Tab. B.1). For the core catchment area the correlation between P and δD_P calculated over the whole simulation period is weaker than in the West Sahel ($r = -0.49$). Furthermore, while the correlation for all years and non-dipole years ($r = -0.47$) have a similar magnitude of strength, the correlation for years with a dipole anomaly is stronger ($r = -0.70$).

Based on the calculated linear relations between the simulated precipitation amount P and δD_P (see Fig. 6.13), the amount of precipitation can be estimated from the simulated δD_P by a linear regression. For the West Sahel the coefficient of determination (R^2)[4] is $R^2 = 0.51$. Thus, 51% of the variation of precipitation amount can be explained by the linear regression $P(\delta D_P)$ (Fig. 6.14a). The calculated R^2 is independent of the rainfall anomaly pattern. In contrast, for the catchment area only 24% of the variation of the simulated amount of precipitation can be explained by the linear regression $P(\delta D_P)$ (Fig. 6.14b). A possible reason of this weak relation in the catchment area may be that summer precipitation is highly underestimated by the model, hence the rainfall amount is most likely too less for a quantitative calibration of $P(\delta D_P)$.

4 The statistical value R^2 describes the quality of the linear regression. It explains, which percentage of the variation in a variable can be explained by the linear regression.

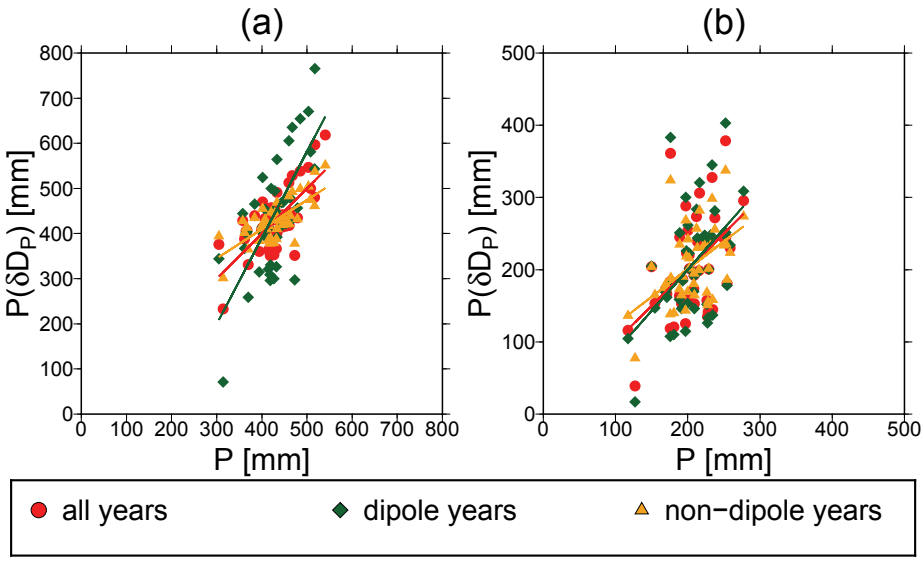

Figure 6.14.: Comparison of the simulated precipitation (P) and the calculated one ($P(\delta D_P)$) for (a) the West Sahel and (b) the catchment area from GeoB9508.

In order to quantify the changes in rainfall amount with respect to the proxy signal, the precipitation anomaly is estimated using the linear regression for the measured anomaly in δD of n-C_{31} alkane retrieved from GeoB9501. Since the linear relation calculated for the catchment area is very weak, the transfer function calculated for the West Sahel over all years is used for this estimation:

$$P(\delta D) = \frac{\delta D}{-0.4847} \tag{6.1}$$

The resulting estimated precipitation anomalies compared to the observed rainfall anomalies are illustrated in Fig. 6.15. Albeit the variations of the estimated $P(\delta D)$ are stronger than in the observed values, the trend is in a good agreement with the observed one. The overestimation of the amplitude in the estimated $P(\delta D)$ are most likely linked to the fact that the transfer function is calculated for the West Sahel where more precipitation occurs than in the core catchment area. Otherwise, the error caused by using the West Sahel linear regression may be negligible compared to the error caused by the linear regression method itself.

6.7 SUMMARY AND INFERENCES

In this chapter it is shown that the model simulates the characteristics of the North African climate compared to observed data, with respect to temperature, precipitation as well as its δD_P values, and wind fields, fairly well. Most important is the under-

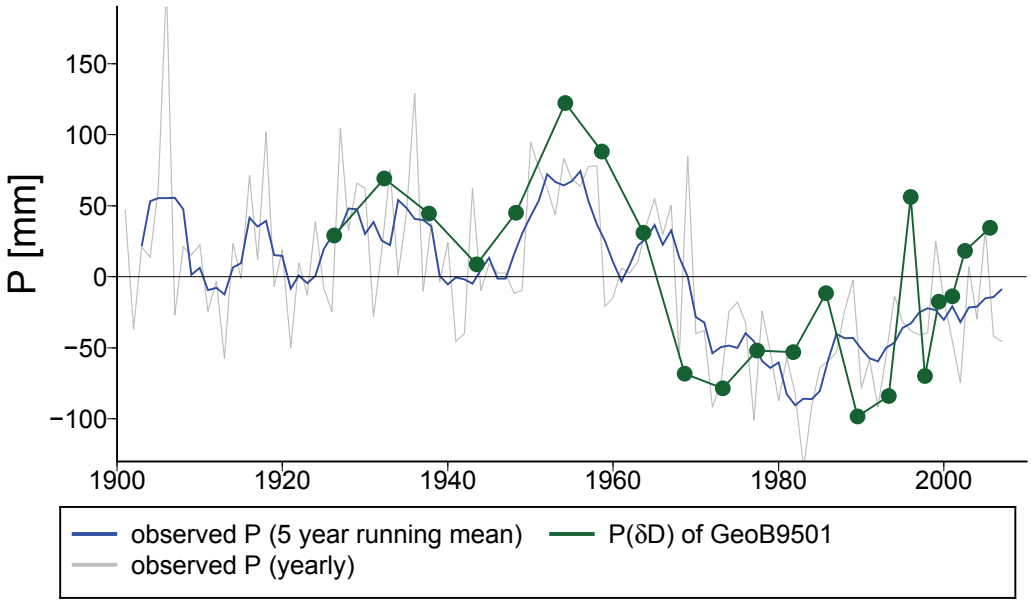

Figure 6.15.: Observed rainfall anomaly of the 20th century as 5-years running mean (blue) and as yearly values (gray). The estimated anomaly in $P(\delta D)$ of the measured anomaly of δD in n-C_{31} alkanes (green)

estimation of the monsoon rainfall from the ECHAM5-JSBACH-wiso model, which agrees with the findings of Dallmeyer [2008]. The simulated isotopic composition of the North African precipitation is linearly dependent on the amount of precipitation. Under present-day conditions the δD_P in the West Sahel is dominated by the signal of the JJAS season. The simulated δD_P as well as its interannual variability are in good agreement with observed values from the three GNIP stations.

As illustrated in Chapter 6.5.1, even with the ERA40 nudged model experiment and prescribed changes in vegetation cover, it has been impossible to simulate the Sahel drought with the ECHAM5-JSBACH-wiso model. The mismatch might be explained by the findings of Di Giuseppe et al. [2013] showing that the ERA-I climate predicts too wet conditions at the Sahel between the 1970s and 1980s. It remains open if the simulation were more realistic if nudged with a corrected re-analysis data set, as proposed by Di Giuseppe et al. [2013]. Another possible reason for the absence of the shift of the amount of rainfall could be the underestimation of convective precipitation [Hagemann et al., 2006; Dallmeyer, 2008]. Furthermore, the feedback mechanisms between atmospheric dust or aerosols and the atmosphere, which are yet not fully understood, are not taken into account within the model. Yet, studies like Nicholson [2000] or Haywood et al. [2013] have shown that dust and aerosols have a considerable impact on the North-West African monsoon system.

Finally, the simulated relation between the annual amount of precipitation and the corresponding δD_P values has been quantified for present-day conditions. Based on the linear dependency of P and δD_P in the West Sahel, it is calculated that an increase of δD_P of 5‰ is related to a decrease in precipitation of approx. 100 mm. Most likely caused by the underestimation of amount of precipitation by the ECHAM5-JSBACH-wiso model simulation, it was not possible to calculate such a quantification for the catchment area of the sediment core GeoB9501. The computed quality of the linear regression for the catchment area of $R^2 = 0.24$ is less than half as the value of West Sahel ($R^2 = 0.51$). However, using the $P - \delta D_P$ relationship calculated for the West Sahel to estimate the variations in rainfall amount indicated by the δD in *n*-C_{31} alkanes measured in GeoB9501, results in a precipitation time series which is in a fairly well agreement with the observations.

7

THE AFRICAN HYDROLOGICAL CYCLE DURING THE HOLOCENE

The determining factors for changes in the amplitude of the seasonality of solar radiation are variations of the orbital parameters [Berger, 1978]. Changes in precession, which describe the orientation of the Earth's rotational axis, induce variations of incoming solar radiation. Owing to the diversity in precession, the seasonal cycle during the early- and mid-Holocene was amplified, with stronger summer and weaker winter insolation in the northern hemisphere [Ruddiman, 2008; Chapter 3.3.2]. Due to these changes in boreal summer insolation, the North-West African monsoon system was much stronger than today. Therefore the North African climate was more humid and the area was more vegetated. Evidence for these conditions is given for instance by analysis of marine sediments [e. g., deMenocal et al., 2000; Dupont, 2011], lake sediments [e. g., Kröpelin et al., 2008], or rock engravings [e. g., McIntosh and McIntosh, 1983]. Model studies discuss various feedback mechanisms, for example between the atmosphere and the sea surface temperature (SST) [e. g., Kutzbach and Liu, 1997] or interactions between atmosphere and land surface [e. g., Claussen and Gayler, 1997; Kutzbach et al., 1996]. Others, as e. g., Krinner et al. [2012], have shown that higher lake levels and increased area of wetlands lead to enhanced evapotranspiration, or have discussed that an increase in surface albedo leads to a decrease in precipitation [e. g., Vamborg et al., 2011].

It is still a dispute whether the transition from the more humid, vegetated conditions in North-West Africa during mid-Holocene towards the dry present-day (PD) conditions were gradual or abrupt. DeMenocal et al. [2000] for instance have examined an abrupt increase of terrigenous material in a marine sediment core located on the north-west coast of Africa, which has been interpreted as an abrupt end of the African Humid Period, while pollen reconstructions from lake Yoa published by Kröpelin et al. [2008] have suggested a more gradual change in vegetation cover. Both theories have been backed up by model studies. While e. g., Claussen et al. [1999] or Liu et al. [2007] were supporting the theory of an abrupt change in environment, other studies, e. g., Braconnot et al. [2007a]; [2007b] were corroborating the assumption that the transition to the arid conditions was more gradual.

This chapter focuses on this question, whether the transition from the humid mid-Holocene conditions into the dry conditions today in North-West Africa has been more gradual or more abrupt. For this purpose, model simulations and proxy data are used.

In order to analyze the long-term evolution from mid-Holocene to PD, a transient model experiment, performed with the fully coupled Earth system model COSMOS, is used. Based on this transient experiment, time-slice experiments have been carried out with the coupled atmosphere-land surface model ECHAM5-JSBACH-wiso, which allows the explicit simulation of the stable water isotopes $H_2^{16}O$, $H_2^{18}O$, and HDO. This isotope model offers the possibility to directly compare the simulated δD signal with the measured one from proxy data. Here, the recently reconstructed deuterium signal of precipitation (δD_P) of sediment core GeoB7920 [B. Beckmann, personal communication], located in the coastal area of North-West Africa, is used for comparison with the simulated δD_P values.

7.1 EXPERIMENTAL SETUP OF THE HOLOCENE SIMULATIONS

7.1.1 *Transient experiment*

The evolution of precipitation in northern Africa is analyzed in a 6,000 year transient model simulation (called T6000) performed by Fischer and Jungclaus [2011] over the period from 6,000 before present (BP) to present. This experiment was set up with the fully coupled Earth system model COSMOS (ECHAM5-MPI-OM-JSBACH, see Chapter 4.1). The atmosphere-land surface component was executed with a resolution of approx. 3.75° and 19 vertical levels (T31L19) and the ocean component was executed with a resolution of approx. 3° and 40 vertical levels (GR30). Fischer and Jungclaus [2011] have applied a yearly orbital forcing described by Bretagnon and Francou [1988]. The greenhouse gas concentration was set to pre-industrial conditions (CO_2=280ppm, CH_4=700ppb, N_2O=265ppb). A more detailed description is given by Fischer and Jungclaus [2011].

7.1.2 *Time-slice simulations*

In addition to the analysis of the transient experiment, four time-slice experiments are performed: for pre-industrial conditions (PI, the experiment is called H0k), for 2,000 years BP (called H2k), for 4,000 years BP (called H4k), and for 6,000 years BP (called H6k). All four experiments are done with the ECHAM5-JSBACH-wiso model with the model resolution T63L31, using the noF setup, which means no fractionation processes during evapotranspiration are included (described in detail in Chapter 4.3). An integration time of 30 years after a spin-up of 2 years is analyzed. The orbital parameters for each time-slice experiment are calculated with a method developed by Berger [1978]. For

the lower boundary conditions of the stable water isotopes the same present-day data set as described in Chapter 5.1 is used. The vegetation cover, SST, and sea ice cover (SIC) is based on the output data of the transient model experiment T6000. Therefore a 30 years climatology from the T6000 experiment for the four time-slices is calculated. The output fields are interpolated from the horizontal resolution T31 to T63.

7.2 EVOLUTION OF THE NORTH-WEST AFRICAN HYDROLOGY

7.2.1 *Results of the transient Holocene experiment*

Fischer and Jungclaus [2011] discussed the response of the global temperature field with respect to the change of orbital parameters. They have found that in high latitudes the sea-ice insolation effect outweighs the insolation effect, while the seasonal insolation distribution defines the amplitude of the seasonal cycle in the low and mid latitudes. One of the strongest decreases of the amplitude of the seasonal temperature cycle, according to the decrease of the amplitude of the seasonal insolation cycle, has been detected over North Africa, via the northern part of the Arabian Peninsula, to central Asia.

In this study the focus is on the evolution of the hydrology of North Africa. In this context, Fischer and Jungclaus [2011] have shown that the insolation changes were accompanied by a southward migration of the Intertropical Convergence Zone (ITCZ). Furthermore, they have demonstrated that these changes conduct a decrease of cloud cover and the weakening of the North-West African summer monsoon from mid-Holocene to PD.

Figure 7.1 displays the zonally averaged (20°W to 55°E) 30 years running mean for the annual mean precipitation of North Africa in a Hovmoeller-type diagram. It shows a decrease of the simulated precipitation from approx. 5,500 BP to 1,500 BP in the area from approx. 5°N to 30°N. Furthermore, Fig. 7.1 indicates an expansion of the dry areas with annual mean precipitation of less than 2mm/month. The modeled zonal transition from the humid conditions during the mid-Holocene to the drier present-day conditions of North Africa is rather gradual.

Due to the simulated evolution of precipitation the corresponding vegetation cover is reduced as well (Fig. 7.2). The simulated changes of desert fraction between 10°N and 30°N are caused by a transition from cover fraction dominated by shrubs, via cover fraction dominated by grasses, into bare soil. The change to more desert fraction is mainly gradual and the gradients of reduction over the time are nearly equal, with two exceptions: Firstly, a relatively fast transition from 0.8 to 0.9 or more fraction of desert between 23°N to 30°N is taking place from 5,200 BP to 3,000 BP. Since this transition

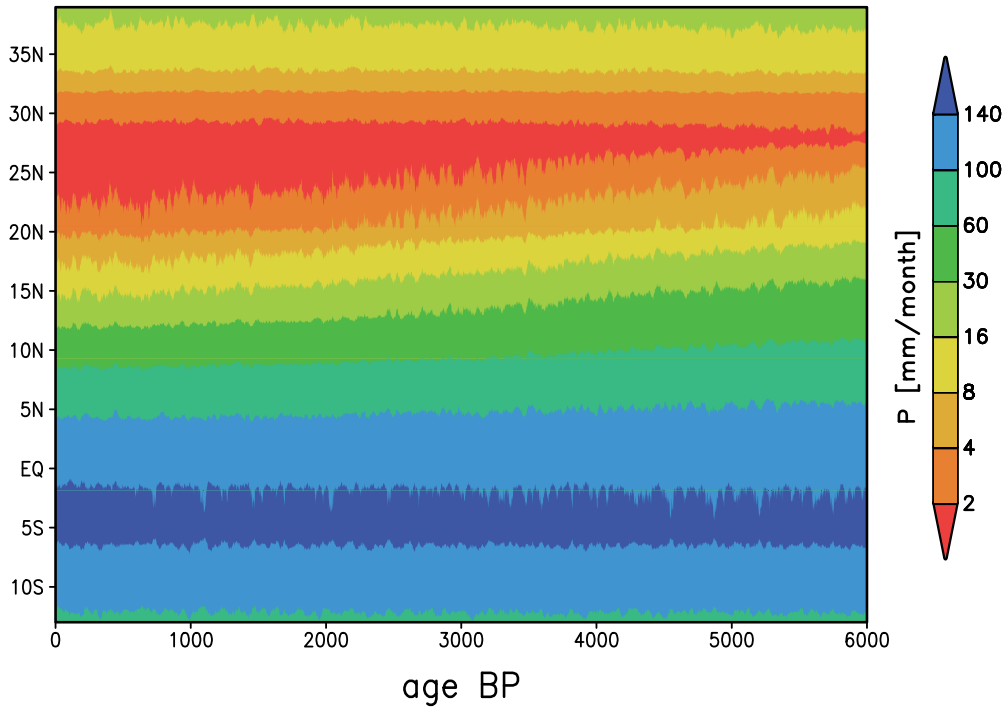

Figure 7.1.: Hovmoeller type diagram of running mean (30 years) of zonal annual mean precipitation of North Africa (20°W to 55°E) of the transient T6000 experiment.

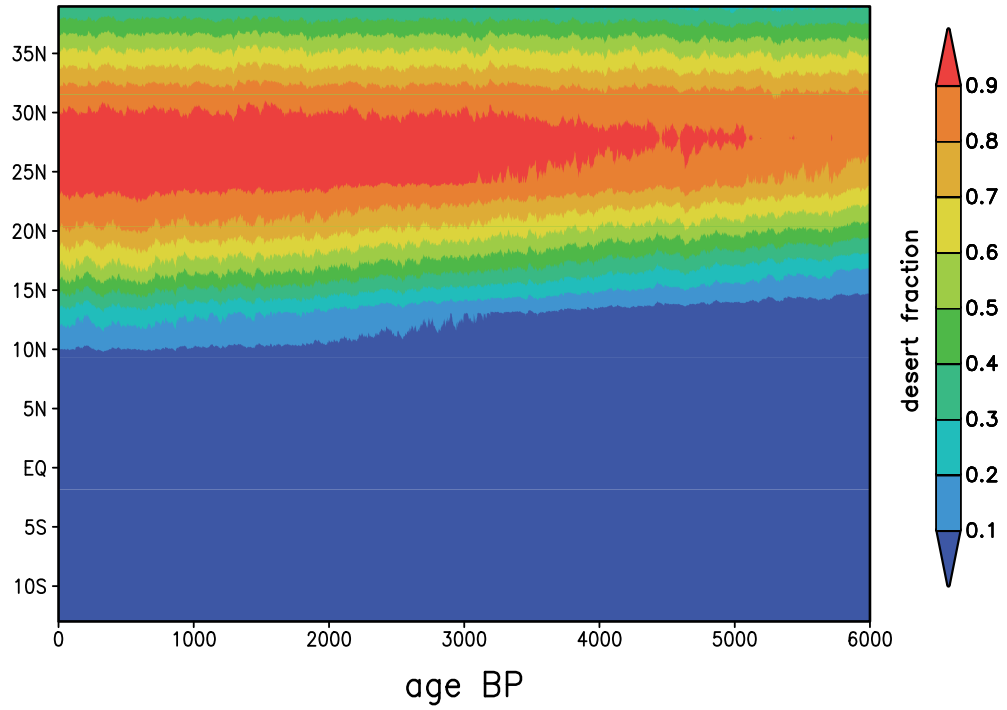

Figure 7.2.: Hovmoeller type diagram of zonal mean desert fraction of North Africa (20°W to 55°E) of the transient T6000 experiment.

is caused by reduction of mainly grass and partly shrubs (not shown), the variations of the amplitude during the transition are also relatively high. Secondly, in the area 10°N to 13°N occurs also a shift in vegetation cover from 3,000 BP to 2,000 BP, which has a relative stronger gradient compared to the other transitions. Here the fraction of desert changed from 10% or less to 20%.

In order to analyze the desertification of North Africa in more detail Fig. 7.3 shows the anomaly of the two time-slices H6k-H0k for shrubs (7.3a) and desert (7.3b). A strong decrease, with a reduction of up to 60%, of the shrubs cover fraction is simulated over the whole Sahel and the Arabian Peninsula. The simulated desertification has a similar pattern, with an averaged increase of the desert fraction of 40% in the area between approx. 14°N to 25°N. In order to show the regional temporal transitions, three test sites were selected:

- Area 1, which presents an arid region of North-West Sahel and South-West Sahara (18°W to 0°E and 15°N to 31°N), was chosen because it is the region of the catchment area of sediment core GeoB7920.
- Area 2 (25°E to 35°E and 15°N to 25°N), represents an area with a relative high fraction of desertification, with approx. 50% change, from 6,000 BP to PD in the East Sahel region.
- Area 3 (5°W to 10°E and 10°N to 18°N) is chosen because it represents a region of the South-West Sahel where the decrease of the shrubs fraction between 6,000 BP and PD is relative high (approx. 50–60%).

For all three simulation areas, the evolution of desert fraction and vegetation cover reveals a rather gradual transition (Fig. 7.3c).

7.2.2 *Results of the time-slice experiments*

The analysis of the time-slice experiments focuses on the North-West African rain period, which is from June to September (JJAS) and provides most of the annual precipitation (see also Chapter 3). Figure 7.4a-7.4c show the simulated PI mean for (a) temperature and wind on the 850hPa level, (b) precipitation, and (c) the δD in precipitation (δD_P). A positive temperature gradient from the Atlantic ocean to the east of the Saharan desert is depicted in Fig. 7.4a. The North-West African monsoon wind is caused by this temperature difference and follows the strongest gradient. In contrast, north of 15°N, the strong Harmattan wind is dominating. The simulated rain belt (cf. Chapter 3.1), sustained by the moist monsoon wind is shown in Fig. 7.4b. It is located between approx. 10°S and

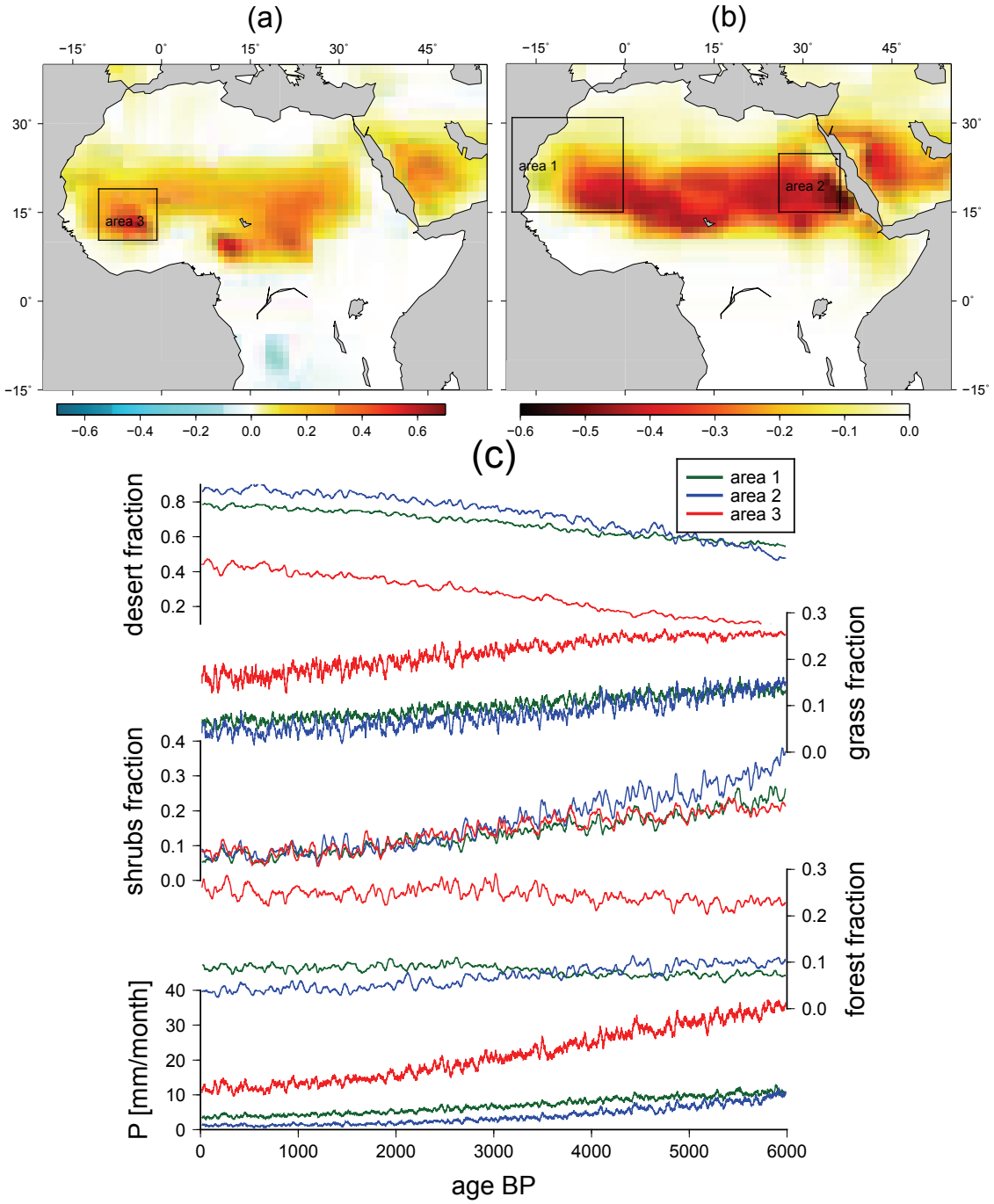

Figure 7.3.: Simulated anomaly H6k-H0k of (a) shrubs and (b) desert. (c) shows the simulated evolution of the 30 year running mean of precipitation, forest, shrubs, grass, and desert over the area 1 between 18°W–0°E and 15°N–31°N (green), area 2 between 25°E–35°E and 15°N–25°N (blue), and area 3 between 5°W–15°W and 10°N–18°N (red). The boxes in Figure (a) and (b) mark area 1, area 2, and area 3.

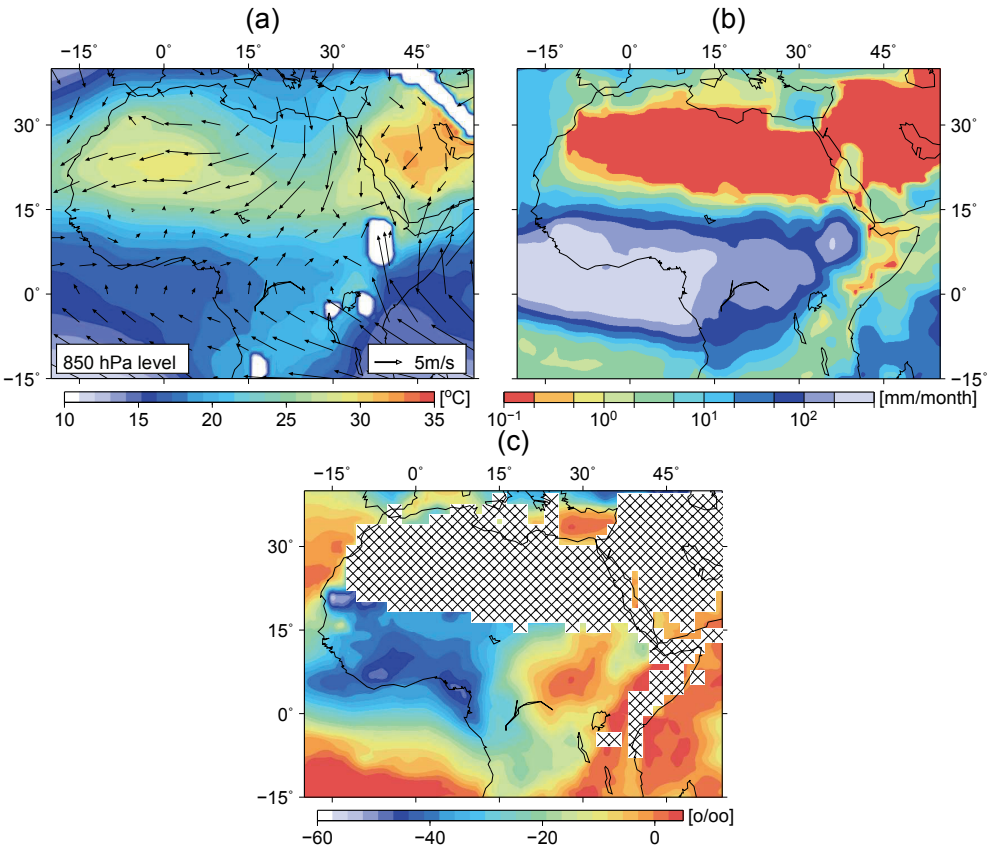

Figure 7.4.: Simulated pre-industrial mean over the JJAS season of (a) temperature and wind on 850hPa, (b) precipitation, and (c) δD_P. The hatched area marks regions where the mean precipitation of JJAS is less then 1mm/month.

15°N with its maximum at approx. 7°N which is 3° more south than observed for PD [Sultan and Janicot, 2003]. The simulated composition of deuterium in precipitation δD_P is shown in Fig. 7.4c. While the North-West African precipitation is relatively depleted in deuterium in precipitation, the East African precipitation is more enriched. This is in accordance with the results of Chapter 6.3, as well as Chapter 5.4.2 and Chapter 5.5.2. The simulated annual mean δD_P (not shown) has the same pattern, which agrees with the findings of Rozanski et al. [1993].

The anomalies of H2k, H4k, and H6k with respect to H0k are shown for temperature and wind (850hPa level) in Fig. 7.5. The temperature anomaly of H6k – H0k (Fig. 7.5c) shows an increase as well as a northwards shift of the temperature gradient at 6ka BP with respect to pre-industrial conditions. Thus the monsoon is strengthened and shifts northwards, while the Harmattan weakens. The cooling between approx. 0°N and 20°N can be linked to the increased cloud cover at the H6k experiment compared to the H0k one [see also Fischer and Jungclaus, 2011]. Due to the decrease of boreal summer insolation the simulated temperature as well as the near surface wind anomaly are

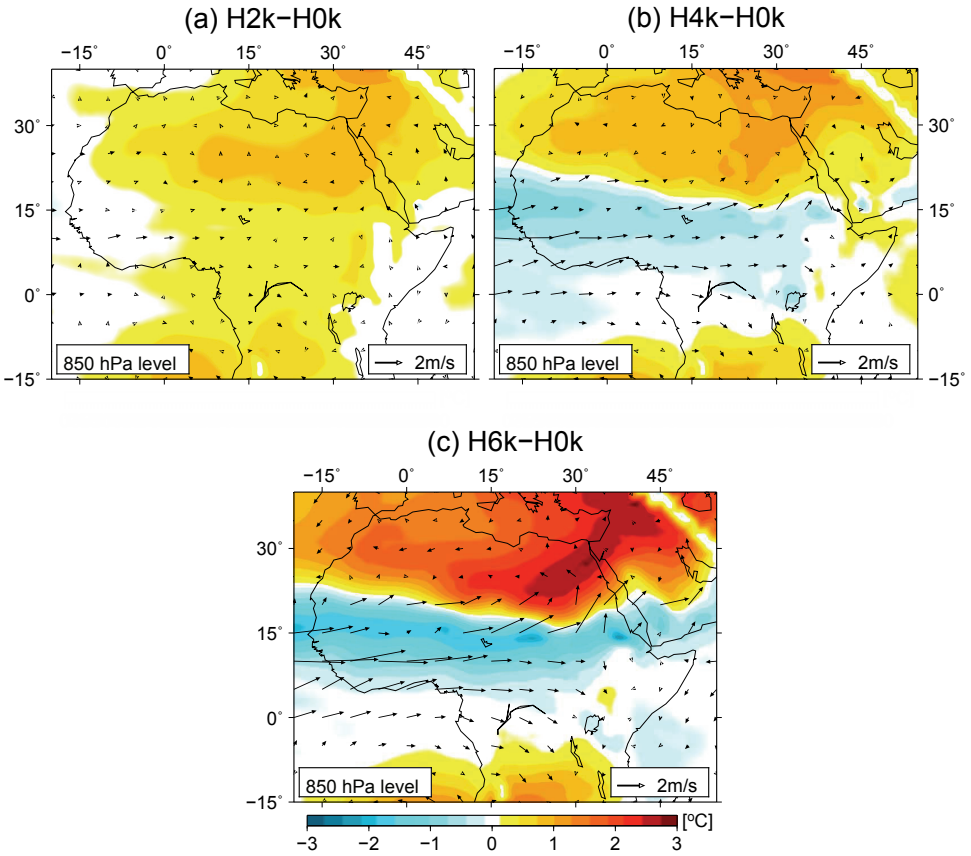

Figure 7.5.: Simulated anomalies of the surface temperature (color-map) and of the winds on the 850hPa level (arrows) over the rainy season (JJAS) for the H2k, H4k, and H6k simulation with respect to the pre-industrial simulation Hk0.

weaker for H4k − H0k as for H6k − H0k (Fig. 7.5b). The anomaly of H2k with respect to H0k shows only a slight warming due to the slightly higher boreal summer insolation. Furthermore, in contrast to the H4k and H6k experiment the simulated cloud cover is nearly the same as in the H0k simulation (not shown).

Figure 7.6 shows the simulated mean zonal wind for JJAS for 10°W-10°E at PI (a), 2ka BP (b), 4ka BP (c), and 6ka BP (d). At 6ka BP (Fig. 7.6d) the simulation shows a northwards shift of the African Easterly Jet (AEJ), Intertropical Discontinuity (ITD), and the ITCZ compared to PI. Moreover, while the monsoon as well as the Tropical Easterly Jet (TEJ) are stronger at 6ka BP compared to PI, the Harmattan and the AEJ are weaker. Taken as a whole, the simulation H6k show all characteristics of the PD configuration for wet years (compare with Chapter 3.3). The simulation of 4ka BP (Fig. 7.6c) reveals a similar pattern as the 6ka BP simulation, but with a weaker anomaly as compared to pre-industrial climate. For the H2k experiment the simulated anomaly of the wind system is reduced as well, therefore the experiment has a very similar wind pattern as

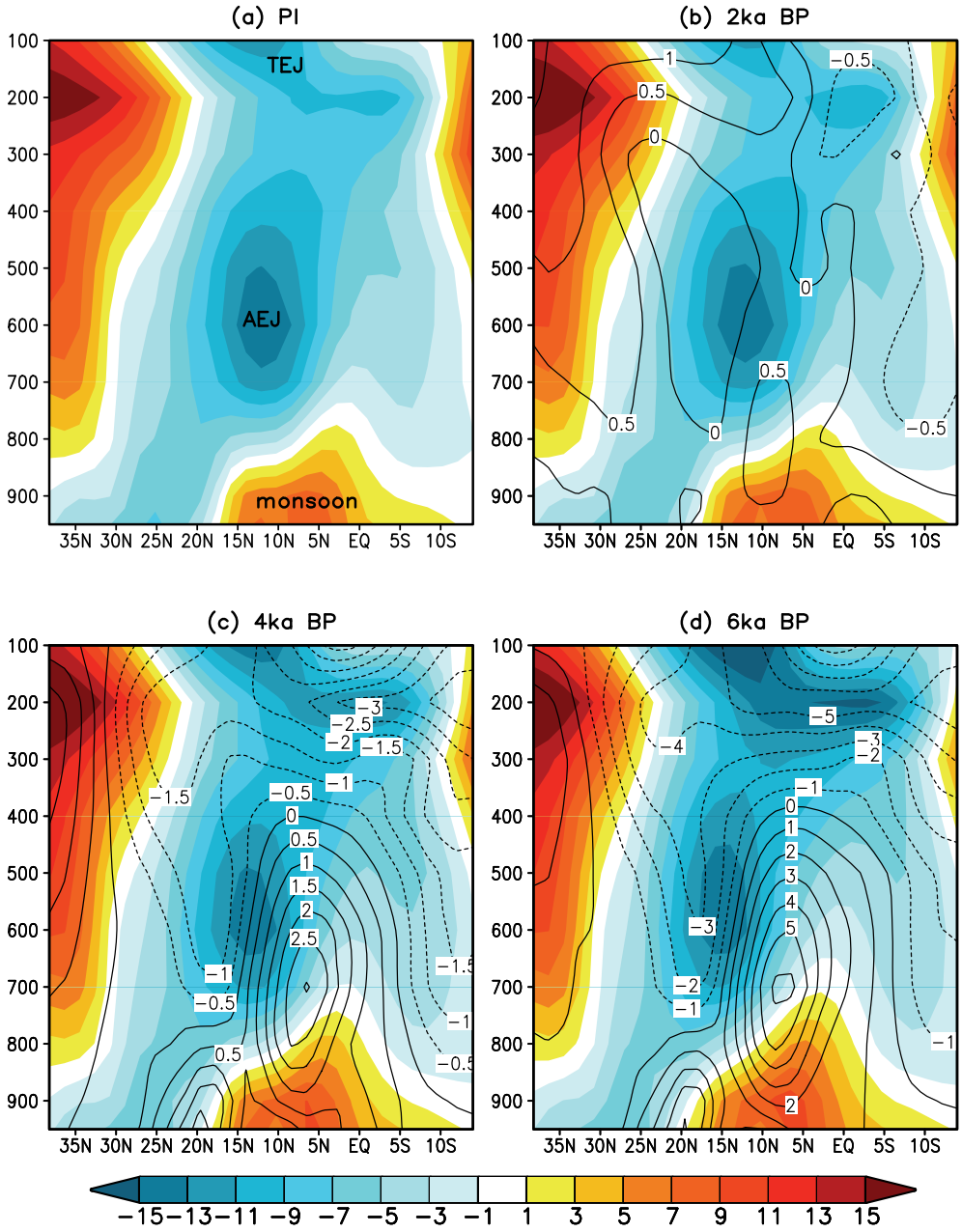

Figure 7.6.: Simulated zonal-seasonal (10°W-10°E, JJAS) wind [m/s] over pressure [hPa] for pre-industrial conditions (a), 2ka BP (b), 4ka BP (c), and 6ka BP (d). The absolute wind speed is pictured in colors and the anomalies of the Holocene simulations with respect to the pre-industrial simulation as contours.

simulated for PI. There are only slight decreases of the AEJ and TEJ, as well as a slight increase of the monsoon flow at H2k as compared to the H0k simulation.

The effects of the evolution of the wind system over the Holocene on the North African rain belt are shown as anomaly plots in Fig. 7.7. As expected, the simulated rain belt is wider and more intense at H4k (Fig. 7.7c) and H6k (Fig. 7.7f) compared to PI climate. This is in a good agreement with previous studies, which have found indicators for higher lake level or the presence of lakes during the early and mid-Holocene [e. g., Gasse, 1987; Schuster et al., 2005; Sereno et al., 2008]. For the H2k simulation (Fig. 7.7a) only inside the core region of the North African rain belt, near Guinea, more precipitation than for H0k is simulated.

The intensified amount of precipitation causes a depletion of δD_P, over the complete North African area, in the H6k simulation as compared to H0k (Fig. 7.7e). This depletion of δD_P in mid-Holocene becomes stronger from west to east, which weakens the positive west-east gradient as shown for PI (Fig. 7.4c) and PD (see Chapter 6.3). The strongest isotopic signal, with a negative anomaly of approx. 35–40‰, is simulated in the Chad region. This agrees with the findings by Gasse [2002], who also has found a decrease of the reconstructed $\delta^{18}O_P$ from study sides in the area of the Holocene lake "Mega-Chad" during the wet Holocene period. Furthermore, Niedermeyer et al. [2010] have detected a depletion of δD by -18‰ in the n-C_{31} of leaf waxes, extracted from sediment-core GeoB9508 (located: 15°N and 17°W). Moreover, the anomaly of the simulated δD_P is in agreement with a general negative correlation between amount of precipitation and δD_P as well as with a gradual continental effect in the isotopic composition. The difference plot of H4k − H0k (Fig. 7.7d) shows a similar pattern as H6k − H0k, but with weaker anomalies. In contrast, the anomaly of H2k with regard to H0k (Fig. 7.7b) shows only a slight depletion of δD_P in the Sahel.

Previous model studies, performed with the ECHAM4-wiso model [Herold, 2011], also indicate a stronger summer monsoon during mid-Holocene compared to industrial climate as well as the negative relation between rainfall amount and δD_P. However, the pattern simulated by Herold [2011] show an eastward shift in the precipitation and δD_P anomaly compared to the results presented in this study. This shift in the spatial distribution might caused e. g. by the different oceanic boundary conditions of SST or the older model version.

7.2.3 *Comparison between simulations and proxy data*

For the comparison of the simulated precipitation and δD_P with proxy data, the estimated δD_P signal of GeoB7920 [B. Beckmann, personal communication] is used. The

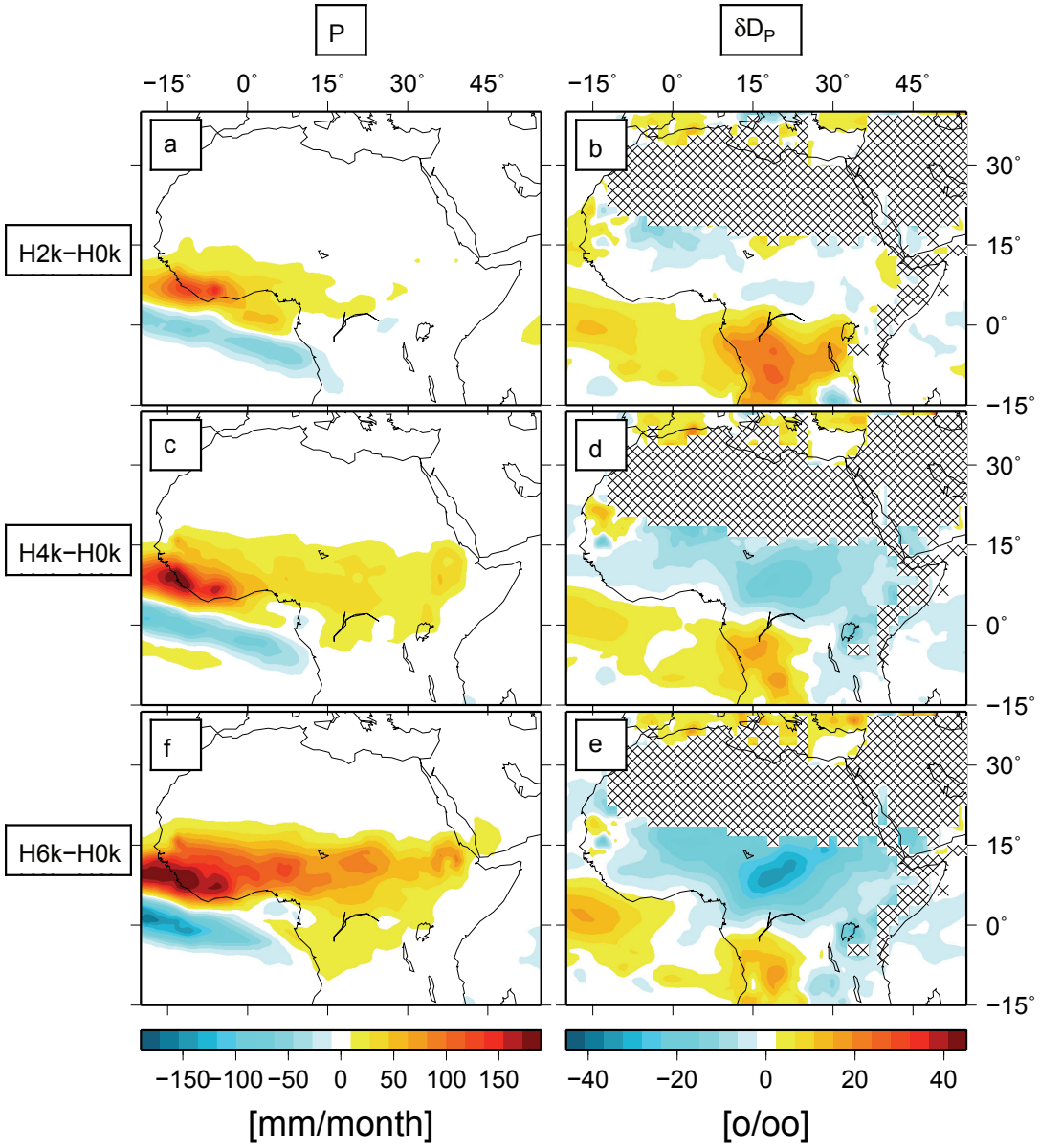

Figure 7.7.: As 7.5, but for precipitation (left) and δD_P (right). The hatched area in the right figures mark those grid boxes where the simulated precipitation is less then 1mm/month.

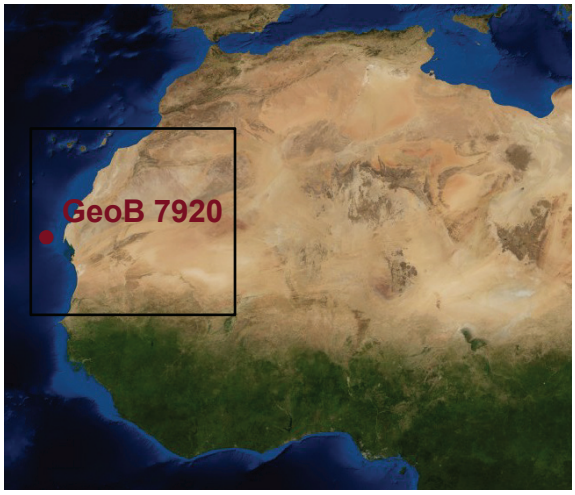

Figure 7.8.: Location of the sediment cores GeoB7920 [B. Beckmann, personal communication]. The black box marks the simulated area (18°W to 0°W and 15°N to 31°N). [Source of background map: http://visibleearth.nasa.gov, NASA.]

estimated catchment area of GeoB7920 is from the west coast to 0°W and 15°N to 31°N. Beckmann measured the δD signal in C_{29} *n*-alkanes with a high temporal resolution, which is used to approximate δD_P as described in Chapter 2.4.

The comparison of the simulated precipitation over the last 6,000 years (T6000 experiment) as well as the simulated isotopic composition δD_P of the time-slice experiments with the proxy data are shown in Fig. 7.9. The reconstructed δD_P signal indicates relative stable, wet conditions from 7ka until 6ka BP. After mid-Holocene the proxy signal shows a gradual transition from relatively wet conditions in 6ka BP to drier conditions at approx. 1.5ka BP. The simulated δD_P changes (red diamonds) agrees very well with the shift of the reconstructed δD_P values. Moreover, the simulated evolution of precipitation in the catchment area also indicates the gradual transition from the relatively wet mid-Holocene to the arid PD conditions.

Figure 7.10 shows the simulated JJAS (left) and annual (right) precipitation and its δD_P signal for the approximated catchment area of GeoB7920. The PI values are shown as absolute values and the H2k, H4k, and H6k simulations are presented as anomalies with respect to H0k. It is shown that the southwards shift as well as the amplification of the North African summer rain belt from mid-Holocene to PI is influencing the annual precipitation in the catchment area with additional precipitation of 45mm/year for H6k, of 18mm/year for H4k, and of 5mm/year for H2k (calculated as field mean over the catchment area). By analyzing the anomalies of δD_P it is found that the depletion of -19‰ (Fig. 7.9) from 6ka compared to PI is most likely caused by the increased summer rainfall at 6ka, due to the linear relation between precipitation amount and δD_P. In contrast, the simulated precipitation at H4k shows positive anomalies for both summer

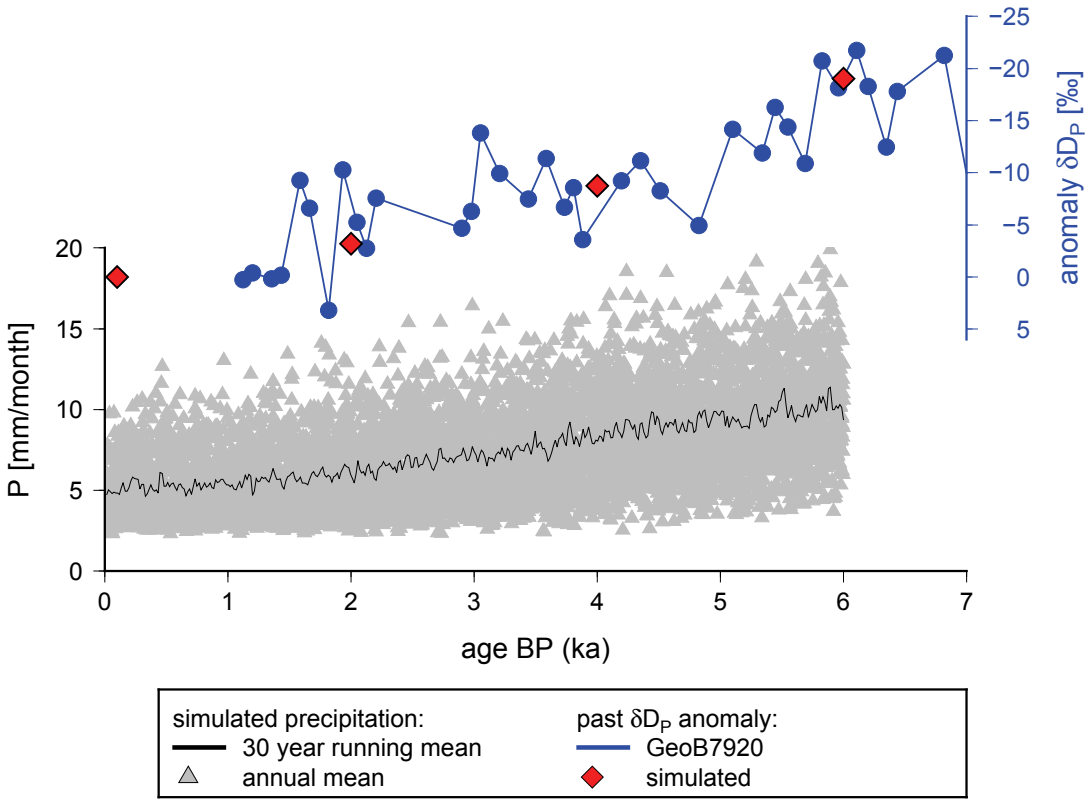

Figure 7.9.: Estimated Holocene δD_P anomalies (as compared to the median δD_P value of the last 1,000 years) derived from measured δD values of n-C_{29} alkanes from marine sediment core GeoB7920 (blue). The red diamonds represent the modeled δD_P anomalies from the time slice simulations. The modeled North-West African precipitation of the transient experiment (by Fischer and Jungclaus, 2011) is shown as monthly, annual mean values (grey) and as a running 30 year mean (black). All simulation results are averaged over the area 18°W–0°W and 15°N–31°N.

rainfall (south) and winter rainfall (north, not shown) compared to PI, thus the simulated anomaly of δD of -9‰ (Fig. 7.9) is presumably not a clear summer monsoon signal, only. In the H2k experiment compared to the H0k one, only a slight change of δD_P (-3‰) is detectable, which can not be seen as a clear signal due to changes in the precipitation amount over the area 18°W to 0°W and 15°N to 31°N.

7.3 DISCUSSION AND IMPLICATIONS

The results of the transient model experiment of Fischer and Jungclaus [2011] indicate a gradual change in precipitation as also seen by Liu et al. [2007]. However, in contrast to Liu et al. [2007] this transient experiment T6000 does not show a rapid desertification

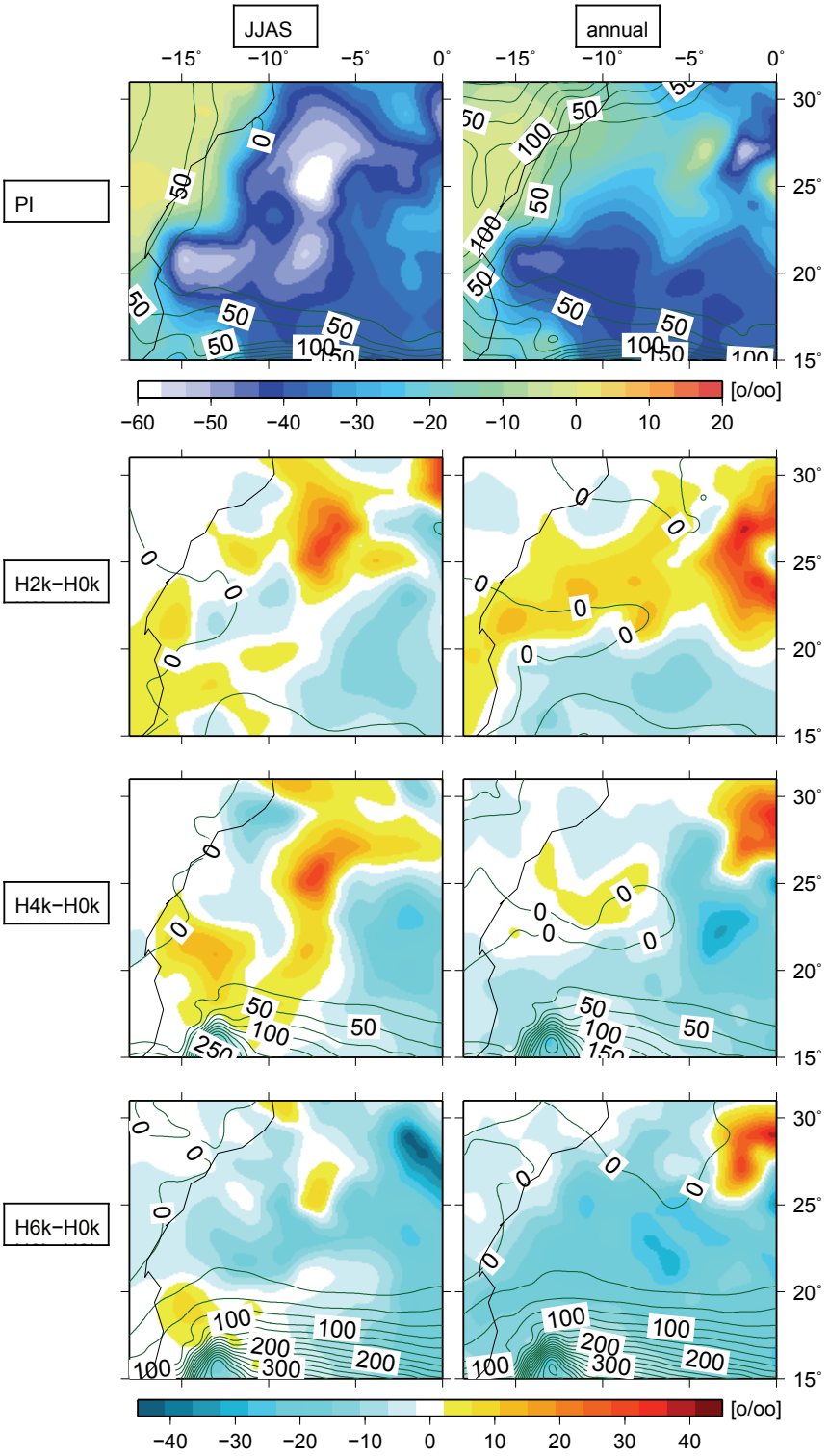

Figure 7.10.: Simulated precipitation of the time-interval (contours) and its δD_P signal (color map) for Area1 (18°W to 0°W and 15°N to 31°N, see Fig. 7.3), for the rainy season (left) and annual mean (right). The upper row shows the absolute PI values of the H0k experiment, the precipitation in [mm] and the δD_P in [‰]. The H2k, H4k, and H6k simulations are presented as anomalies with respect to H0k.

or change in vegetation cover. A reason for this difference could be the finer model resolution compared to the earlier studies.

Forced by insolation changes [e. g., Rossignol-Strick, 1983; Fischer and Jungclaus, 2011] and amplified by feedback mechanisms as SST changes [Kutzbach and Liu, 1997] or vegetation changes [Claussen and Gayler, 1997], the North-West African summer monsoon was weakening over the Holocene. Furthermore, the North African rain belt, including the ITCZ, was located more north during the mid-Holocene than today. A similar finding was already discussed by Herold and Lohmann [2009] for the Eemian and by Herold [2011] for the Holocene. The northwards shift of the rain belt is accompanied by an intensified cloud cover over the northern hemisphere low latitudes [Fischer and Jungclaus, 2011] and an intensified TEJ during mid-Holocene as compared to PI. As a result, the North African rain belt was amplified and enlarged during the early and mid-Holocene. All these changes can also be found in the performed time-slices experiments.

Due to the shift in amount of precipitation the simulated δD_P changes as well. The δD_P is relatively depleted in the area of increased precipitation in H6k compared to PI. This depletion in δD_P is caused by the negative correlation between amount of precipitation and its isotopic composition, which is a typical characteristic of the African monsoon rainfall (see also Chapter 6). For the Holocene time-slice experiments, the simulated precipitation decreases, which is accompanied by an enrichment of δD_P. However, the shift of the isotopic composition of precipitation is not linear (Fig. 7.7). Due to changes of the wind structure the source area of the precipitated water is most likely shifted as well.

Both the simulated precipitation of the transient climate simulation as well as the reconstructed δD_P values of sediment core GeoB7920 show a gradual transition from the wetter mid-Holocene to the PD conditions. These findings are supported by the simulated δD_P values of the time-slice simulations. Moreover, the temporal changes as well as the absolute values of the simulated δD_P anomalies are in a very good agreement with the reconstructed data. Both data sets, independent from each other, indicate a depletion (anomaly) of approx. -20‰ in δD_P between 6ka BP and modern conditions. The weakening of the anomaly over the Holocene, with an increase of approx. 10‰ from 6ka BP to 4ka BP and 5‰ from 4ka BP to 2ka BP, has the same amplitude for the simulated and reconstructed δD_P values.

Summarizing the results of this Chapter, it is concluded that both the climate simulations as well as the proxy data imply a more gradual evolution of the North-West African hydrological cycle between 6ka BP and 1.5ka BP.

8

FINAL CONCLUSIONS AND OUTLOOK

This chapter summarizes the main results of the Chapters 5, 6, and 7 and discusses their main implications regarding the research questions listed in Chapter 1.2. Finally, an outlook is given as to which topics still require further investigation and how such research could be carried out in the future.

8.1 CONCLUSION

Within this thesis the coupled atmosphere-land surface model, ECHAM5-JSBACH, has been successfully enhanced with an explicit stable water isotope diagnostic. This new model development, called ECHAM5-JSBACH-wiso, is evaluated in Chapter 5. Using the coupled model rather than the stand alone version ECHAM5-wiso, the simulated temperature and surface albedo differs remarkably on a global scale. Furthermore, the simulated soil wetness also differs between the models. However, the global distribution of the simulated precipitation is very similar.

The first part of this PhD study deals with the question: **"How much do fractionation processes over land surfaces influence the global distribution of the isotopic composition in precipitation?"** It has been shown that the ECHAM5-JSBACH-wiso model simulates the isotopic composition of precipitation in good agreement with observations from the GNIP database. The root mean square error (RMSE) between the selected GNIP station $\delta^{18}O$ data and the simulation results is approximately 1.8‰–2.2‰, depending on the chosen model resolution. These results are comparable with those of the ECHAM5-wiso model. In order to test the influence of fractionation processes over land surface, three model setups are used. The sensitivity studies in Chapter 5.5 reveal very similar results for the three setups, where either no fractionation processes over land (noF), fractionation during evaporation, only (FE), or fractionation during both evaporation and transpiration (FET) is assumed. The simulations with the FE and FET setup produce a slightly higher depletion up to 1‰ in $\delta^{18}O$ in precipitation compared to the noF setup. Furthermore, in the (sub)tropics, for the FET setup an enrichment of precipitation of the same magnitude can be detected. However, since the FET setup assumes an unrealistically strong fractionation, in reality this increase of heavy isotopes in precipitation is certainly weaker or non existent. In summary, it is concluded that including fractiona-

tion processes over land does not lead to a substantial improvement or change of the isotopic composition in precipitation on a global scale.

As a second part of this PhD study the (present-day) North-West African climate is investigated. Here the research question **"What is the relation between the amount of precipitation and its isotopic composition in North-West Africa?"** is addressed. It is demonstrated, that the ECHAM5-JSBACH-wiso model is able to simulate North-West African climate seasonality as well as the spatial distribution of precipitation and its isotopic composition, in a good agreement with available observations. However, the model strongly underestimates the amount of summer precipitation. From the model results, a linear relation between the amount of rainfall and δD_P can be quantified for the West Sahel region. The calculated transfer function links changes of -5‰ in δD_P to an increase of 100 mm in the yearly amount of rainfall under present-day conditions.

The final overall research topic of this PhD thesis is related to the question: **"Was the change of the hydrology in North-West Africa characterized by a more gradual or abrupt transition during the Holocene?"** To answer this question, firstly an existing transient experiment from 6,000 BP to present with the fully coupled Earth system model COSMOS is analyzed regarding the evolution of North-West African precipitation amount and vegetation. Both the transition of vegetation cover as well as the reduction of precipitation amount are simulated as a gradual transition. Based on this transient experiment, four new times slice simulations, for 6,000 years BP, 4,000 years BP, 2,000 years BP, and PI, are carried out with the ECHAM5-JSBACH-wiso model. The time slice experiments indicate an increase and a northward expansion of the North-West African summer monsoon at 6,000 years BP. The intensified amount of rainfall causes a depletion of δD_P over the whole North African monsoon area, which is in agreement with previous studies. Furthermore, the simulated δD values of the time slice experiments are in very good agreement with a recently reconstructed, high resolution record of δD in precipitation, derived from δD measurements on leaf waxes in the marine sediment core GeoB7920 [B. Beckmann, personal communication]. Both independent methods for analyzing the evolution of δD in North-West African precipitation indicate nearly identical values, and support the hypothesis of a gradual transition from the African Humid Period towards modern dry conditions.

8.2 OUTLOOK

The research presented in this PhD thesis successfully addressed all proposed research questions. However, it also reveals some model deficits as well as some needs for further

research. For example, further investigations in the following research areas might be encouraged:

- In Chapter 5 the influence from fractionation processes over land surface on the global distribution of stable water isotopes in precipitation is analyzed. However, the simulated pattern of the isotopic composition of soil moisture was not evaluated. Recently established networks for isotope measurements in the biosphere, like BASIN (Biogeosphere-Atmosphere Stable Isotope Network) or MIBA (Moisture Isotopes in the Biosphere and Atmosphere), observing the isotopic compositions of soil water, have been operational for only a limited time so far. Hence, the available data do not yet represent long-term annual mean values, but this will hopefully change during the next few years. Comprehensive model-data comparisons of the isotopic composition of soil moisture will then be possible on a global scale.

- One possible future model development would be to include a more complex multi-layer soil scheme in the ECHAM5-JSBACH-wiso model. Since evaporation occurs mainly in the upper soil layers and the water transpired by plants might have (depending on the plant type) deeper layers serving as a water source, the inclusion of a multilayer soil scheme may improve the simulation of the evapotranspiration fluxes. Such a model would allow to analyze the impact of vegetation changes on the isotopic composition of precipitation, as recently done for proxy data by Mix et al. [2013].

- In Chapter 6 it is shown that it is not possible to adequately simulate the Sahel drought event during the 1970's–1980's, even if using a nudged model simulation. Di Giuseppe et al. [2013] have recently shown that the ERA40 re-analysis data is unrealistically humid in the Sahel during the 70's and 80's and propose a real-time correction of this set of data. If this real-time correction of this data set would improve the simulation results with respect to the Sahelian precipitation is still an open question.

- This study is an example that combined results of ECHAM5-JSBACH-wiso simulations and analysis of the δD in leaf water improve the understanding of processes governing the isotopic composition within the proxy data. Therefore, this tool could also be used for other regions or time-slices. Furthermore, it would be very useful to embed an isotope diagnostic for leaf water within the JSBACH module. Such a model development may improve the interpretation of the estimated δD in precipitation retrieved from the isotopic composition in plant waxes.

- Since the ocean model MPI-OM has also been equipped with stable water isotopes [Xu et al., 2012], it will be possible to run simulations with the fully coupled GCM COSMOS enhanced by a stable water isotope module. Such a model would allow simulations of transient experiments enhanced with a stable water isotope diagnostic. Thus, the possibility to perform future model-data comparison studies will have been greatly expanded.

APPENDIX

A

THE ISOTOPIC COMPOSITION OF RECYCLED WATER

In Chapter 5.5.1 the influence of fractionation processes on land surface on the global pattern of $\delta^{18}O_P$ is investigated.

For this study, the following three model setups are used: FE — isotope fractionation occurs during evaporation processes, only; FET — isotope fractionation occurs during both evaporation and transpiration processes; noF — no fractionation occurring during evapotranspiration processes over land surface. In the anomaly pattern of $\delta^{18}O_P$ for $FE - noF$ and $FET - noF$ (Chapter 5.5.1, Fig. 5.11) positive and negative isotope deviations can be detected. The positive anomalies are counter-intuitive. One would assume that a fractionation during evapotranspiration processes will always lead to more depleted $\delta^{18}O$ values of the vapor above land surfaces and, consequently, also to more depleted $\delta^{18}O$ values in precipitation. Here an example is used to clarify, why positive anomalies in $\delta^{18}O_P$ are possible with enhanced fractionation during evapotranspiration. As an example, an South African region (spatial average of the area 15°E to 33°E and 20°S to 12°S), where one of the strongest positive anomaly of $FET - noF$ of $\delta^{18}O_P$ is displayed (Chapter 5.5.1, Fig. 5.11b), is chosen. The positive anomalies of $\delta^{18}O_P$ for $FET - noF$ as well as for $FE - noF$ in other regions can be explained in a similar manner.

As shown in Fig. A.1, the included fractionation during evaporation from bare soil and transpiration leads to an enrichment of $\delta^{18}O_{ws}$ in the FET setup compared to the noF setup. The arithmetic annual mean difference in $\delta^{18}O_{ws}$ between both setups is approx. 8‰ (Fig. A.1, top panel). For the evapotranspiration flux in the noF setup, the water has the same isotopic composition (approx. -10‰) as it's source (Fig. A.1, top and middle panel: red lines), as we assume no fractionation during evapotranspiration. On the opposite, in the FET setup due to the fractionation process the isotopic composition of the evapotranspiration flux ($\delta^{18}O_{ET}$) is approx. 6‰ more depleted then the soil water, resulting in a arithmetic mean $\delta^{18}O_{ET}$ value of -8‰. Thus, $\delta^{18}O_{ET}$ for FET is more enriched than for noF, despite the additional fractionation. This delta difference is then imprinted to (and diluted within) the vapour above this region and kept during condensation processes (identical fractionation effects for the noF and FET case). In the end, a small, but noticeable remaining positive anomaly of $\delta^{18}O_P$ for the FET setup as compared to noF can be detected (Fig. A.1, bottom panel).

Furthermore, to evaluate the isotopic balance of the soil water reservoir, the yearly incoming and outgoing fluxes are estimated, as shown in Fig. A.2. Since the surface

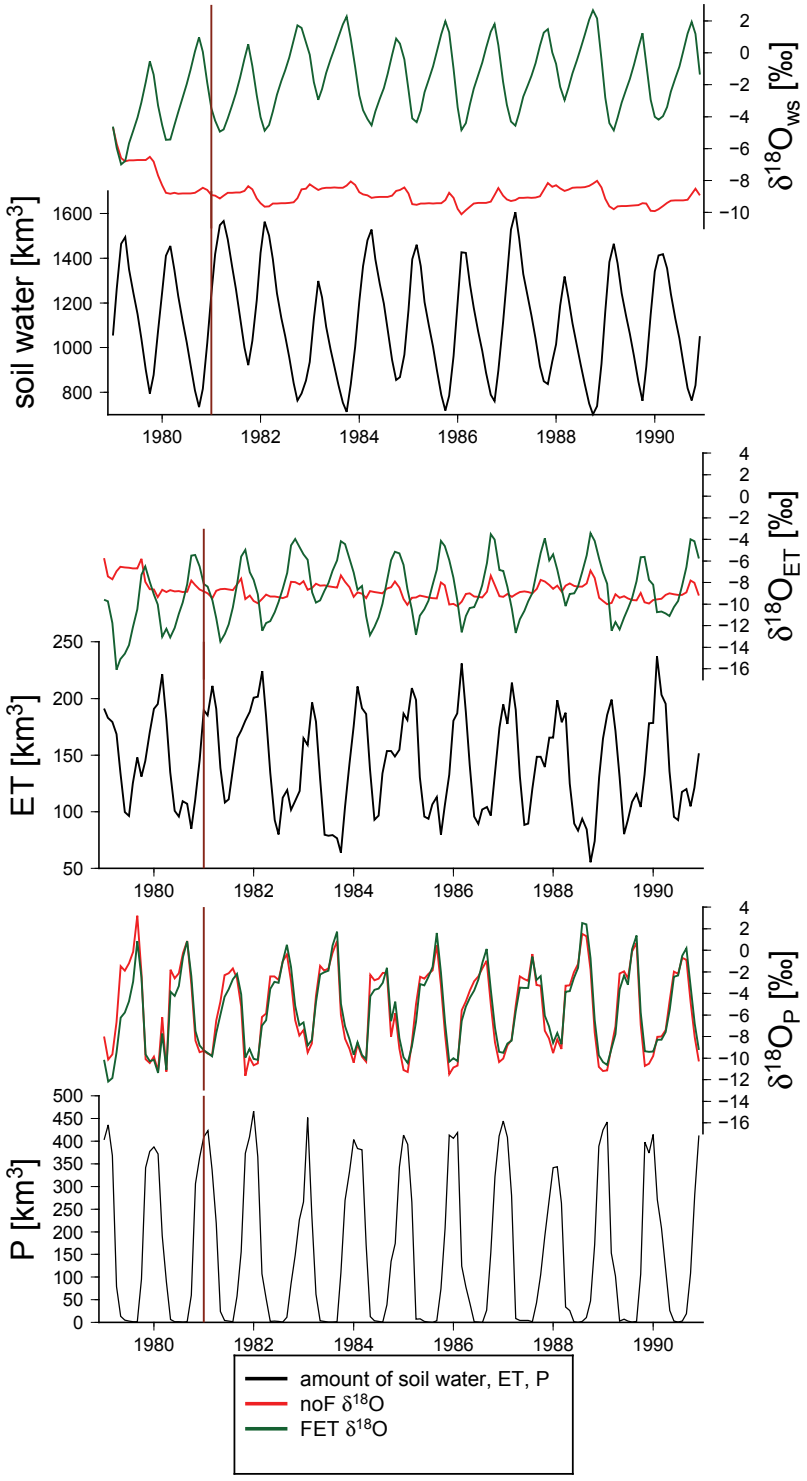

Figure A.1.: (Top) Amount of soil water (black) in [km^3] over the area 15°E to 33°E and 20°S to 12°S and it's isotopic composition $\delta^{18}O_{ws}$ for the noF-setup (red) and the FET-setup (green) in [‰]. (Middle) The same as in the top panel, but for evapotranspiration. (Bottom) The same as in the top panel, but for precipitation. The ruby line marks the end of the spin-up period.

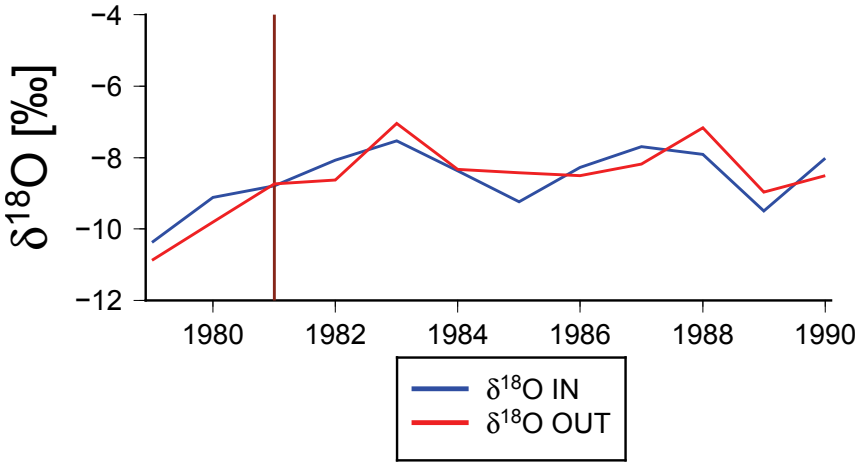

Figure A.2.: Annual mean isotopic composition of water that comes into soil (IN=P-runoff [‰]) and its output (OUT=ET+drainage [‰]) as fealdmean over the area 15°E to 33°E and 20°S to 12°S. The ruby line marks the end of the spin-up period.

runoff never interacts with the soil water the input is calculated as $IN = P - runoff$ while the output is written as $OUT = ET + drainage$. In Fig. A.2 it is shown that the isotopic composition of incoming and outgoing water for the example area has the same magnitude, which means the soil water is isotopically balanced.

B

CLASSIFICATION OF MODEL RESULTS INTO RAINFALL ANOMALY PATTERN

In order to classify the simulated years of the nudged ECHAM5-JSBACH-wiso experiment (Chapter 6.1) into different rainfall anomaly pattern described in Chapter 3.3.1, two approaches are taken. First, the simulated rainfall anomaly over the season JJAS has been visualized and second the field mean over the area from 18°W–10°E and 5°N–20°N has been analyzed. Only if both result give the same classification of a rainfall anomaly, the simulation year has been associated with one of the precipitation anomaly pattern. The following table shows the classification of the simulation years into the different rainfall anomaly pattern, as well as the calculated anomalies of precipitation and its isotopic composition.

year	anomaly pattern					Western Sahel		core region	
	dipole		non-dipole		NA	P	δD_P	P	δD_P
	dry	wet	dry	wet		[mm]	[‰]	[mm]	[‰]
1958		1				45.35	3,98	47.78	1,46
1959		1				51.32	-0,07	14.15	-1,28
1960				1		89.99	-7,91	-30.57	-6,94
1961		1				89.51	-2,26	70.51	-3,89
1962					1	6.14	0,20	6.54	-1,24
1963				1		15.94	-0,37	-15.53	2,77
1964		1				17.87	0,90	24.98	-1,42
1965					1	-17.30	1,62	-30.08	1,30
1966		1				-2.18	0,11	8.62	0,64
1967	1					-57.62	4,96	-26.19	4,26
1968				1		32.58	-3,84	20.56	-1,20
1969					1	-20.41	0,01	1.40	1,80
1970					1	-19.26	0,94	-17.77	-1,53
1971					1	-12.03	1,05	20.55	3,60
1972		1				75.43	-5,49	-6.48	-1,97
1973	1					-65.58	2,21	-52.35	2,74
1974			1			-26.36	1,01	21.43	3,31

1975			1			-13.28	3,37	19.52	2,54
1976			1			-8.86	4,01	27.76	3,14
1977		1				5.60	1,57	43.23	-1,44
1978		1				4.34	3,24	1.75	0,93
1979			1			-6.85	-1,17	-18.29	2,26
1980	1					-28.65	1,26	-37.53	1,84
1981					1	-17.90	0,86	22.32	0,53
1982					1	-0.61	3,91	-13.64	1,19
1983				1		19.32	-0,39	-8.82	-0,50
1984				1		113.13	-8,97	45.38	-7,76
1985				1		39.92	-4,60	26.89	-5,40
1986		1				1.47	-1,03	5.37	-2,86
1987	1					-69.64	0,24	-57.05	0,37
1988	1					-122.60	2,78	-89.65	4,49
1989				1		57.07	-5,08	9.63	-4,38
1990			1			-62.55	1,35	-9.76	4,06
1991	1					-43.47	-0,29	2.56	2,77
1992			1			-33.19	3,53	-30.94	4,37
1993			1			-25.66	-1,78	-9.50	-3,55
1994				1		32.99	0,74	51.80	-0,83
1995	1					-60.55	1,28	-35.80	2,14
1996					1	5.69	-2,80	30.73	-2,79
1997		1				80.72	-3,23	16.72	-1,40
1998			1			-113.57	9,72	-79.97	8,08
1999				1		26.56	0,82	-4.82	-0,36
2000					1	-9.61	3,68	-4.44	0,49
2001				1		35.01	-0,63	46.11	-1,56
2002			1			-8.21	3,14	-7.01	2,49

Table B.1.: Distinguishing between the dipole and non-dipole rainfall anomaly pattern for each simulation year of the nudged ECHAM5-JSBACH-wiso experiment (Chapter 6.1). The simulated annual rainfall anomaly and the corresponding anomaly of δD_P are calculated for both the West Sahel region and the catchment area of core GeoB9501 ("core region"). All anomalies are calculated with respect of the JJAS mean values of the simulation period.

BIBLIOGRAPHY

[1] Ackerley, D., Booth, B. B., Knight, S. H. E., Highwood, E. J., Frame, D. J., Allen, M. R., and Rowell, D. P. (2011). Sensitivity of twentieth-century Sahel rainfall to sulfate aerosol and CO_2 forcing. *Journal of Climate*, 24(19):4999–5014.

[2] Adkins, J., deMenocal, P., and Eshel, G. (2006). The "African humid period" and the record of marine upwelling from excess ^{230}Th in Ocean Drilling Program Hole 658C. *Paleoceanography*, 21(4):4203–4216.

[3] Aleinov, I. and Schmidt, G. A. (2006). Water isotopes in the GISS ModelE land surface scheme. *Global and Planetary Change*, 51:108–120.

[4] Allison, G. B. and Hughes, M. W. (1983). The use of natural tracers as indicators of soil-water movement in a temperate semi-arid region. *Journal of Hydrology*, 60:157–173.

[5] Andreae, M. O. (1995). Chapter 10 Climatic effects of changing atmospheric aerosol levels. In A. Henderson-Sellers, editor, *Future climates of the world: a modelling perspective*, volume 16 of *World Survey of Climatology*, pages 347–398. Elsevier.

[6] Beckmann, B., Niedermeyer, E. M., Sessions, A. L., and Schefuß, E. (2013). Hydrogen isotope ratios of plant lipids record variations of continental hydrology off NW Africa during the 20th century. Manuscript sumbitted for publication to: Geochimica et Cosmochimica Acta.

[7] Berger, A. L. (1978). Long-term variations of daily insolation and Quaternary climatic changes. *Journal of the Atmospheric Sciences*, 35(12):2362–2367.

[8] Berrisford, P., Dee, D., Fielding, K., Fuentes, M., Kallberg, P., Kobayashi, S., and Uppala, S. (2009). The ERA-Interim archive, ERA Report Series, European Centre for Medium Range Weather Forecast. ERA Report Series, European Centre for Medium Range Weather Forecast, Shinfield Park, Reading, Berkshire RG29AX, United Kingdom.

[9] Braconnot, P., Otto-Bliesner, B., Harrison, S., Joussaume, S., Peterchmitt, J. Y., A. Abe-Ouchi, M. C., Driesschaert, E., Fichefet, T., Hewitt, C. D., Kageyama, M., Kitoh, A., Laîné, A., Loutre, M.-F., Marti, O., Merkel, U., Ramstein, G., Valdes, P., Weber, S. L., Yu, Y., and Zhao, Y. (2007a). Results of PMIP2 coupled simulations of the Mid-Holocene

and Last Glacial Maximum - Part 1: experiments and large-scale features. *Climate of the Past*, 3:261–277.

[10] Braconnot, P., Otto-Bliesner, B., Harrison, S., Joussaume, S., Peterchmitt, J. Y., Abe-Ouchi, A., Crucifix, M., Driesschaert, E., Fichefet, T., Hewitt, C. D., Kageyama, M., Kitoh, A., Loutre, M.-F., Marti, O., Merkel, U., Ramstein, G., Valdes, P., Weber, L., Yu, Y., and Zhao, Y. (2007b). Results of PMIP2 coupled simulations of the Mid-Holocene and Last Glacial Maximum - Part 2: feedbacks with emphasis on the location of the ITCZ and mid- and high latitudes heat budget. *Climate of the Past*, 3(2):279–296.

[11] Braud, I., Bariac, T., Gaudet, J. P., and Vauclin, M. (2005). SiSPAT-Isotope, a coupled heat, water and stable isotope (HDO and $H_2^{18}O$) transport model for bare soil. Part I. Model description and first verifications. *Journal of Hydrology*, 309:277–300.

[12] Bretagnon, P. and Francou, G. (1988). Planetary theories in rectangular and spherical variables - VSOP 87 solutions. *Astronomy and Astrophysics*, 202:309–315.

[13] Brovkin, V., Raddatz, T., Reick, C. H., Claussen, M., and Gayler, V. (2009). Global biogeophysical interactions between forest and climate. *Geophysical Research Letters*, 36(7):L07405.

[14] Cadet, D. L. and Nnoli, N. O. (1987). Water vapour transport over Africa and the Atlantic Ocean during summer 1979. *Quarterly Journal of the Royal Meteorological Society*, 113(476):581–602.

[15] Castañeda, I. S., Mulitza, S., Schefuß, E., dos Santos, R. A. L., Damsté, J. S. S., and Schouten, S. (2009). Wet phases in the Sahara/Sahel region and human migration patterns in North Africa. *Proceedings of the National Academy of Sciences*, 106(48):20159–20163.

[16] Charney, J. G. (1975). Dynamics of deserts and drought in the Sahel. *Quarterly Journal of the Royal Meteorological Society*, 101(428):193–202.

[17] Charney, J. G. and Stern, M. E. (1962). On the stability of internal baroclinic jets in a rotating atmosphere. *Journal of Atmospheric Sciences*, 19(2):159–172.

[18] Clark, I. D. and Fritz, P. (1997). *Environmental Isotopes in Hydrogeology*. CRC press.

[19] Claussen, M. (1997). Modeling bio-geophysical feedback in the African and Indian monsoon region. *Climate Dynamics*, 13(4):247–257.

[20] Claussen, M. and Gayler, V. (1997). The greening of the Sahara during the mid-Holocene: results of an interactive atmosphere-biome model. *Global Ecology and Biogeography Letters*, 6(5):369–377.

[21] Claussen, M., Kubatzki, C., Brovkin, V., Ganopolski, A., Hoelzmann, P., and Pachur, H.-J. (1999). Simulation of an abrupt change in Saharan vegetation in the mid-Holocene. *Geophysical Research Letters*, 26(14):2037–2040.

[22] Collins, J. A., Schefuß, E., Mulitza, S., Prange, M., Werner, M., Tharammal, T., Paul, A., and Wefer, G. (2013). Estimating the hydrogen isotopic composition of past precipitation using leaf-waxes from western Africa. *Quaternary Science Reviews*, 65:88–101.

[23] Craig, H. (1961). Isotopic variations in meteoric waters. *Science*, 133(3465):1702–1703.

[24] Craig, H. and Gordon, L. I. (1965). Deuterium and oxygen 18 variations in the ocean and the marine atmosphere. In Tongiorgi, E., editor, *Stable Isotopes in Oceanographic Studies and Paleotemperature*, pages 9–130. V. Lishi e F., Pisa, Italy.

[25] Criss, R. E. (1999). *Principles of Stable Isotope Distribution*. Oxford University Press.

[26] Cuntz, M., Ciais, P., and Hoffmann, G. (2002). Modelling the continental effect of oxygen isotopes over Eurasia. *Tellus B*, 54(5):895–911.

[27] Cuntz, M., Ciais, P., Hoffmann, G., and Knorr, W. (2003). A comprahensive global three-dimensional model of $\delta^{18}O$ in atmospheric CO_2: 1. Validation of surface processes. *Journal of Geophysical Research: Atmospheres*, 108(D17):2156–2202.

[28] Dallmeyer, A. (2008). Simulation des Nordafrikanischen Sommermonsuns in ECHAM5 - Analyse der Modellempfindlichkeit. Master Thesis, Universität Hamburg.

[29] Dansgaard, W. (1964). Stable isotopes in precipitation. *Tellus*, 16(4):436–468.

[30] Dee, D. P., Uppala, S. M., Simmons, A. J., Berrisford, P., Poli, P., Kobayashi, S., Andrae, U., Balmaseda, M. A., Balsamo, G., Bauer, P., Bechtold, P., Beljaars, A. C. M., van de Berg, L., Bidlot, J., Bormann, N., Delsol, C., Dragani, R., Fuentes, M., Geer, A. J., Haimberger, L., Healy, S. B., Hersbach, H., Hólm, E. V., Isaksen, L., Kållberg, P., Köhler, M., Matricardi, M., McNally, A. P., Monge-Sanz, B. M., Morcrette, J.-J., Park, B.-K., Peubey, C., de Rosnay, P., Tavolato, C., Thépaut, J.-N., and Vitart, F. (2011). The ERA-Interim reanalysis: configuration and performance of the data assimilation system. *Quarterly Journal of the Royal Meteorological Society*, 137(656):553–597.

[31] deMenocal, P., Ortiz, J., Guilderson, T., Adkins, J., Sarnthein, M., Baker, L., and Yarusinsky, M. (2000). Abrupt onset and termination of the African Humid Period: rapid climate responses to gradual insolation forcing. *Quaternary Science Reviews*, 19(1):347–361.

[32] Di Giuseppe, F., Molteni, F., and Dutra, E. (2013). Real time correction of ERA-Interim monthly rainfall. *Geophysical Research Letters*, 40(14):3750–3755.

[33] DKRZ (1992). The ECHAM3 Atmospheric General Circulation Model. Technical Report 6, Deutsches Klimarechenzentrum, Hamburg, Germany.

[34] Druyan, L. M. (1996). Science Briefs: African Wave Disturbances and African Drought. last access: 2013-04-20.

[35] Dümenil, L. and Tondini, E. (1992). *Advances in Theoretical Hydrology, A Tribute to James Dooge*, chapter 9: A rainfall-runoff scheme for use in the Hamburg climate model, pages 129–157. European Geophysical Society series on hydrological science. Elsevier Science.

[36] Dupont, L. (2011). Orbital scale vegetation change in Africa. *Quaternary Science Reviews*, 30(25):3589–3602.

[37] Fink, A. H. (2006). Das Westafrikanische Monsunsystem. *Promet*, 3/4:114–122.

[38] Fischer, M. J. (2006). iCHASM, a flexible land-surface model that incorporates stable water isotopes. *Global and Planatary Change*, 51(1):121–130.

[39] Fischer, N. and Jungclaus, J. H. (2011). Evolution of the seasonal temperature cycle in a transient Holocene simulation: orbital forcing and sea-ice. *Climate of the Past*, 7(4):1139–1148.

[40] Friedman, I. and O'Neil, J. R. (1977). *Compilation of stable isotope fractionation factors of geochemical interest*, volume 440. USGPO.

[41] Gasse, F. (1987). Diatoms for reconstructing palaeoenvironments and paleohydrology in tropical semi-arid zones. *Hydrobiologia*, 154(1):127–163.

[42] Gasse, F. (2002). Diatom-inferred salinity and carbonate oxygen isotopes in Holocene waterbodies of the western Sahara and Sahel (Africa). *Quaternary Science Reviews*, 21(7):737–767.

[43] Gat, J. R. (1996). Oxygen and hydrogen isotopes in the hydrologic cycle. *Annual Review of Earth and Planetary Sciences*, 24(1):225–262.

[44] Gat, J. R., Mookand, W. G., and Meijer, H. (2001). Environmental Isotopes in the Hydrological Cycle. Principles and Applications. Technical Documents in Hydrology 39 Vol. II, International Atomic Energy Agency and United Nations Educational, Scientific and Cultural Organization.

[45] Gazis, C. and Feng, X. (2004). A stable isotope study of soil water: evidence for mixing and preferential flow paths. *Geoderma*, 119(1):97–111.

[46] Giry, C., Felis, T., Kölling, M., Wei, W., Lohmann, G., and Scheffers, S. (2013). Controls of Caribbean surface hydrology during the mid- to late Holocene: insights from monthly resolved coral records. *Climate of the Past*, 9(2):841–858.

[47] Grist, J. P. and Nicholson, S. E. (2001). A study of the dynamic factors influencing the rainfall variability in the West African Sahel. *Journal of Climate*, 14(7):1337–1359.

[48] Haese, B., Werner, M., and Lohmann, G. (2013). Stable water isotopes in the coupled atmosphere-land surface model ECHAM5-JSBACH. *Geoscientific Model Development*, 6:1463–1480.

[49] Hagemann, S., Arpe, K., and Roeckner, E. (2006). Evaluation of the hydrological cycle in the ECHAM5 model. *Journal of Climate*, 19(16):3810–3827.

[50] Hagemann, S., Botzet, M., Dümenil, L., and Machenhauer, B. (1999). Derivation of global GCM boundary conditions from 1 km land use satellite data. MPI Report 289, Max Planck Institute for Meteorology.

[51] Harris, I., Jones, P. D., Osborn, T. J., and Lister, D. H. (2014). Updated high-resolution grids of monthly climatic observations – the CRU TS3.10 Dataset. *International Journal of Climatology*, 34(3):622–642.

[52] Haywood, J. M., Jones, A., Bellouin, N., and Stephenson, D. (2013). Asymmetric forcing from stratospheric aerosols impacts Sahelian rainfall. *Nature Climate Change*, 3(7):660–665.

[53] Herold, M. (2011). *Modelling Stable Isotopes in the Eemian and Holocene Hydrological Cycles*. PhD thesis, Universität Bremen.

[54] Herold, M. and Lohmann, G. (2009). Eemian tropical and subtrobical African moisture transport: an isotope modelling study. *Climate Dynamics*, 33(7-8):1075–1088.

[55] Hoffmann, G. (1995). *Wasserisotope im allgemeinen Zirkulationsmodell ECHAM*. PhD thesis, Universitaet Hamburg.

[56] Hoffmann, G., Werner, M., and Heimann, M. (1998). Water isotope module of the ECHAM atmospheric general circulation model: A study on timescales from days to several years. *Journal of Geophysical Research: Atmospheres*, 103(D14):16871–16896.

[57] Hsieh, J. C. C., Chadwick, O. A., Kelly, E. F., and Savin, S. M. (1998). Oxygen isotopic composition of soil water: qantifying evaporation and transpiration. *Geoderma*, 82:269–293.

[58] IAEA/WMO (2006). Global network of isotopes in precipitation: The gnip database. last access: 2012-24-10.

[59] IPCC (1990). Climate change: The IPCC Scientific Assessment. Technical report, J. T. Houghton, G. J. Jenkins, and J. J. Ephraums, editors. Cambridge University Press.

[60] IPCC (2000). IPCC Special Report on Emissions Scenarios. Technical report, N. Nakicenovic, R. Swart editors. Cambridge University Press, Cambridge, UK.

[61] Joussaume, S., Sadourny, R., and Jouzel, J. (1984). A general circulation model of water isotope cycles in the atmosphere. *Nature*, 311:24–29.

[62] Jouzel, J., Hoffmann, G., Koster, R. D., and Masson, V. (2000). Water isotopes in precipitation:: data/model comparison for present-day and past climates. *Quaternary Science Reviews*, 19(1):363–379.

[63] Jouzel, J., Russell, G. L., Suozzo, R. J., Koster, R. D., White, J. W. C., and Broecker, W. S. (1987). Simulations of the HDO and $H_2^{18}O$ atmospheric cycles using the NASA GISS general circulation model: The seasonal cycle for present-day conditions. *Journal of Geophysical Research*, 92(D12):14739–14760.

[64] Jungclaus, J. H., Keenlyside, N., Botzet, M., Haak, H., Luo, J.-J., Latif, M., Marotzke, J., Mikolajewicz, U., and Roeckner, E. (2006). Ocean circulation and tropical variability in the coupled model ECHAM5/MPI-OM. *Journal of Climate*, 19(16):3952–3972.

[65] Knorr, W. (2000). Annual and interannual CO_2 exchanges of the terrestria biosphere: Process-based simulations and uncertainties. *Global Ecology and Biogeography*, 9(3):225–252.

[66] Krinner, G., Lézine, A.-M., Braconnot, P., Sepulchre, P., Ramstein, G., Grenier, C., and Gouttevin, I. (2012). A reassessment of lake and wetland feedbacks on the North African Holocene climate. *Geophysical Research Letters*, 39(7):L07701.

[67] Krishnamurti, T. N., Xue, J., Bedi, H. S., Ingles, K., and Oosterhof, D. (1991). Physical initialization for numerical weather prediction over the tropics. *Tellus A*, 43(4):53–81.

[68] Kröpelin, S., Verschuren, D., Lézine, A.-M., Eggermont, H., Cocquyt, C., Francus, P., Cazet, J.-P., Fagot, M., Rumes, B., and Russell, J. M. (2008). Climate-driven ecosystem succession in the Sahara: The past 6000 years. *Science*, 320(5877):765–768.

[69] Kutzbach, J., Bonan, G., Foley, J., and Harrison, S. P. (1996). Vegetation and soil feedbacks on the response of the African monsoon to orbital forcing in the early to middle Holocene. *Nature*, 384:623–626.

[70] Kutzbach, J. E. (1981). Monsoon climate of the early Holocene: Climate experiment with the Earth's orbital parameters for 9000 years ago. *Science*, 214(4516):59–61.

[71] Kutzbach, J. E. and Liu, Z. (1997). Response of the African monsoon to orbital forcing and ocean feedbacks in the middle Holocene. *Science*, 278(5337):440–443.

[72] Kutzbach, J. E. and Street-Perrott, F. A. (1985). Milankovitch forcing of fluctuations in the level of tropical lakes from 18 to 0 kyr BP. *Nature*, 317:130–134.

[73] Lau, K. M., Sud, Y., and Kim, J. H. (1996). Intercomparison of hydrologic processes in AMIP GCMs. *Bulletin of the American Meteorological Society*, 77(10):2209–2227.

[74] Lee, J.-E., Fung, I., DePaolo, D. J., and Henning, C. C. (2007). Analysis of the global distribution of water isotopes using the NCAR atmospheric general circulation model. *Journal of Geophysical Research: Atmospheres*, 112:D16306.

[75] LeGrande, A. N. and Schmidt, G. A. (2006). Global gridded data set of the oxygen isotopic composition in seawater. *Geophysical Research Letters*, 33(12):L12604.

[76] Levis, S., Bonan, G. B., and Bonfils, C. (2004). Soil feedback drives the mid-Holocene North African monsoon northward in fully coupled CCSM2 simulations with a dynamic vegetation model. *Climate Dynamics*, 23(7-8):791–802.

[77] Liu, Z., Wang, Y., Gallimore, R., Gasse, F., Johnson, T., deMenocal, P., Adkins, J., Notaro, M., Prentice, I. C., Kutzbach, J., Jacob, R., Behling, P., Wang, L., and Ong, E. (2007). Simulating the transient evolution and abrupt change of Northern Africa atmosphere-ocean-terrestrial ecosystem in the Holocene. *Quaternary Science Reviews*, 26(13):1818–1837.

[78] Majoube, M. (1971a). Fractionnement en oxygene 18 entre la glace et la vapeur d'eau. *J. Chem. Phys.*, 68:625–636.

[79] Majoube, M. (1971b). Fractionnement en oxygene 18 et en deuterium entre l'eau et sa vapeur. *J. Chem. Phys.*, 68(10):1423–1436.

[80] Marsland, S. J., Haak, H., Jungclaus, J. H., Latif, M., and Röske, F. (2003). The Max-Planck-Institute global ocean/sea ice model with orthogonal curvilinear coordinates. *Ocean Modelling*, 5(2):91–127.

[81] Mathieu, R. and Bariac, T. (1996). A numerical model for the simulation of stable isotope profiles in drying soils. *Journal of Geophysical Research: Atmospheres*, 101(D7):12685–12696.

[82] McDermott, F., Atkinson, T. C., Fairchild, I. J., Baldini, L. M., and Mattey, D. P. (2011). A first evaluation of the spatial gradients in $\delta^{18}O$ recorded by European Holocene speleothems. *Global and Planetary Change*, 79(3):275–287.

[83] McGuffie, K. and Henderson-Sellers, A. (2005). *Coupled Climate System Models*, pages 165–212. John Wiley & Sons, Ltd.

[84] McIntosh, S. K. and McIntosh, R. J. (1983). Current directions in West African prehistory. *Annual Review of Anthropology*, 12:215–258.

[85] Merlivat, L. and Jouzel, J. (1979). Global climatic interpretation of the deuterium-oxygen 18 relationship for precipitation. *Journal of Geophysical Research: Oceans*, 84(C8):5029–5033.

[86] Milanković, M. (1969). *Canon of insolation and the ice-age problem: (Kanon der Erdbestrahlung und seine Anwendung auf das Eiszeitenproblem) Belgrade, 1941.* Israel Program for Scientific Translations; [available from U.S. Dept. of Commerce, Clearinghouse for Federal Sciencific and Technical Information, Springfield, Va.], Jerusalem.

[87] Mix, H. T., Winnick, M. J., Mulch, A., and Chamberlain, C. P. (2013). Grassland expansion as an instrument of hydrologic change in Neogene western North America. *Earth and Planetary Science Letters*, 377–378:73–83.

[88] Mohino, E., Janicot, S., and Bader, J. (2011). Sahel rainfall and decadal to multi-decadal sea surface temperature variability. *Climate Dynamics*, 37(3-4):419–440.

[89] Mulitza, S., Krastel, S., and Wefer, G. (2008). Climate History and Sedimentation Processes off NW Africa, Cruise No. 65, June 11 - August 10, 2005, Dakar (Senegal) - Las Palmas (Spain). Technical report, Institut für Meereskunde der Universität Hamburg, Leitstelle METEOR.

[90] NASA (2004). National Aeronautics and Space Administration, NASA Earth Observatory (NASA Goddard Space Flight Center), Blue Marble: Next Generation was produced by Reto Stöckli. last access: 2013-09-20.

[91] Nicholson, S. E. (2000). Land surface processes and Sahel climate. *Reviews of Geophysics*, 38(1):117–139.

[92] Nicholson, S. E. (2009). A revised picture of the structure of the "monsoon" and land ITCZ over West Africa. *Climate dynamics*, 32(7-8):1155–1171.

[93] Nicholson, S. E. and Grist, J. P. (2001). A conceptual model for understanding rainfall variability in the West African Sahel on interannual and interdecadal timescales. *International Journal of Climatology*, 21(14):1733–1757.

[94] Nicholson, S. E. and Grist, J. P. (2003). The seasonal evolution of the atmospheric circulation over West Africa and equatorial Africa. *Journal of Climate*, 16:1013–1030.

[95] Nicholson, S. E. and Webster, P. J. (2007). A physical basis for the interannual variability of rainfall in the Sahel. *Quarterly Journal of the Royal Meteorological Society*, 133(629):2065–2084.

[96] Niedermeyer, E. M., Schefuß, E., Sessions, A. L., Mulitza, S., Mollenhauer, G., Schulz, M., and Wefer, G. (2010). Orbital- and millennial-scale changes in the hydrologic cycle and vegetation in the western African Sahel: insights from individual plant wax δD and δ^{13}C. *Quaternary Science Reviews*, 29(23-24):2996–3005.

[97] Noone, D. and Simmonds, I. (2002). Associations between δ^{18}O of Water and Climate Parameters in a Simulation of Atmospheric Circulation for 1979–95. *Journal of Climate*, 15:3150–3169.

[98] Ossing, F. (2012). Bilder als Klima-Archive? *System Erde*, 2(1):90–95.

[99] Parry, M. L., Canziani, O. F., Palutikof, J. P., van der Linden, P. J., and (eds.), C. E. H. (2007). Contribution of Working Group II to the Fourth Assessment Report of the Intergovernmental Panel on Climate Change. Technical report, IPCC, Cambridge, United Kingdom and New York.

[100] Petit, J.-R., Jouzel, J., Raynaud, D., Barkov, N. I., Barnola, J.-M., Basile, I., Bender, M., Chappellaz, J., Davis, M., Delaygue, G., et al. (1999). Climate and atmospheric history of the past 420,000 years from the Vostok ice core, Antarctica. *Nature*, 399(6735):429–436.

[101] Pongratz, J., Reick, C., Raddatz, T., and Claussen, M. (2007). Reconstruction of global land use and land cover AD 800 to 1992. Technical report, World Data Center for Climate.

[102] Pongratz, J., Reick, C., Raddatz, T., and Claussen, M. (2008). A reconstruction of global agricultural areas and land cover for the last millennium. *Global Biogeochem. Cycles*, 22(3):GB3018.

[103] Raddatz, T. J., Reick, C. H., Knorr, W., Kattge, J., Roeckner, E., Schnur, R., Schnitzler, K.-G., Wetzel, P., and Jungclaus, J. (2007). Will the tropical land biosphere dom-

inate the climate-carbon cycle feedback during the twenty-first century? *Climate Dynamics*, 29(6):565–574.

[104] Ramel, R., Gallée, H., and Messager, C. (2006). On the northward shift of the West African monsoon. *Climate Dynamics*, 26(4):429–440.

[105] Rast, S. (2013). Sea ice and nudging in ECHAM5. last access: 2013-06-25.

[106] Riley, W. J., Still, C. J., Torn, M. S., and Berry, J. A. (2002). A mechanistic model of $H_2^{18}O$ and $C^{18}OO$ fluxes between ecosystems and the atmosphere: Model description and sensitivity analyses. *Global Biogeochemical Cycles*, 16(4):1095–1109.

[107] Risi, C., Bony, S., Vimeux, F., and Jouzel, J. (2010). Water-stable isotopes in the LMDZ4 general circulation model: Model evaluation for present-day and past climates and applications to climatic interpretations of tropical isotopic records. *Journal of Geophysical Research: Atmospheres*, 115:D12118.

[108] Roeckner, E., Bäuml, G., Bonaventura, L., Brokopf, R., Esch, M., Giorgetta, M., Hagemann, S., Kirchner, I., Kornblueh, L., Manzini, E., Rhodin, A., Schlese, U., Schulzweida, U., and Tompkins, A. (2003). Report No. 349 - The atmospheric general circulation model ECHAM5 - Part 1. Technical report, Max-Planck Inst. für Meteorol., Hamburg, Germany.

[109] Roeckner, E., Brokopf, R., Esch, M., Giorgetta, M., Hagemann, S., Kornblueh, L., Manzini, E., Schlese, U., and Schulzweida, U. (2006). Sensitivity of Simulated Climate to Horizontal and Vertical Resolution in the ECHAM5 Atmosphere Model. *Journal of Climate*, 19(16):3771–3791.

[110] Roedel, W. and Wagner, T. (2011). *Physik unserer Umwelt - Die Atmosphäre*, volume 3. Springer-Verlag GmbH.

[111] Rossignol-Strick, M. (1983). African monsoons, an immediate climate response to orbital insolation. *Nature*, 304(5921):46–49.

[112] Rozanski, K., Araguás-Araguás, L., and Gonfiantini, R. (1993). Isotopic patterns in modern global precipitation. In Swart, P. K. e. a., editor, *Climate Change in Continental Isotopic Records*, volume 78 of *Geophysical Monograph Series*, pages 1–36. AGU, Washington, D. C.

[113] Ruddiman, W. F. (2008). *Earth's Climate: Past and Future*. W. H. Freeman.

[114] Sachse, D., Billault, I., Bowen, G. J., Chikaraishi, Y., Dawson, T. E., Feakins, S. J., Freeman, K. H., Magill, C. R., McInerney, F. A., van der Meer, M. T. J., Polissar, P.,

Robins, R. J., Sachs, J. P., Schmidt, H.-L., Sessions, A. L., White, J. W. C., West, J. B., and Kahmen, A. (2012). Molecular Paleohydrology: Interpreting the Hydrogen-Isotopic Composition of Lipid Biomarkers from Photosynthesizing Organisms. *Annual Review of Earth and Planetary Science*, 40:221–249.

[115] SAHRA (2013). University of Arizona, last access: 2013-09-10.

[116] Schmidt, G. A. (1998). Oxygen-18 variations in a global ocean model. *Geophysical Research Letters*, 25(8):1201–1204.

[117] Schmidt, G. A., LeGrande, A. N., and Hoffmann, G. (2007). Water isotope expressions of intrinsic and forced variability in a coupled ocean-atmosphere model. *Journal of Geophysical Research: Atmospheres*, 112:D10103.

[118] Schulz, J.-P., Dümenil, L., and Polcher, J. (2001). On the Land Surface-Atmosphere Coupling and Its Impact in a Single-Column Atmospheric Model. *Journal of Applied Meteorology*, 40:642–663.

[119] Schuster, M., Roquin, C., Duringer, P., Brunet, M., Caugy, M., Fontugne, M., Mackaye, H. T., Vignaud, P., and Ghienne, J.-F. (2005). Holocene Lake Mega-Chad palaeoshorelines from space. *Quaternary Science Reviews*, 24(16-17):1821–1827.

[120] Sereno, P. C., Garcea, E. A. A., Jousse, H., Stojanowski, C. M., Saliège, J.-F., Maga, A., Ide, O. A., Knudson, K. J., Mercuri, A. M., Stafford, T. W., Kaye, T. G., Giraudi, C., Nśiala, I. M., Cocca, E., Moots, H. M., Dutheil, D. B., and Stivers, J. P. (2008). Lakeside Cemeteries in the Sahara: 5000 Years of Holocene Population and Environmental Change. *PLoS ONE*, 3(8):e2995.

[121] Shukla, J. (1981). Dynamical Predictability of Monthly Means. *Journal of the Atmospheric Sciences*, 38(12):2547–2572.

[122] Stärz, M., Lohmann, G., and Knorr, G. (2013). Dynamic soil feedbacks on the climate of the mid-Holocene and the Last Glacial Maximum. *Climate of the Past Discussions*, 9:2717–2770.

[123] Sturm, C., Zhang, Q., and Noone, D. (2010). An introduction to stable water isotopes in climate models: benefits of forward proxy modelling for paleoclimatology. *Climate of the Past*, 6:115–129.

[124] Sultan, B. and Janicot, S. (2003). The West African monsoon dynamics. Part II: The "preonset" and "onset" of the summer monsoon. *Journal of Climate*, 16(21):3407–3427.

[125] Taylor, K. E., Williamson, D., and Zwiers, F. (2000). The sea surface temperature and sea-ice concentration boundary conditions for AMIP II simulations, PCMDI Report No. 60. Technical report, Program for Climate Model Diagnosis and Intercomparison, Lawerence Livermore National Laboratory, Livermore, California, 25pp.

[126] Tindall, J. C., Valdes, P. J., and Sime, L. C. (2009). Stable water isotopes in HadCM3: Isotopic signature of El Niño-Southern Oscillation and the tropical amount effect. *Journal of Geophysical Research: Atmospheres*, 114:D04111.

[UNFCCC] UNFCCC. United Nations Framework Convention on Climate Change. Kyoto Protocol. last access: 2013-10-16.

[128] Vamborg, F. S. E., Brovkin, V., and Claussen, M. (2011). The effect of a dynamic background albedo scheme on Sahel/Sahara precipitation during the mid-Holocene. *Climate of the Past*, 7:117–131.

[129] Vuille, M. and Werner, M. (2005). Stable isotopes in precipitation recording South American summer monsoon and ENSO variability: observations and model results. *Climate Dynamics*, 25(4):401–413.

[130] Wang, K. and Dickinson, R. E. (2012). A review of global terrestrial evapotranspiration: Observation, modeling, climatologie, and climatic variability. *Reviews of Geophysics*, 50:RG2005.

[131] Ward, M. N. (1998). Diagnosis and Short-Lead Time Prediction of Summer Rainfall in Tropical North Africa at Interannual and Multidecadal Timescales. *Journal of Climate*, 11:3167–3191.

[132] Weldeab, S., Lea, D. W., Schneider, R. R., and Andersen, N. (2007). Centennial scale climate instabilities in a wet early Holocene West African monsoon. *Geophysical Research Letters*, 34:L24702.

[133] Werner, M., Langebroek, P., Carlsen, T., Herold, M., and Lohmann, G. (2011). Stable water isotopes in the ECHAM5 general circulation model: Toward high-resolution isotope modeling on a global scale. *Journal of Geophysical Research: Atmospheres*, 116:D15109.

[134] Xu, X., Werner, M., Butzin, M., and Lohmann, G. (2012). Water isotope variations in the global ocean model MPI-OM. *Geosientific Model Development*, 5:809–818.

[135] Yeshanew, A. and Jury, M. R. (2007). North African climate variability. Part 2: Tropical circulation systems. *Theoretical and applied climatology*, 89(1-2):37–49.

[136] Yoshimura, K., Miyazaki, S., Kanae, S., and Oki, T. (2006). Iso-MATSIRO, a land surface model that incorporates stable water isotopes. *Global and Planetary Change*, 51(1-2):90–107.

[137] Zeng, N., Neelin, J. D., Lau, K.-M., and Tucker, C. J. (1999). Enhancement of Interdecadal Climate Variability in the Sahel by Vegetation Interaction. *Science*, 286(5444):1537–1540.